

SHRP-A-656

Development of an Asphalt Core Tomographer

C.E. Synolakis, R.M. Leahy, M.B. Singh,
Z. Zhou, S.M. Song, D.S. Shannon
Department of Civil Engineering
University of Southern California



Strategic Highway Research Program
National Research Council
Washington, DC 1993

SHRP-A-656
Contract A-002B

Program Manager: *Edward T. Harrigan*
Project Manager: *Jack Youtcheff*
Production Editor: *Marsha Barrett*
Program Area Secretary: *Juliet Narsiah*

June 1993

key words:
3-D imaging
asphalt core deformation
asphalt content
core tomography
crack identification
voids network mapping

Strategic Highway Research Program
National Academy of Sciences
2101 Constitution Avenue N.W.
Washington, DC 20418

(202) 334-3774

The publication of this report does not necessarily indicate approval or endorsement of the findings, opinions, conclusions, or recommendations either inferred or specifically expressed herein by the National Academy of Sciences, the United States Government, or the American Association of State Highway and Transportation Officials or its member states.

© 1993 National Academy of Sciences

Acknowledgments

The research described herein was supported by the Strategic Highway Research Program (SHRP). SHRP is a unit of the National Research Council that was authorized by section 128 of the Surface Transportation and Uniform Relocation Assistance Act of 1987.

This report is the result of a truly multidisciplinary effort of civil engineers, electrical engineers, radiologists, chemists, chemical engineers and asphalt paving technologists.

We are happy to acknowledge the numerous contributions of the following colleagues in their work. Our thanks go to: our students, Sam Song and Zhenyu Zhou, for preparing most of the images in this report; Sam Song, for his work on 2-D optical flow in appendix A which was his PhD thesis; our project manager Jack Youtcheff for his technical input, guidance, and resilience, his commitment to excellence was a substantial motivating factor to produce more and better for less. We are thankful to: our resident asphalt paving technologist Joe Vicelja for arranging the support of the LA County Materials Lab and for introducing us to the grit of asphalt testing; the A001 technical coordinator Jim Moulthrop for his technical and administrative support and for reviewing the first two drafts of this report; Ron Cominsky, Ed Harrigan, and Rita Leahy for many technical suggestions; Carl Monismith, Ron Terrel, Lloyd Griffiths, Tom Kennedy, and Janine Nghiem for providing us with cores, data, and administrative and technical support with the management of the project. Special thanks are extended to Dave Shannon and Paul Mercurief for their assistance with the core preparation and with the loading tests.

We are grateful to SHRP for its contract 88-A002B.

Contents

Table of Contents	i
List of Figures	iii
Acknowledgements	1
1. Executive Summary	2
2. Introduction to Computer Tomography	4
3 Development of the ACT imaging protocol.	11
3.1 Determination of optimal scanner parameters	12
3.2 Determination of asphalt CT numbers.....	13
3.3 Determination of system resolution.....	17
3.4 Determination of system detectability.....	19
3.5 Determination of the beam hardening correction	22
3.6 Determination of aggregate CT numbers	27
3.7 Determination of the CT numbers of asphalt mixes with fines	29
4. Mass fraction calculations and morphological studies	36
4.1 Determination of the mass fraction of asphalt/aggregate cores	36
4.2 Large scale 2-D deformation studies	38
4.3 Three dimensional morphological studies	45
4.4 Special Topics	50
4.4.1 Voids network visualization	50
4.4.2 Magnetic resonance imaging in asphalt testing	51

Conclusions	52
Recommendations	53
References	55
References for Appendix A	56

Appendices

A. Computation of 3-D displacement fields from 3-D x-ray CT scans of a deforming asphalt core	58
B. User's manual for the ASPlab software package	82

List of Figures

Figure 2.1 Schematic diagram of a particle beam incident on a three-dimensional object	5
Figure 2.2 Schematic of a third generation CT scanner imaging a patient's head	7
Figure 2.3 Typical CT values for the different components of the human body	8
Figure 2.4 Four slices of CT images of asphalt cores	9
Figure 3.2.1 Photograph of lucite phantom	15
Figure 3.2.2 Plot of attenuation data as function of metal content of different asphalts	16
Figure 3.3.1 Tomogram of the platinum wire used to determine the PSF	18
Figure 3.3.2 PSF derived from the image in figure 3.3.1	18
Figure 3.4.1 Map of the particles in asphalt AAG to determine the detectability of the system	20
Figure 3.5.1 Typical energ spectrum generated by x-ray tube	22
Figure 3.5.2 Reconstructed image from polychromatic projection data. Plot of linear attenuation coefficient as a function of the radius	24
Figure 3.5.3 a Plot of the function $C(r, z, \mathcal{E}) = \int_0^\pi f(r, \phi, \mathcal{E})d\phi$ for three different energy levels and three different elevations.	26
Figure 3.5.3b Plots of the function $C(r, z, \mathcal{E})$ for three different energy levels, but at the same axial elevation	26

Figure 3.5.4a Two cross-sectional images of the asphalt/fine-aggregate core before and after the beam hardening correction	27
Figure 3.5.4b The variation in the CT number along a diameter of the images in Figure 3.5.4a.....	27
Figure 3.6.1 Six tomograms of aggregate particles in a water bath.....	31
Figure 3.7.1 Tomograms of eight different fine-aggregate/asphalt cores.....	33
Figure 3.7.2 Variation of the CT number with the asphalt content in percentage by weight units for three different energy levels	34
Figure 4.2.1 Typical loading curve for the 5B1WOFD core.....	40
Figure 4.2.2a Sequence of tomograms of six different cross-sections of the 5B1WOFD core before loading.....	41
Figure 4.2.2b Sequence of tomograms of six different cross-sections of the 5B1WOFD core after the first loading cycle.	42
Figure 4.2.2c Sequence of tomograms of six different cross-sections of the 5B1WOFD core after the second loading cycle. A large crack is visible.....	43
Figure 4.2.3 Demonstration of image flow calculations. Two registered images of the 5B1WOFD core before and after two stages of loading	45
Figure 4.2.4 The streamflow pattern associated with the velocity field of figure 4.2.3	46
Figure 4.3.1 Three series of eight properly registered CT images of a core at three different stages of loading. The images are taken along planes perpendicular to the core axis. . .	48
Figure 4.3.2 Three properly registered CT images of a core at three different stages of loading. The images are taken along planes perpendicular to the core axis, i.e., along the azimuthal plane.	49

Appendix A
Computations of 3-D displacement fields
from 3-D x-ray CT scans of
a deformed asphalt core.

Figure A.1 Simulated images for experiments 1,2 and 3	76
Figure A.2 Calculated flow field from experiment 1 with the boundary outlines; the dotted circle represents the second time frame.	77

Figure A.3 Calculated flow field from experiment 1 with the boundary outlines; the dotted circle represents the second time frame.	78
Figure A.4 Calculated flow field from experiment 1 with the boundary outlines; the dotted circle represents the second time frame.	79
Figure A.5 Simulated images for experiment 4. Vertically translating ellipsoid at two times.	80
Figure A.6 Results of experiment 4. Results of 3-D vector field as a function of a 3-D space is projected into a plane.	81
Figure A.7 Demonstration of image flow calculations. Two registered images of deforming core before and after two stages of loading.	82

Appendix B

ASP Image Lab User's Manual

Figure B.1 Image of a fine core, as displayed by the CT computer.	86
Figure B.2 Image of the core in figure B.1 after the modify data operation. The image of the CT gantry has been removed.	86
Figure B.3 Image of a fine core before and after the beam hardening calibration.	88
Figure B.4 Variation of the CT number along a diameter of the image in figure B.3 before and after BH calibration.	88
Figure B.5 Image of a mixed fine/coarse aggregate core before and after the beam hardening calibration.	89
Figure B.6 Variation of the CT number along a diameter of the image in figure B.5 before and after BH calibration.	89
Figure B.7 Image of a coarse core before and after the beam hardening calibration. ...	90
Figure B.8 Variation of the CT number along a diameter of the image in figure B.7 before and after BH calibration.	90
Figure B.9 Image of the mixed coarse/fines aggregate core of figure B.5 after self-calibration.	92
Figure B.10 Variation of the CT number along a diameter of the image in figure B.9 after BH self-calibration.	92

Figure B.11 Image of a mixed coarse/fine aggregate core showing the mass fraction of asphalt.....93
Figure B.12a Image of a mixed core and enhanced image.....96
Figure B.12b Sharpened image and edge-Robert image of the core in figure B.12a...97
Figure B.12c Sharpened image and binary image of the core in figure B.12a.98
Figure B.13a Image of a coarse core and enhanced image.....99
Figure B.13b Sharpened image and edge-Robert image of the core in figure B.13a..100
Figure B.13c Sharpened image and binary image of the core in figure B.13a.101

Abstract

This a study of the application of computer tomography (a non invasive laboratory technique for imaging the interior of objects with complex internal geometry) in the study of asphalt pavements. A standardized imaging procedure is developed and presented for imaging asphalt cores using an x-ray CT scanner. This protocol is referred to as asphalt core tomography (ACT) and it includes the optimal beam energy and intensity settings, imaging time, slice-thickness, interslice spacings standard calibration procedures and the CT characteristics of asphalt and aggregates, and it includes various enhancements algorithms to remove imaging artifacts and to perform beam hardening corrections.

The imaging protocol can be used to determine the asphalt mass fractions in mixed and coarse aggregate cores. The protocol is found to generate reasonable estimates of the true mass fractions inside the core and it can be used to complement destructive chemical extraction methods. ACT can also be used to study the three dimensional internal deformations which occur as a core is going through different loading cycles. By extending existing two-dimensional motion detection methods, and by comparing properly registered CT images of a core before and after a loading test, ACT can compute the complete displacement field for the entire core.

The greatest potential application of ACT in materials testing application is in forensic studies and in screening cores for unusual features before further destructive testing.

1. Executive Summary

In January 1989, the Strategic Highway Research Program of the National Research Council awarded the University of Southern California contract A002B to pursue innovative methods in the investigation of asphalt material properties. The original contract had three different subtasks, the development of an asphalt core tomographer, the investigation of a colloidal chemical approach to beam hardening, and the application of acoustic emission techniques in the study of adhesive and cohesive strength of asphalt concretes. This report summarizes the findings of the first subtask, namely the development of an asphalt core tomographer; other reports summarize the other subtasks. The objective of this subtask was to investigate whether x-ray computer tomography could be applied in the study of asphalt concretes and of asphalt/aggregate mixes. The following specific objectives were established at the outset:

1. To develop a standardized procedure for imaging asphalt cores using an x-ray CT scanner. This protocol would include optimization of the beam energy and intensity settings, imaging time, slice thickness, interslice spacings and standard calibration procedures.
2. To develop software for transferring data and image files from the CT computer to the image processing workstation for performing automated image processing and interpretation.
3. To conduct preliminary ACT experiments to study the interior of asphalt cores.
4. To determine various mass and area fractions and their distributions.

5. To evaluate large scale deformations before and after loading.

The objectives of this contract have been achieved. We have demonstrated the applicability of computer tomography in asphalt studies and we have developed and a standardized imaging protocol for testing asphalt cores. We have also developed optical-flow type solution algorithms which allow for detailed quantitative studies of core deformations.

We believe that ACT can be used most effectively in the following areas of asphalt paving technology:

- 1) To complement chemical stripping tests and to provide certain mass-fraction data for the core composition.
- 2) To routinely screen cores which will be used in other standardized tests. The screening would detect any unexpected anomalies which might unduly influence the results.
- 3) To provide data on the the detailed composition of asphalt cores for forensic studies, both to determine whether certain contract specifications have been met, or to investigate the cause of failure of asphalt pavements.
- 4) To detect and to measure the propagation and geometric characteristics of internal cracks down to $1mm(0.025in)$ size, even for cracks parallel to the core axis.

Our results suggest that ACT –whose cost is estimated to be no more than \$400 per core scan– is a very cost– effective testing method for morphological studies. We recommend that the State Highway Agencies adopt this test to complement standard materials testing protocols.

2. Introduction to Computer Tomography.†

Computer tomography is a non-invasive laboratory technique for imaging the interior of objects with complex internal structure. The method attempts to relate changes in the intensity of penetration of a particle or photon beam through an object to the density of the object. It uses a particle or photon beam source and a detector array to obtain data, a dedicated processor for data reconstruction and another dedicated processor for the display. The procedure attempts to produce a series of cross-sectional images of an object from a number of projections. It can be described as follows. A thin plane layer of a three-dimensional object –referred to as a *slice*– is isolated by the synchronized movement of the beam source and the detector array. A schematic diagram of this arrangement is shown in figure 2.1.

During the synchronized motion of the beam detector assembly, beam projection data are obtained for the particular image plane from many different angles. Then the changes in the beam intensity from the source to the detector are related to the densities of the nonuniformities and inhomogeneities in the interior of the slice, and eventually a two-

† The discussion in this chapter is a simplified introduction to computer tomography. We follow the style of Davidson's chapter in the book *Scientific basis for medical image processing (1982)* (edited by P.N.T. Wells) and Kak's (1979) article (*Computerized tomography with X-ray, emission x-ray and ultrasound sources*; both are excellent basic reviews of the reconstruction algorithms and of other imaging modalities such as emission CT and ultrasound CT).

dimensional map of the interior density of the slice is produced.

The reconstruction of the image of the interior structure of the slice relies on a basic principle of topography. This principle requires that given a set of single beam projections through a two-dimensional slice then it is possible to derive the exact distribution of the attenuation coefficient of the beam for the entire volume. This simple technique was first suggested in 1940 by T. Watson but -because the image reconstruction is very computationally intensive- it was not applied until twenty years later when powerful enough computers started becoming available. In 1972, Hounsfield designed the first "modern" computer tomographer. His discovery profoundly changed biomedical imaging and medicine. For this, Hounsfield was awarded the Nobel prize for medicine in 1976.

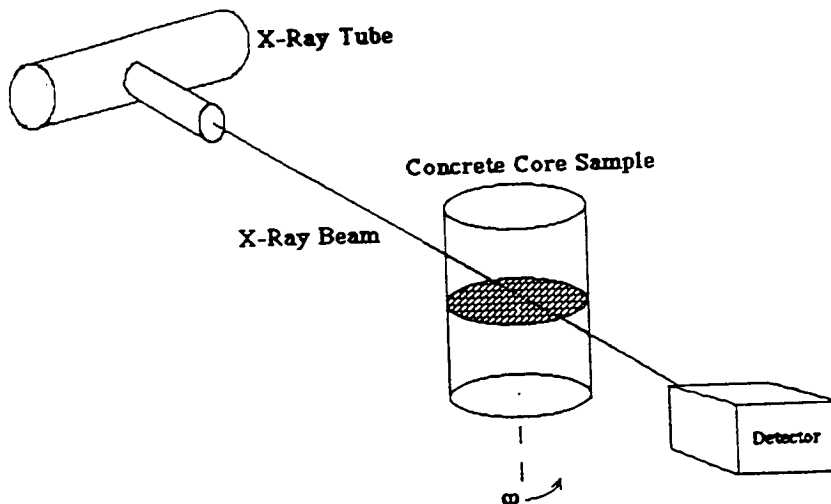


Figure 2.1 A schematic diagram of an x-ray beam system incident on a three-dimensional core.

To appreciate the operation and nomenclature of computer tomography, consider a *monochromatic* photon beam[‡] of intensity I_0 incident upon a homogeneous object of width

[‡] The epithet *monochromatic* refers to a monoenergetic photon beam; in reality an x-ray source produces a beam with a spectrum of energy. In general, the attenuation coefficient

d and density ρ . The intensity of the beam after it penetrates the object is $I_{\text{transmitted}}$, it is a function of both d and ρ and it is related to I_0 by the following relationship :

$$I_{\text{transmitted}} = e^{-k(\rho, \mathcal{E})d} I_0. \quad (1)$$

$k(\rho, \mathcal{E})$ is referred to as *the attenuation coefficient* of the object and it is directly related to its density ρ , and is a function of the incident energy \mathcal{E} . When the incident beam is monochromatic, the dependence of k on the incident energy is usually omitted for brevity, and one writes $k(\rho)$.

When the object is inhomogeneous, then the intensity after penetration depends on the distribution of density $\rho(x, y, z)$ which the beam encountered along its path through the object. In this case the transmitted intensity is given by

$$I_{\text{transmitted}} = e^{-\int_L k(\rho(x, y, z)) dl} I_0. \quad (2)$$

L is the total path length and dl is the differential element along the path. The integral $\int_L k(\rho(x, y, z)) dl$ is referred to as the *ray integral*. In a conventional CT, the detector signal is averaged over a short period of time and then digitized. Since the reference I_0 is known, by measuring sets of $I_{\text{transmitted}}$, sets of values of the $\log(I_{\text{transmitted}}/I_0)$ provide sets of the values of the ray integral $\int_L k(\rho(x, y, z)) dl$ along different paths L . A set of such values of ray integrals is called a *projection*. Given a large number of projections, one obtains a sufficient number of values of $\int_L k(\rho(x, y, z)) dl$ so that it becomes possible to derive an approximate map of $k(\rho(x, y, z))$ throughout the two-dimensional slice. Image reconstruction algorithms are then used to assign different grey-level intensities to ranges of values of $k(\rho(x, y, z))$ which lead to a two-dimensional grey-scale image produced on a computer monitor.

Figure 2.2 shows a schematic of a third generation x-ray scanner imaging a patient's head. The detector-array provides one projection, i.e., a set of values of $\log(I_{\text{transmitted}}/I_0)$ for every angle of the X-ray tube assembly.

also depends on the photon energy, and the polyenergetic beams produce imaging artifacts. This problem is described in section 7 .

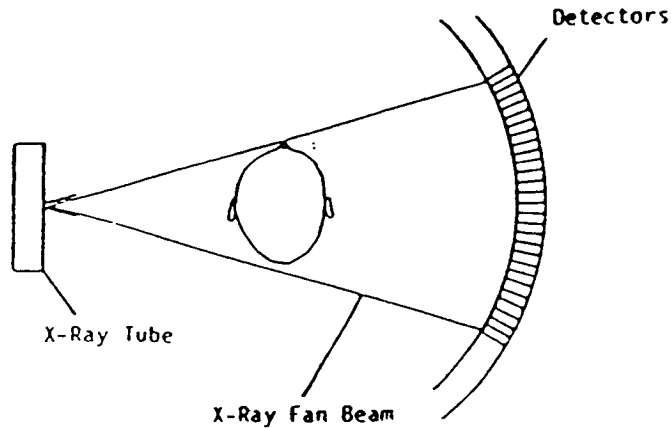


Figure 2.2 A schematic of a third generation CT scanner imaging a human head. The figure shows a *fan* beam projection system with equiangular rays. Typically, the fan has an angle of 30 to 45 degrees and the detector array has about 500 to 700 xenon gas ionization detectors.

In practice absolute values of the attenuation coefficient are never calculated; instead the processor assigns integer values at each pixel of the image. These values are known as *CT numbers*. The CT number is related to the attenuation coefficient by the equation

$$CT = K \left(\frac{k_{\text{asphalt}}}{k_{\text{water}}} - 1 \right). \quad (3)$$

When the coefficient $K = 1000$, then the CT numbers are also referred to as the Hounsfield numbers. In this report we will use the terms Hounsfield numbers and CT numbers interchangeably.

The CT number is essentially the relative difference of the attenuation coefficient of the material from the attenuation coefficient of water; the larger the specific gravity of the material, the higher the CT number is. This implies that if a material has an attenuation coefficient which is very close to that of water, then the imaging system will not be able to resolve any water-filled voids inside that material. Computer tomography works best when the inhomogeneities in the material have large differences in their attenuation coefficients. Typical CT values for the human body are shown below in figure 2.3. Notice how different the CT numbers are for the various tissue types. One of the objectives of this study was to

determine if sufficient differences in the CT numbers exist among the various components of an asphalt/aggregate core to make asphalt tomography possible.

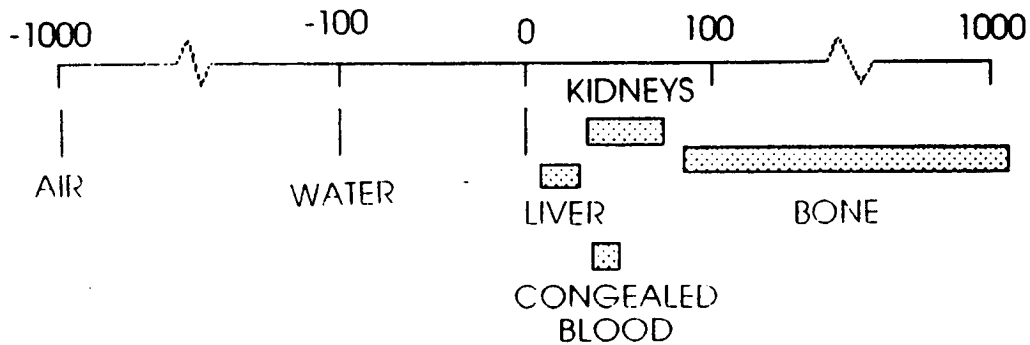


Figure 2.3 Typical CT values for the different components of the human body. After Davison (1982).

Computer tomography systems use specialized dedicated processors together with sophisticated image reconstruction algorithms to produce the final image.

The single most common beam systems in use for computer tomography are x-ray systems, which are now ubiquitous in medicine and in aerospace engineering. In medical applications the peak beam energies vary from 100keV to 130keV. One example of an image from a medical scanner is shown in figure 2.4. In prototype industrial applications the beam energies are about 1500keV, because higher energies are required to penetrate through denser materials. (One such system was installed in 1989 at the Physics Division of the Boeing Co.) Another type of tomography is acoustic tomography which uses ultrasound waves instead of x-rays; its resolution and sensitivity is much poorer because acoustic beams in a non-homogenous material do not necessarily travel in straight lines as they scatter and diffract at the interfaces between different materials. Other related computer tomography modalities include magnetic resonance imaging (MRI) and positron emission tomography. However these are based on entirely different principles of operation, whose discussion is beyond the scope of this introduction. In this study we only used x-ray tomographic imaging; however we did test the applicability of MRI in core tomography but our preliminary MRI results had very poor resolution. Acoustic tomography is clearly ineffective for high resolution core studies with the current generation of ultra-sound scanners.

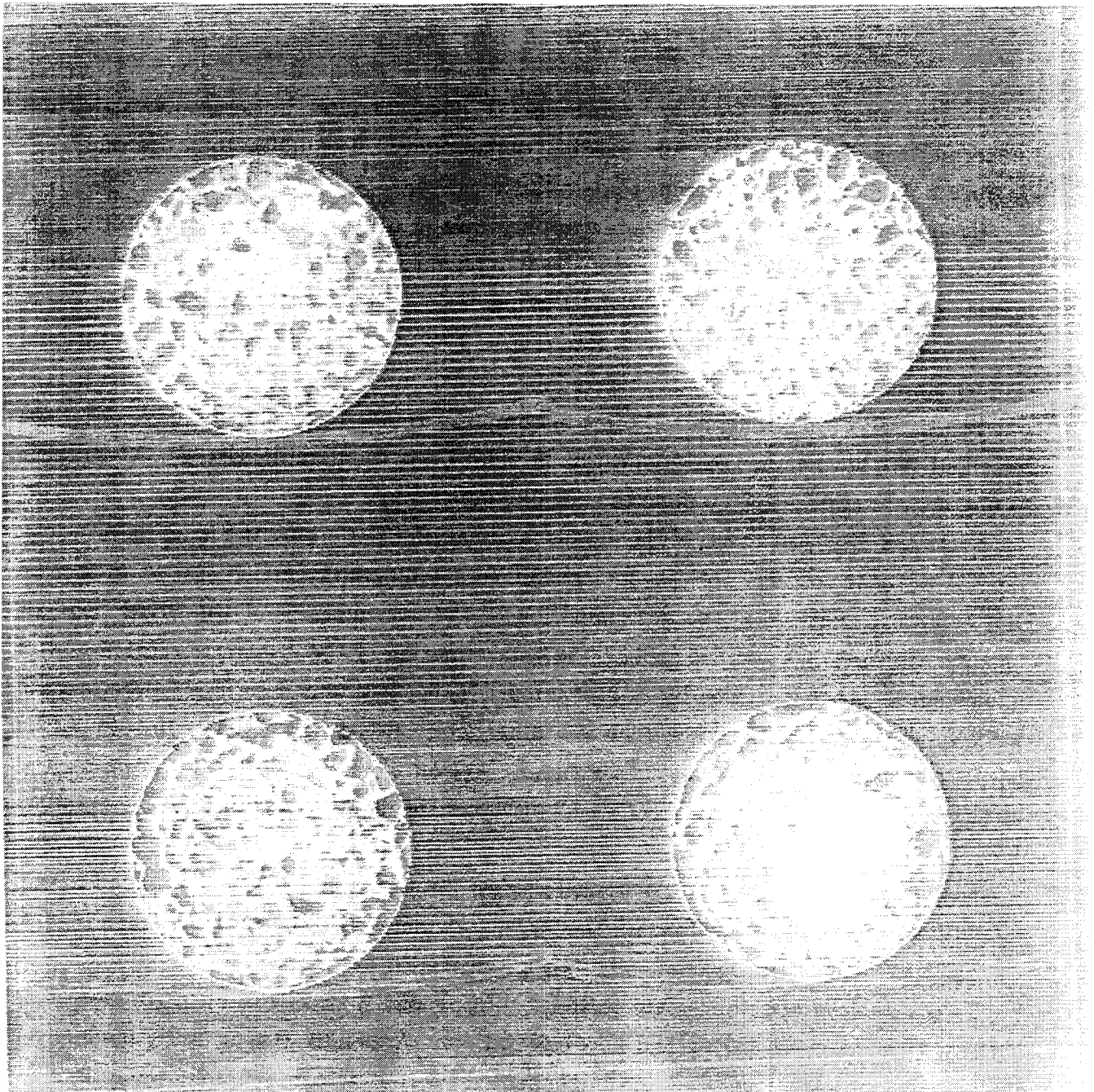


Figure 2.4 Four slices CT images of asphalt cores

Testing an asphalt core with a medical CT does not alter its molecular structure; furthermore it does not leave any residual radioactivity. The ubiquitous use of CT in diagnostic medicine is a testament to its relative safety.

Even though there have been a few applications of computer tomography in imaging soil and earth cores, CT had never before been applied to the study of asphalt or of asphalt aggregate cores. In our study we used a Phillips TX60 which is a third generation x-ray CT scanner and is located at Norris Hospital at USC. It utilizes a fan beam rotational scanner similar to that sketched in figure 2.2.

In this report the imaging protocol of computer tomography and its application are described. We have named our application Asphalt Core Tomography (ACT). We will also discuss certain applications unique to asphalt tomography.

Section 3 discusses many of the details necessary for performing the imaging protocol. The CT scanner settings optimal for asphalt core tomography are described in section 3.1. Section 3.2 discusses the determination of the CT numbers of the SHRP asphalt cements. Sections 3.3 and 3.4 explain the determination of the system resolution and of the system detectability. The beam hardening(BH) correction is described in section 3.5; this is a procedure for removing some of the image reconstruction artifacts introduced by the polychromatic nature of real x-ray tubes. Section 3.6 discusses the determination of the aggregate CT numbers, and section 3.7 discusses the determination of the CT numbers of asphalt mixes with fines.

Section 4 describes our morphological studies. Section 4.1 discusses the mass-fraction calculations and section 4.2 discusses the large-scale deformation studies.

The conclusions and recommendations are discussed in section 5.

Two extensive appendices are included. Appendix A describes in great detail the mathematical basis for the optical flow calculations. Appendix B is a user's manual for ASPlab, the software developed and implemented for routine core scanning analysis.

3. Development of the ACT Imaging Protocol.

An imaging protocol consists of a set of procedures and CT scanner settings that are used when imaging specific objects. An imaging protocol also includes data on the CT characteristics of the tissues or materials under study. In medical imaging, there are specific imaging protocols for the various regions of the human body; for example, slightly different operating parameters are used when imaging brain tissue than when imaging neck tissue.

In this section we will describe all the operating parameters and the determination of CT data that were necessary in developing the Asphalt Core Tomography protocol.

The CT scanner settings optimal for asphalt core tomography are described in section 3.1. Section 3.2 discusses the determination of the CT numbers of the SHRP asphalt cements. Sections 3.3 and 3.4 explain the determination of the system resolution and the system detectability. The beam hardening correction (BH) is described in section 3.5; this is a procedure for removing some of the image reconstruction artifacts introduced by the polychromatic nature of real x-ray tubes. Section 3.6 discusses the determination of the aggregate CT numbers, and section 3.7 discusses the determination of the CT numbers of asphalt mixes with fines.

3.1 Determination of the optimal scanner parameters.

CT was originally developed for human studies; operating parameters have to be modified to yield optimal results for concrete/aggregate cores.

We established a standard imaging protocol for asphalt core tomography, and we determined the optimal system parameters by imaging two cylindrical asphalt/aggregate cores of 15.24cm(6.0in)diameter and of 10.16cm(4.0in) height.

In particular we determined the following optimal parameters for the x-ray tube settings :

X-ray peak energy = 130kV

Beam intensity = 250mA

Scan time = 3msec

Slice thickness = 3mm

These parameters produced excellent grey-scale images with good contrast. Other system parameters such as the number of repetitions, the number of projections, and the interslice spacing appear to be highly dependent on the specific application and the resolution desired for 3-D studies and they do not depend on the single slice data. However we found that a maximum 3mm(0.12in) interslice spacing is necessary for achieving uniform contrast across the entire image, as well as the desired level of detectability.

Next we developed a specialized algorithm for transferring the CT image file data from the CT computer to SUN and Macintosh workstations. For proprietary reasons, the CT image data are scrambled by the CT computer, and they are not stored in a standard image processing format. Our unscrambling algorithm is specific to images generated by Phillips-made CT scanners; Several software packages have been announced by various vendors for transferring data from CT computers in standard image format (PICT or TIFF files). This is discussed further in the appendix on ASPlab.

3.2 Determination of Asphalt CT Numbers.

To obtain quantitative information from an asphalt/aggregate core image, it is necessary to have accurate CT numbers for the different material components composing the core. This is necessary to properly identify the different components (i.e., asphalt, voids, aggregates, asphalt-aggregate mixes) during image reconstruction. This is not a straightforward as it appears; uncorrected CT images have beam hardening artifacts which are introduced due to the polychromatic nature of the x-ray beams in commercial CT systems. If uncorrected, these artifacts could be interpreted as regions of higher asphalt/fine-aggregate mix density. Medical CT scanners have standard algorithms for compensating for these effects, but unfortunately they have been developed specifically for human studies.

To determine the CT values of asphalt we followed a standard calibration procedure by constructing a water phantom. At first, a plexiglass phantom[†] was constructed. The phantom was a solid lucite cylinder 15.24cm(6.0in) diameter and of 10.16cm(4.0in) height. The phantom had nine 2.54cm(1.0in) cylindrical bore holes and it was used to hold test-tubes of different asphalts during CT scans.

This plexiglass phantom performed satisfactorily, except that the CT values obtained for the different SHRP asphalts showed a relatively large standard deviation around their mean values. Even though it was evident that beam hardening effects accounted for these deviations, it was important to ensure that the values obtained were reliable asphalt CT values. Therefore, we constructed another phantom which surrounded the test-tubes with water; water is known to have relatively small x-ray attenuation and therefore the new phantom was designed to reduce the beam hardening effect.

The new phantom was manufactured by using 15.24cm(6.0in) diameter, 0.635cm(0.25in) thickness lucite pipe, and it was 10.16cm(4.0in) high with two circular plates as lids. The top lid had nine 2.54cm(1.0in) diameter holes; these holes were the receptacles for the test-tubes and were lined with rubber O-rings for sealing. In the same lid we drilled a 0.635cm(0.25in) hole for bleeding out the residual air remaining after the phantom had

[†] A *phantom* is a lucite cylindrical box with known CT characteristics and is routinely used to calibrate the CT scanner.

been filled with water.

In normal operation, asphalt cements were poured in the pyrex test-tubes and the test-tubes were placed in the holes; then the phantom was filled with water. This geometrical configuration was identical to that of the plexiglass phantom, except that now the inner space between adjacent test-tubes was filled with water instead of solid lucite. Figure 3.2.1 shows a photograph of the lucite phantom with several asphalt test-tubes.

Using this phantom we obtained the following values for the attenuation coefficients of six SHRP asphalts.

Table 3.2.1

Asphalt	Hounsfield#
AAM-1	-62.00
AAG-1	-25.80
AAB-1	-14.40
AAA-1	-4.40
AAD-1	22.20
AAK-1	34.30

These numbers are averages of eighteen different trials for each asphalt. These trials were performed using two different fillings from each of the SHRP asphalts, three different geometric arrangements for each samples within the lucite rack, and using three different elevations with respect to the top of the rack. The CT number in each trial was determined using the Region of Interest (ROI) operation of the CT computer. The ROI we used was approximately $100mm^2(0.16in^2)$, and the CT number variations between trials were less than 5%, except for the AAG-1 asphalt where it was less than 10%. ‡

These attenuation values were then compared with the chemical composition of the SHRP asphalts. The most interesting results were derived when the metal content of the asphalts was plotted with the Hounsfield number; as expected, higher metallic content correlated well with higher Hounsfield numbers. These results are presented in figure 3.2.2.

‡ The ROI operation is performed by selecting of any arbitrary closed contour by a roller-point type mouse. The computer displays the enclosed area in mm^2 and then the average CT number. The same operation exists in the ASPLab software described in Appendix B.

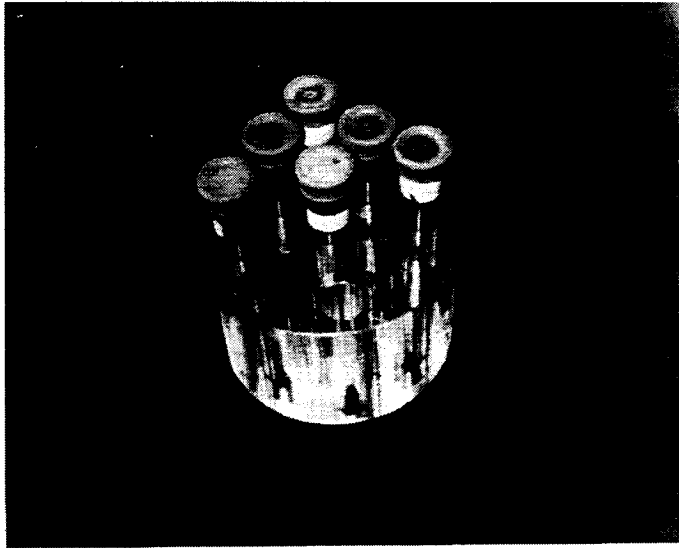


Figure 3.2.1 A photograph of the lucite phantom.

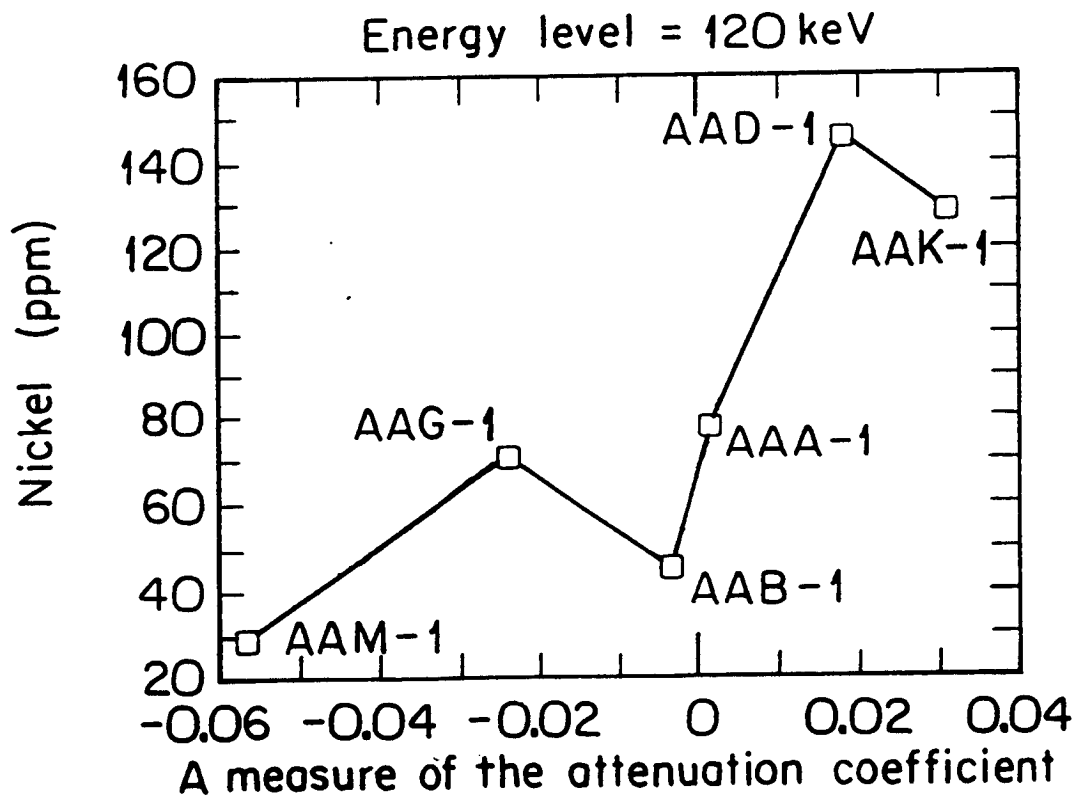
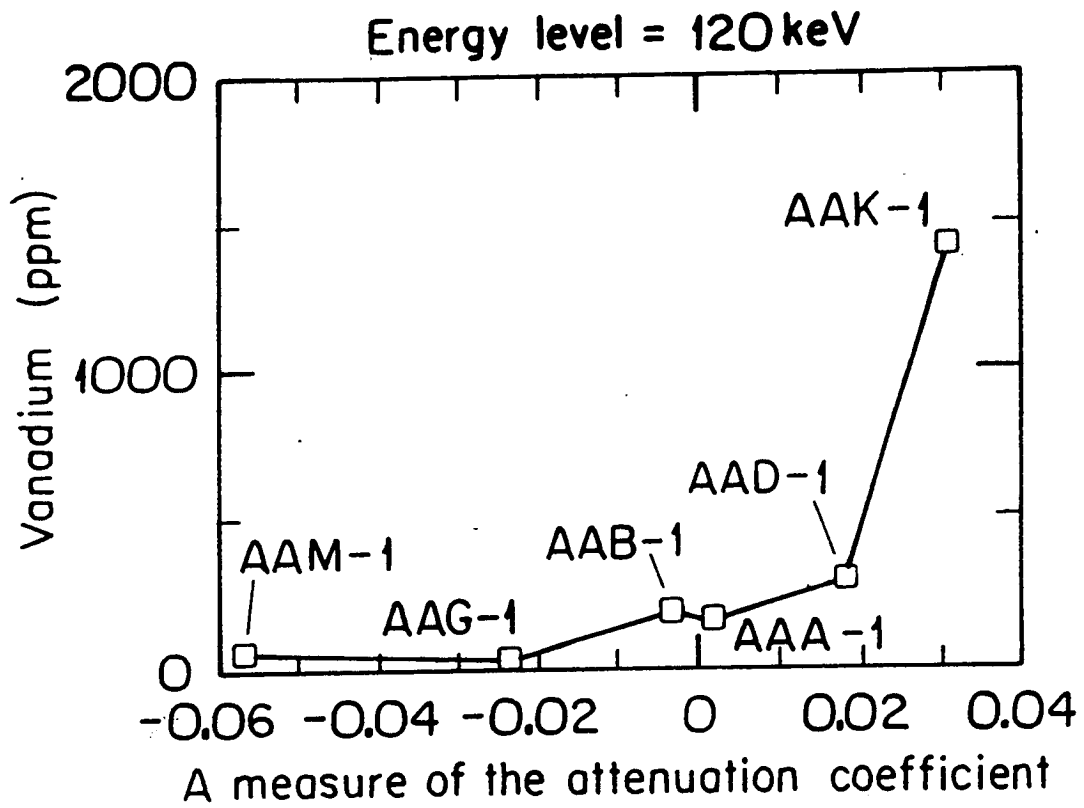


Figure 3.2.2 Attenuation data as a function of the metal content of different asphalts.

3.3 Determination of the System Resolution

It is customary in CT investigations to determine the system resolution by calculating a nominal system performance parameter referred to in signal processing as *the point spread function* (PSF). This parameter is a measure of the smallest geometric features which can be identified by the CT scanner.

To appreciate this parameter, consider the CT monitor display which normally consists of a square array of 512×512 pixels. Since the imaging test area is approximately $129\text{cm}^2(20\text{in}^2)$, then approximately every area of $1\text{mm}^2(0.016\text{in}^2)$ of the test object is mapped in one pixel. One could conclude that the resolution is about approximately $1\text{mm}(0.04\text{in})$.

To obtain a reliable estimate of the system resolution, a $0.4\text{mm}(0.015\text{in})$ platinum wire was imaged in an air phantom. Figure 3.3.1 shows an image of a section of the wire, the test-tube and the phantom. If the system had had perfect resolution, and since there are 2pixels/mm, then the wire should occupy one pixel in the display. Figure 3.3.2 shows the actual results. The figure shows the distribution of CT numbers normalized between 0 and 320 as a function of the distance perpendicular to the wire axis, in pixel numbers.

This plot depicts the PSF. The centerline of the wire is at approximately 12.5pixels. Under ideal conditions, one would expect to see a single line at that location, similar to a delta function. Instead, it is clear that the image "spills" over into adjacent pixels. The nominal CT resolution is determined by measuring the width in pixels of the distribution at an elevation exactly half the maximum CT number. In this case the maximum is 320, and the half-width at 160 is 4.63 pixels; this implies a nominal system resolution of $2.3\text{mm}(0.09\text{in})$. Note that the system detectability may be higher than the nominal system resolution; images of small dense particle may "bleed" into adjacent pixels making them visible. This phenomenon is further discussed in the next section.

It is important to note that the PSF is dependent on the Hounsfield number. Platinum has density much higher and therefore lower attenuation than the density of aggregate or asphalt. The resolution obtained using the platinum wire is clearly an upper limit of the resolution of the system.

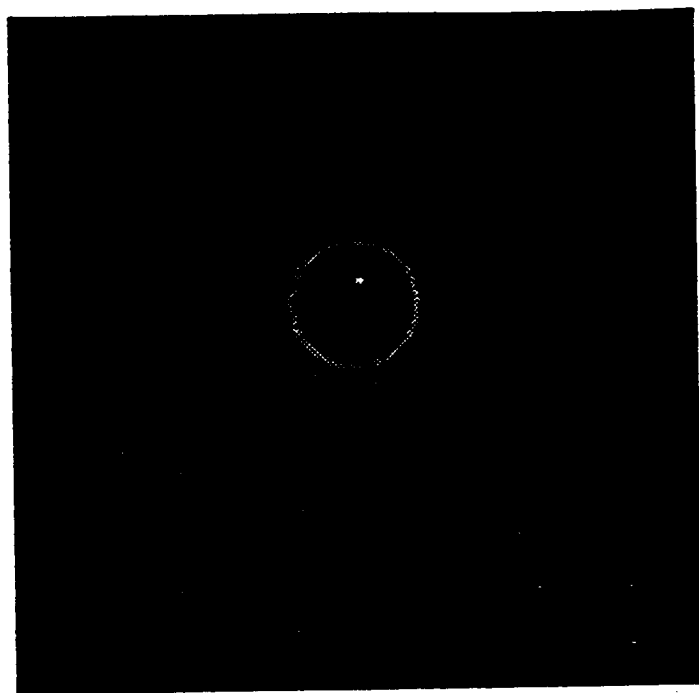


Figure 3.3.1 The image of a platinum wire.

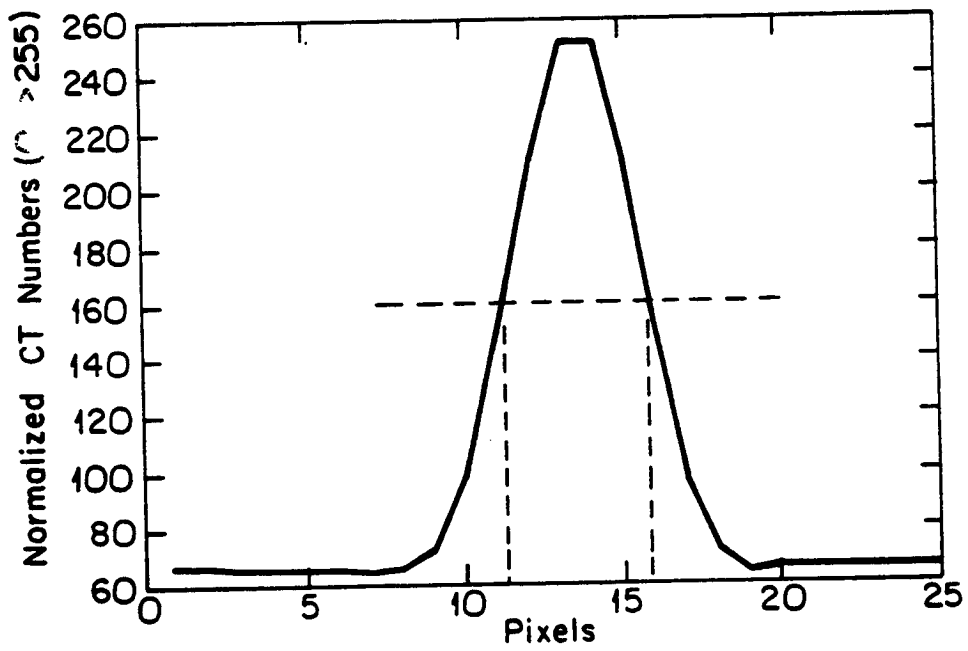


Figure 3.2.2 The point spread function (PSF) derived from the image in figure 3.3.1.

3.4. System Detectability

As discussed in the description of the previous test, the system detectability may be much larger than the system resolution. To determine the detectability of the imaging protocol, we conducted a special test with two objectives. One, to determine of the smallest particle size that is detectable with the ACT, and two, to determine of the smallest identifiable distance between two adjacent particles.

A. Determination of smallest detectable particle size.

Several $2.54\text{cm}(1.0\text{in})$ test-tubes were filled with AAG asphalt up to a specific elevation, approximately half-way up to the top. We then placed a $3\text{mm}(0.12\text{in})$ metallic marker particle on the initially free asphalt surface in each tube. We refer to this surface as the test surface; the marker particle allowed us to locate the image of the test surface quickly with the CT computer when scanning the entire tube. We then located glass beads and sand grains of different sizes on the test surface, and we drew an approximate map of particle sizes and sand grains sizes for the test surface in each tube. An example of this map is shown in figure 3.4.1. Then the tubes were filled with asphalt to the top, so that the test surface could now only be identified through CT images.

The test-tubes were then imaged both in the plexiglass and in the water phantoms. The CT scanner's gantry was moved incrementally until the surface with the marker beads was located in the CT monitor; subsequent slice images were obtained every $1\text{mm}(0.04\text{in})$.

By visual inspection of the CT display monitor, it was possible to detect glass beads and sand grains down to sizes of $0.46\text{mm}(0.018\text{in})$ on our test surface. Particles smaller than the $0.37\text{mm}(0.014\text{in})$ particles smaller were not detected.

We did not find any significant differences in the lower limits of detectability between the glass and the sand particles. Since metallic materials have low attenuation, we expect that the protocol should detect metal grains down to the $0.1\text{mm}(0.004\text{in})$ size ; however, the detection of metallic particles of this size was not attempted.

The detectability was also checked using the cross-hair cursor and the joystick available on the CT console for obtaining specific data from the display. We displayed the test surface and we positioned the cross-hair at one side of the perimeter of one of the

WATER BATH PHANTOM (WBP)

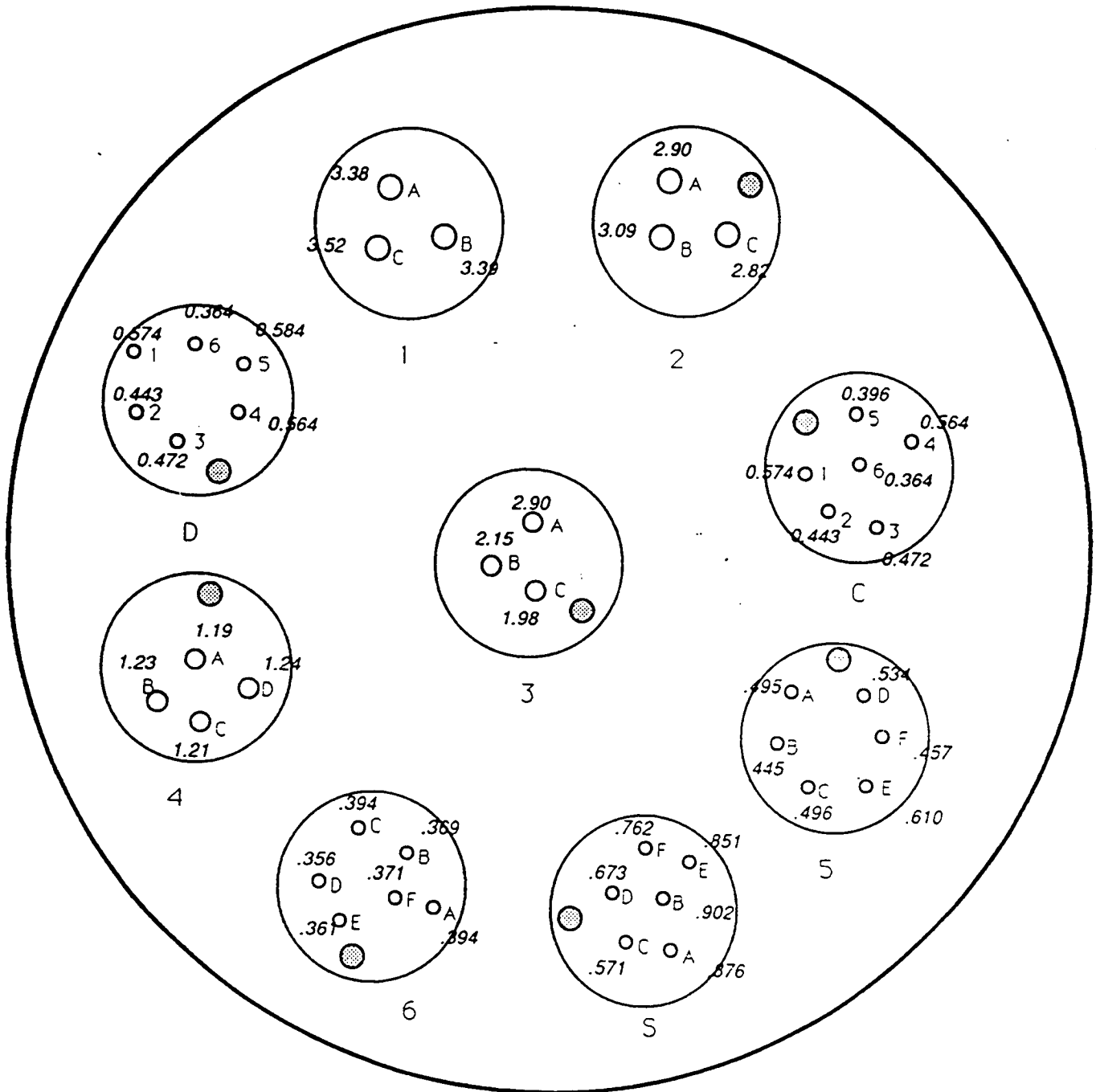


Figure 3.4.1 Map of the particles which were placed inside an AAG asphalt filled test-tube to determine the detectability of the system.

smallest visible beads and noted the co-ordinates from the display. We then moved the cursor to the diametrically opposite side of the bead perimeter, and we noted the co-ordinates again. We thus calculated the size of a particle known to be $0.46\text{mm}(0.018\text{in})$ size to $0.60\text{mm}(0.023\text{in})$ diameter. Since the cursor is at least $0.4\text{mm}(0.016\text{in})$ thick, these observations suggest that the system detectability is $0.5\text{mm}(0.02\text{in})$.

B. The determination of the smallest detectable separation distance.

Another measure of the detectability of the system is the smallest separation distance that can be identified. Images of small particles bleed to adjacent pixels and small particles close together may appear as a single larger particle.

It was not possible to locate submillimeter size particles at fixed distances on the test surface. Therefore, we designed another test by carefully filling a test-tube with asphalt AAG after placing two $1.8\text{mm}(0.070\text{in})$ bore glass capillary tubes. The two tubes were coplanar, but not parallel and they converged to a common vertex. The sample was then scanned and images were obtained, until it was no longer possible to identify the two separate tubes (i.e., until the tubes appeared fused together).

Based on our results, we conclude that the smallest separation distance detectable with the Phillips scanner is of the order of one-tube diameter (i.e., $1.8\text{mm}(0.070\text{in})$).

Note that the detectability of the system (in terms of particle size) is much smaller than the limiting separation distance, since the images of small particles smear on adjacent pixels. A single small particle surrounded by asphalt is easily identifiable; however the images of two small particles very close together appear as the image of a single large particle. This limitation has practically no effect in the mass-fraction calculations for the entire core because the combined image has approximately the same image area as that of the sum of the areas of the two particles.

This one-particle size limit on the detectability of small particles implies that it may not be possible to accurately obtain the particle distribution function for particle sizes smaller than $1.00\text{mm}(0.040\text{in})$. Particles larger than this size have distinct shapes in the CT images even when adjacent to each other.

3.5 Determination of the Beam Hardening Correction.

Beam hardening arises from the *polychromatic* nature of x-ray beams. A characteristic polychromatic x-ray spectrum is shown in figure 3.5.1. The figure shows the number of counts incident on an x-ray detector as a function of the energy of an x-ray tube.†

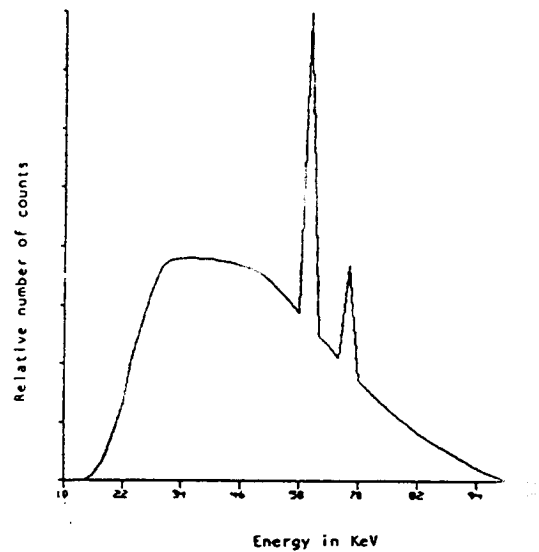


Figure 3.5.1 An example of an experimentally measured x-ray tube spectrum. From Epps and Weiss (1976).

To appreciate how this x-ray spectrum affects the results, consider a *monochromatic* beam with N_{in} photons entering through an object and suppose that $N_{transmitted}$ photons penetrate through this object. According to equation (2), the entering and the transmitted numbers of photons are related by the equation

$$N_{transmitted} = e^{-\int_L k[\rho(x,y,z)]dl} N_{in}. \quad (4)$$

† The ionization detectors employed in the Phillips CT system used in this study respond to energy deposition per unit mass and do not actually count individual photons; however the effect is qualitatively the same as in systems responding to energy deposition (Kak, 1979).

If the beam is polychromatic, then this equations should be replaced by the following

$$N_{\text{transmitted}} = \int S_{\text{in}}(\mathcal{E}) e^{-\int_L \kappa[\rho(x,y,z),\mathcal{E}] dl} d\mathcal{E}. \quad (5)$$

$S_{\text{in}}(\mathcal{E})$ is the incident photon number density in the range between \mathcal{E} and $\mathcal{E} + d\mathcal{E}$, i.e., it is a probability density function. Notice (Kak, 1979), that in equation (5) the attenuation coefficient $\kappa[\rho(x,y,z),\mathcal{E}]$ is also a function of the incident energy \mathcal{E} . In the energy range used in CT, the attenuation coefficient generally decreases with the incident energy. Therefore in a polychromatic beam, the lower energy photons are preferentially absorbed or scattered, and the peak of the exit spectrum maybe higher than the peak of the incident spectrum. This is the *beam hardening* effect we referred to earlier.

As a polychromatic x-ray beam with a continuous distribution of energy levels penetrates a plane of a uniform object, the variation of the attenuation coefficient with the beam energy level produces a variation of CT numbers through the plane. Lower lower-than-actual CT values near the center of the object are then obtained and consequently the image of the slice appears darker near the center than near the edges. This effect is shown in figure 3.5.2. Without correction, this artifact may lead to a serious misinterpretation of the image. For example, darker areas at the center may be interpreted as containing more asphalt than surrounding areas.

To remove this artifact, a beam hardening correction function was applied to transform the CT image. This was done through the calculation of a non-linear transformation function which was then applied to filter the reconstructed image. This transformation function was determined by measuring a standard correction image, and it is often referred to as the beam-hardening kernel.

The correction image was obtained by imaging a specially constructed core. We prepared a $7.62\text{cm}(3.0\text{in})$ diameter and $10.16\text{cm}(4.0\text{in})$ high core with AAG asphalt mixed with finely crushed granite $d_s < 0.5\text{mm}(0.02\text{in})$ to a very uniform consistency. Then we imaged the core at three different energy levels and at three different elevations. Since the core is uniform by construction, under ideal conditions the image of the core should have had uniform gray intensity; yet the center area of the image was slightly darker than the edge area. This effect was obvious in all our uncorrected images of asphalt/aggregate cores. It can be seen in the images in figure 3.5.5a.

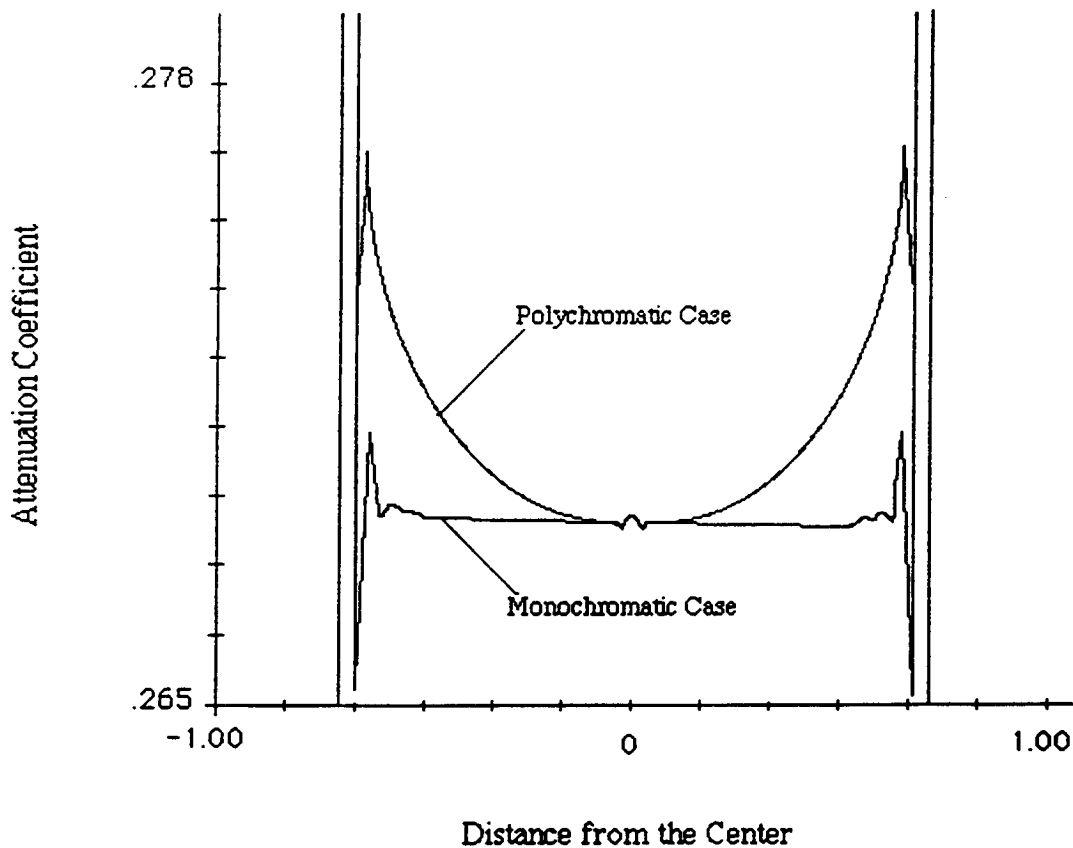
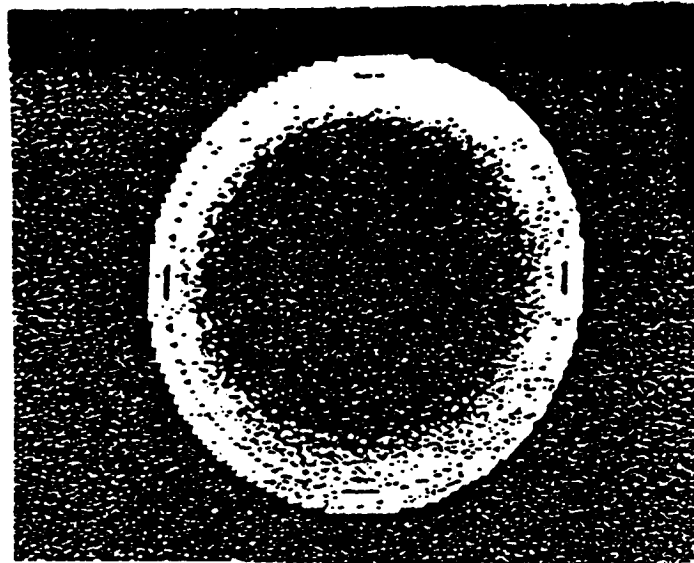


Figure 3.5.2 (a) Reconstructed image from projection data of a surface of a water phantom using a polychromatic source. The whitening seen near the edges of phantom is the beam hardening effect. (b) A sketch of the variation of the linear attenuation coefficient through a diametral line of the water phantom, both with polychromatic and with monochromatic x-ray beams. After Kak(1979).

The variation of the attenuation coefficient (in CT number units) as a function of the relative radial distance from the center normalized with the core radius is shown in figures 3.5.3a and 3.5.3d. The ordinate is the CT number $CT(r, z, \mathcal{E})$ averaged over all azimuthal angles ϕ . In our cylindrical co-ordinate system r is the radial location measured from the center, z is the elevation, and ϕ is the azimuthal angle. The abscissa is normalized so that the number 100 indicates the core edge and the number 0 the sample center. Figure 3.5.3a shows the variation of the CT number at the three different elevations z for three different beam intensities $100kEV$, $120kEV$ and $130kEV$. Each group of three curves represents a different energy level, while each curve in the group represents a different elevation. Without the beam hardening effect, these curves would collapse into one straight line.

Clearly there is little difference in the distribution of CT numbers at different elevations; however there is some difference in the distribution among images derived using beams with different intensities. This is also seen in figure 3.5.3b; here the same image plane was scanned three different times without removing the core from the CT gantry. This is quite a helpful result because it allows the use a single beam hardening correction function for all slice data (i.e. for the entire core), for any given beam intensity.

We determined the two-dimensional nonlinear transformation function $f(\rho; \phi)$ for core analysis using standard image processing methods. The objective was to find a kernel which, when applied on every pixel x, y of a fine-aggregate core image, it would produce uniform gray intensity over the entire image area. Given figure 3.5.3, this kernel does not depend on the the elevation z inside the core, but only on the energy level.

In order to determine the effectiveness of the kernel that we have developed, a coarse-aggregate core was constructed with the same overall density as the fine-aggregate core which was used for the kernel determination. Then we imaged the coarse core at the same energy level as the fine-aggregate core. The results of these scans are shown in figure 3.5.4. Figure 3.5.4a shows the image of a section of the fine aggregate core before performing the beam hardening correction. Figure 3.5.4a shows images of the same slice before and after performing the beam hardening correction.

We have incorporated this operation in our asphalt core image processing software package (ASPlab) described in appendix B. In ASPlab there is a specific menu driven function to perform this correction. The software uses the standard calibration image with AAG asphalt shown in figure 3.5.4a. There is very little difference in the beam hardening

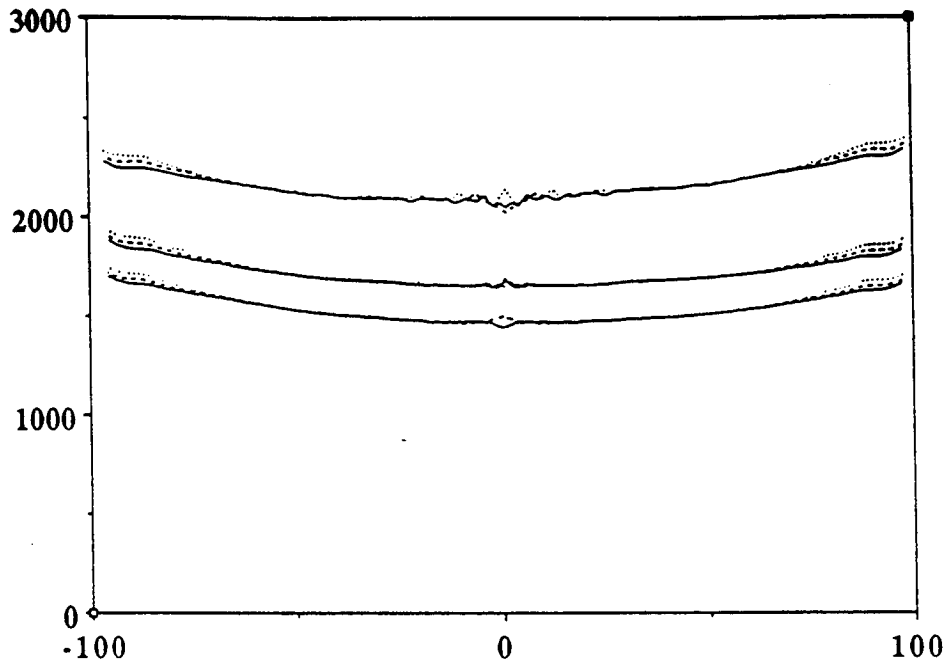


Figure 3.5.3a Plot of the function $CT(r, z, \mathcal{E}) = \int_0^\pi f(r, \phi, \mathcal{E})d\phi$ for three different axial elevations and for three different energy levels.

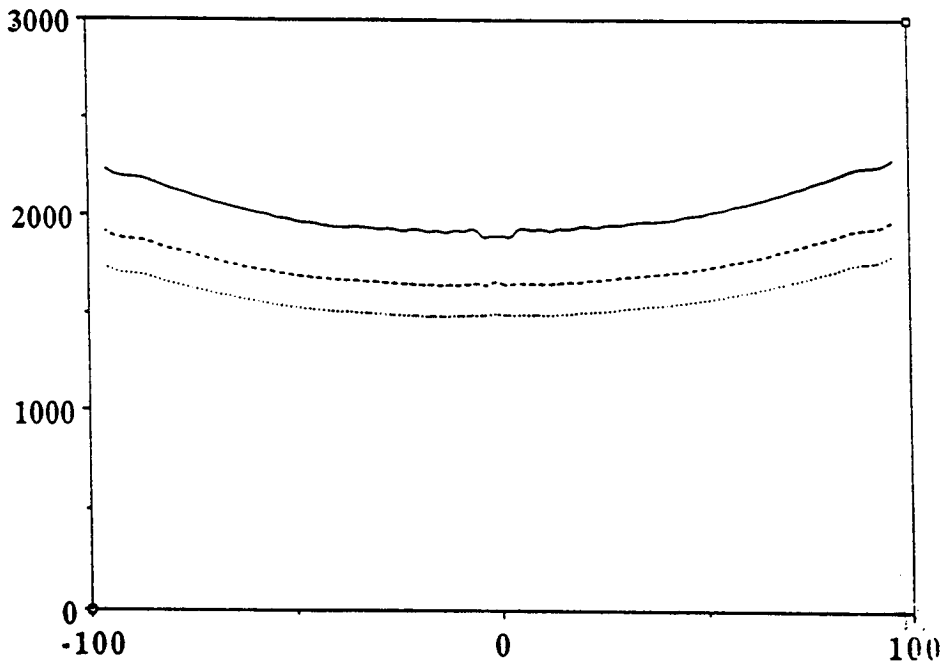


Figure 3.5.3b Plot of the function $CT(r, z, \mathcal{E}) = \int_0^\pi f(r, \phi, \mathcal{E})d\phi$ for three different energy levels at the same axial elevation.

correction function between the different SHRP asphalts, and we are confident that the same correction can be used for all asphalt cores with asphalt mass fractions in the range between 5.5% to 6.5%. Further, the procedure described in appendix B can be used for any core with diameter less than 25.4cm(10in) and it does not depend on the core height.

For determining the beam-hardening correction for coarse cores with mass fractions significantly different than $6.0\% \pm 0.5$, we propose the following procedure for performing the beam hardening correction.

A) If the mass fraction of the sample is known by some other method or by design, then a fine-aggregate core of the same mass fraction should be constructed and a calibration image should be obtained. Then ASPlab can be used to determine the kernel for correcting the images of the original core and for verifying its mass fraction.

B) If the mass fraction is not known, then ASPlab can be used first to determine a preliminary mass-fraction value, without any corrections. Then a fine-aggregate core with that preliminary mass fraction value can be constructed and then be used to obtain a calibration image.

C) If it is not possible to construct a fine-aggregate core, the ASPlab operation SELF-CALIBRATE can be used. This operation will produce qualitatively correct images, but care should be used in interpreting the mass fraction results obtained in this manner.

3.6 Determination of the Aggregate CT Numbers

As discussed earlier, determination of quantitative mass-fraction data from a set of ACT slice data requires knowledge of the CT numbers for all the different components of the core, so that these components can be properly identified during image reconstruction. In this section we present results on the SHRP aggregate CT numbers.

In our preliminary work, we determined aggregate CT numbers by locating the cross-hair cursor of the CT display directly on aggregate images inside a core and then reading off the CT number. That data was used for demonstrating that significant differences exist between the CT numbers of asphalt and of aggregates to thus allow unambiguous

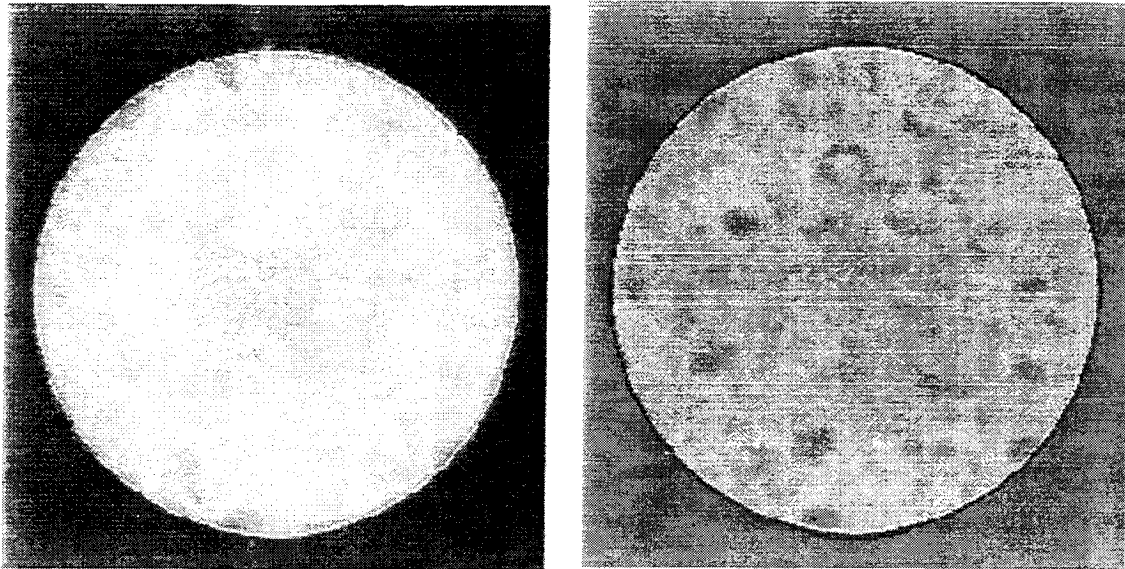


Figure 3.5.4a Two cross-sectional images of the asphalt/fine-aggregate core before and after the beam hardening correction.

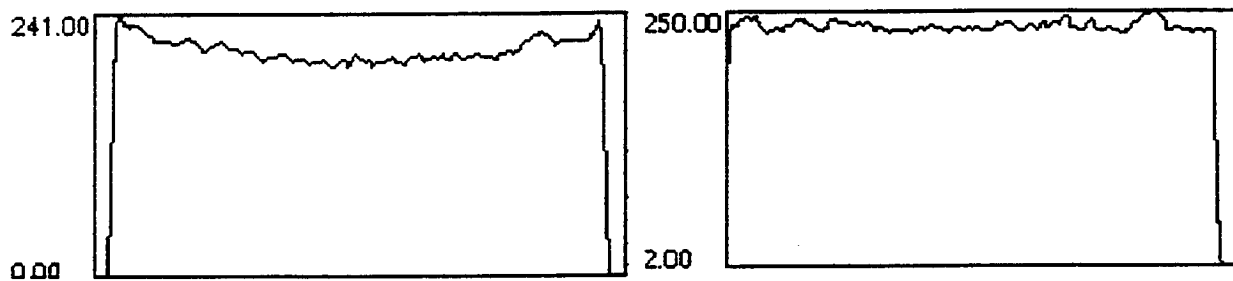


Figure 3.5.4b The variation in the CT number along a diameter of the images in Figure 3.5.4a.

identification of these components. However, when we measured the standard deviation of the CT numbers in large aggregates inside the core using the ROI operation of ASPlab, we noted that the standard deviation was relatively high, possibly because of absorption of the asphalt.

To reduce the standard deviation and to obtain more representative CT numbers, we imaged test-tubes filled with crushed aggregate grains. The data showed a substantial standard deviation probably because of the air voids entrained in the fine-grains column during packing.

Finally we performed a systematic series of tests by placing the largest size SHRP aggregate particles that would fit inside water-filled petri dishes. Figure 3.6.1 shows six of the tomograms used to obtain aggregate CT numbers. The standard deviation obtained was smaller than before and it appears possible –in some cases– to identify the aggregate type by its CT number.

Table 3.6.1 lists the CT numbers of seven SHRP aggregates using three different beam intensities. The mean values shown in the second column are mean CT values obtained by averaging CT data over an area containing the number of pixels shown in the fourth column. The third column shows the standard deviation over the same region. Even though the standard deviation is not large, it is greater than the standard deviation measured in a region of approximately the same size in a pure asphalt core.

3.7 Determination of the CT Numbers of Asphalt Mixes with Fines

As discussed in section 3.4, the smallest particle which can be detected with this protocol is $0.47\text{mm}(0.018\text{in})$. Therefore it is not possible to identify individually smaller aggregate particles inside asphalt/aggregate mixes. However, the CT number depends on the density of the material, and it is therefore plausible to attempt to determine the local particle concentration, i.e., the mass-fraction of a fine –aggregate mix from the ACT data.

Assume that the CT number of a pixel in the image is written as CT_{pixel} and assume

Table 3.6.1
Aggregate CT Numbers

	keV	Mean Value	Standard Deviation	No. of Pixels
RA	100	2475.0	48.25	234
	120	2184.0	43.25	329
	130	2015.0	41.75	284
RB	100	3157.5	48.1	622
	120	2738.0	19.9	606
	130	2530.0	19.0	571
RC	100	3130.0	37.0	286
	120	2918.0	61.0	322
	130	2699.0	57.0	302
RG	100	2900.0	95.0	428
	120	2530.0	92.0	550
	130	2350.0	73.0	348
RJ*	100	2049.7	153.0	559
	120	1816.0	105.0	484
	130	1704.3	100.3	485
RL*	100	2343.0	134.0	235
	120	2072.7	110.2	259
	130	1930.7	110.5	277

Table 3.6.1 A table of CT values for the different SHRP aggregates.

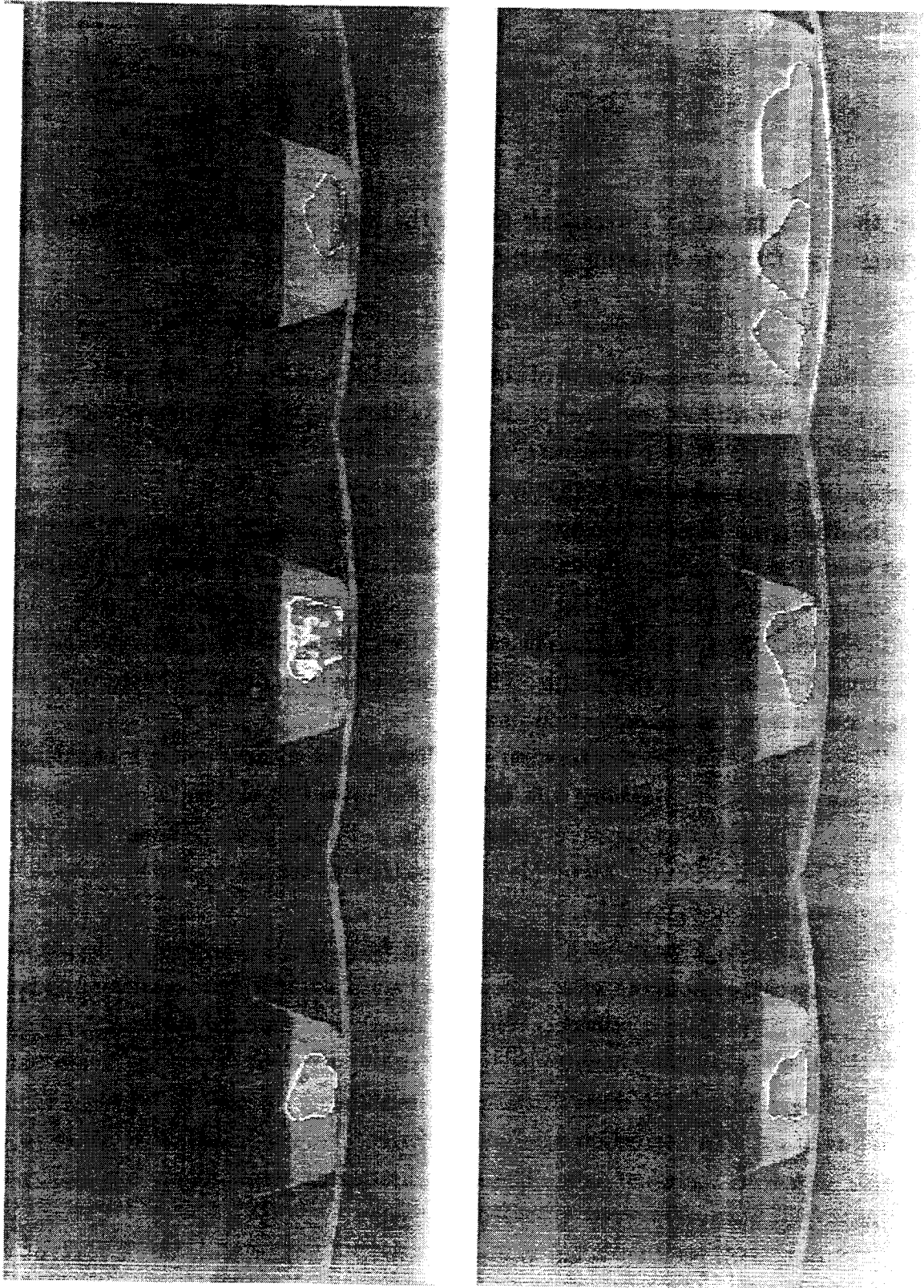


Figure 3.6.1 Six images of aggregate particles in a water bath.

that the CT numbers of the asphalt and of the aggregate are CT_{asphalt} and $CT_{\text{aggregate}}$ respectively. Then the following relationship holds true :

$$CT_{\text{pixel}} = \alpha CT_{\text{asphalt}} + (1 - \alpha) CT_{\text{aggregate}}, \quad (6)$$

where α is the local mass-fraction of the asphalt, i.e., α is the fraction of the pixel volume occupied by the asphalt and $(1 - \alpha)$ is the fraction of the pixel volume occupied by the aggregate. If a relationship between CT_{pixel} and α is established, then it should be possible to identify the mass fraction α anywhere inside the core.

To determine this relationship, twelve cores were constructed with the following asphalt mass-fraction ratios 0.04, 0.045, 0.05, 0.055, 0.06, 0.1, 0.2, 0.3, 0.4, 0.5, 0.6, & 0.7. Even though most pavements are in the 0.03 to 0.1 range, the entire series of data is needed to identify a relationship. Each core was prepared with asphalt AAG and with RC limestone aggregate crushed as fine as possible. These cores were then imaged to determine the effect of the mix density on the correction image.

The CT number for each fraction was determined without using a beam hardening correction, simply by averaging the CT number over the sample area, using the ROI operation. The experiments were performed in a double-blind fashion. The cores were prepared by the LA County Materials Lab and they were only known to us by code. The images are shown in figure 3.7.1.

Figure 3.7.1 is a print with 8 tomograms from the scans used to derive the data which are presented in figure 3.7.2. The curved surface underneath each sample is the CT gantry bed; this artifact is routinely removed from the images using the ASPlab software, when the beam-hardening correction is performed. However, since the beam hardening correction kernel for every mass fraction is determined by preparing fine-aggregate cores of that fraction, this correction was not performed here; it made little sense to correct a set of data with the same data. The beam hardening correction is only necessary for obtaining quantitatively correct coarse-core images.

Figure 3.7.2 shows the variation of the mix CT number with the % asphalt content in the mix, for three different energy levels. As expected, the CT numbers decrease as the mix density decreases, i.e., as the % asphalt content increases.

Notice that no data is shown for mass-fractions less than 10%. The 4%, 4.5%, 5%, 5.5% and 6% cores did not produce any significant differences in the CT numbers. This result

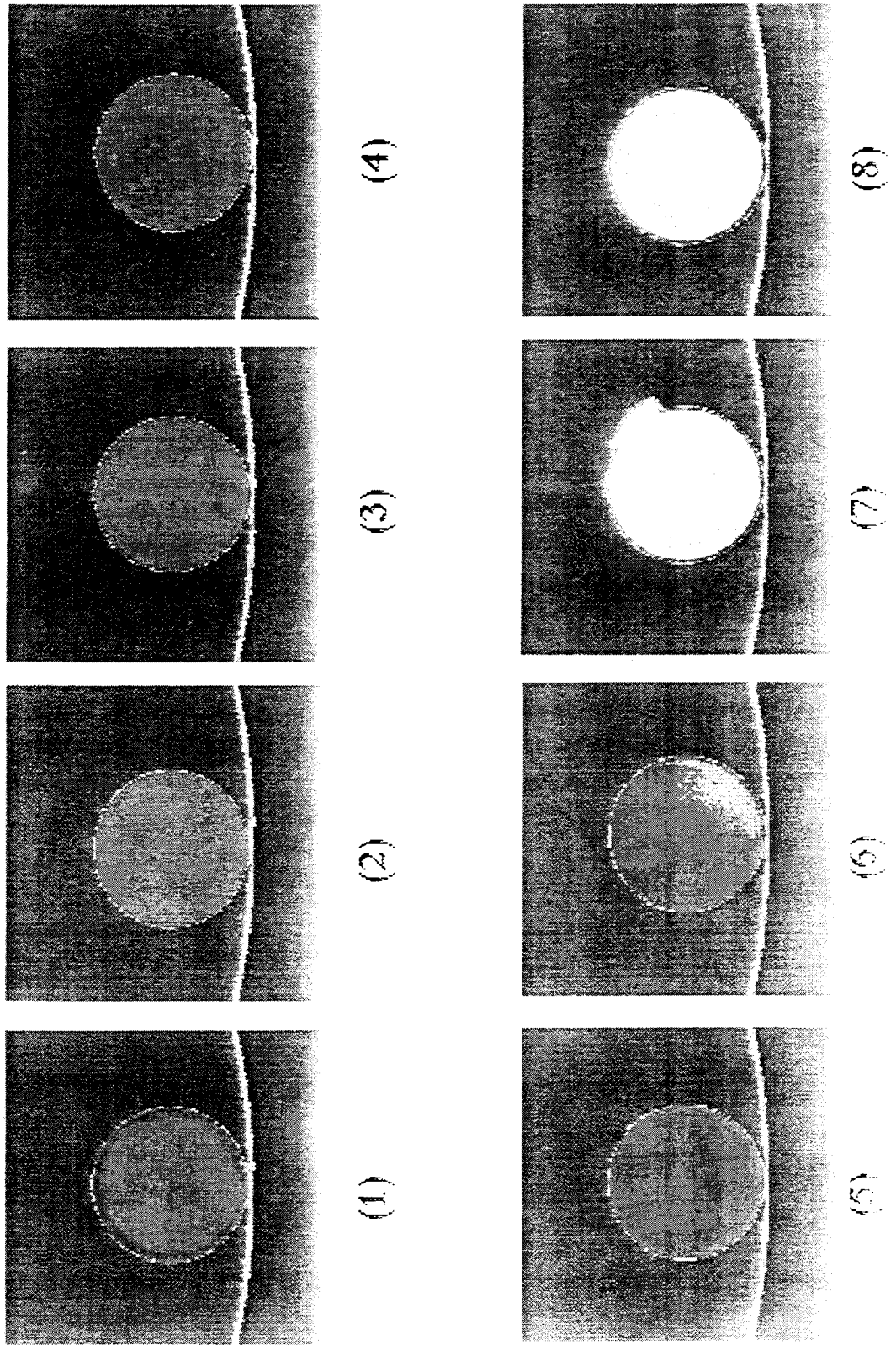


Figure 3.7.1 Tomograms of eight different fine-aggregate/asphalt cores.

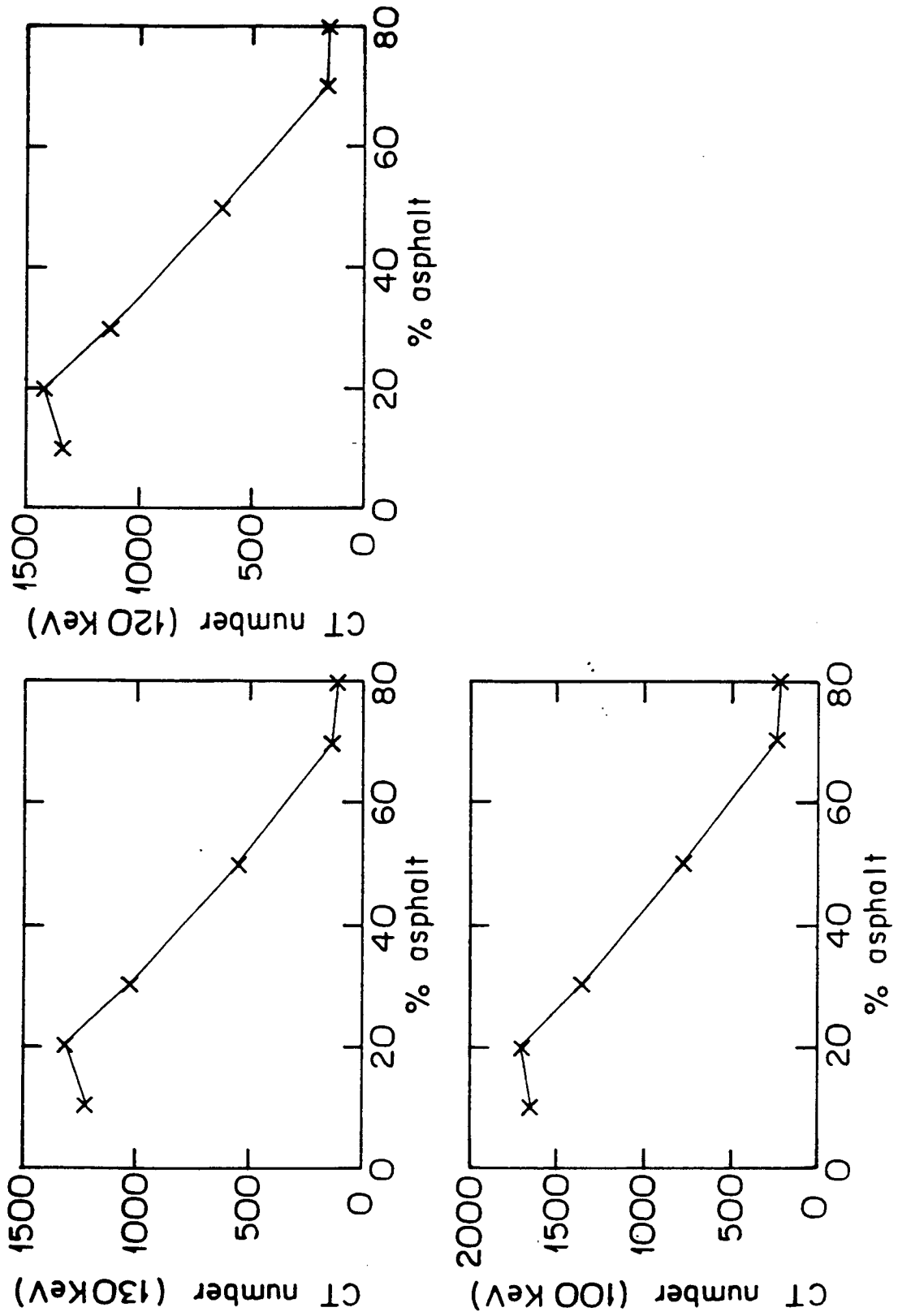


Figure 3.7.2 The variation of the CT number with the asphalt content in percentage by-weight units for three different energy levels.

implies that –in the range of mix–density values most often used in pavement–grade asphalt cores– the CT number depends only weakly on the density. Therefore the same beam–hardening correction kernel can be used for cores with different densities, as long as the core has an asphalt fraction less than 10%.

We did not perform experiments with different aggregates, but we expect the same quantitative behaviour. The fines are a small portion of the total aggregate in the mix, and small errors in determining the mass–fraction in the fines will not affect significantly the estimate of the mass–fraction for the entire core.

The CT mix–density data obtained suggest that it is only possible to identify the local mix density at any given microscopic region of the core to within 20% of the true asphalt mass fraction. However, since in most real cores the fines portion of the core is only a fraction of the overall aggregate fraction, the overall error in the determination of the aggregate mass fraction in the large aggregate/fine core is not expected to exceed 5%. For example, when imaging a 5% core, ACT should produce a result in the range 4.75% to 5.25%. Uncertainty and scatter in the CT values because of the particular aggregate type in the mix may introduce another 0.25% *absolute* error in the final mass–fraction calculation.

4. Morphological Studies and Mass Fraction Calculations

The most interesting application of asphalt core tomography is the determination of mass fractions and the visualization of large internal deformations. We will describe these results in the following sections.

4.1 The determination of the mass fraction of asphalt/aggregate cores.

With the software tools developed and the CT component data obtained, it is now possible to estimate the mass-fraction of the different components in a mixed core. This procedure involves establishing certain threshold ranges for the CT numbers of individual components in the mix and then calculating the mass-fraction from histogram of the frequency of occurrence of the different CT numbers in each set of slice data for a given core.

Using standard methods the frequency distribution of CT numbers over a core-slice was determined. Then, by establishing threshold ranges for asphalt and aggregate, the number of pixels with CT numbers in these ranges was determined. When divided by the

total number of pixels in the slice, one obtains directly the area fraction of the particular component with CT number in the range chosen. This area fraction is clearly an average of the actual volume fraction over the thickness of the individual slice. Integrating these area fractions over the entire core determines the volume fraction.

Recall that slice data are obtained at a $3mm(0.12in)$ inter-slice spacing. Therefore there are several "empty" regions in the core for which no CT data exist; however standard image reconstruction algorithms do exist for interpolating the data in these "empty" region between adjacent slices. After interpolation, it is a trivial matter to integrate and to obtain the volume fraction, i.e., the number of pixels of asphalt in the entire core is divided by the total number of pixels in the core. Multiplying this volume fraction by the known density of the asphalt in the mix produces one estimate of the asphalt mass fraction in the core.

We have incorporated in ASPlab a special operation (script) for performing mass-fraction calculations. Our algorithm is more complicated than what described above; the ASPlab script also accounts for the asphalt present in the asphalt fine-aggregate mix.

Data for two different cores are shown in table 4.1. The mixed core contains all grades of aggregate particles, while the coarse core only contained aggregate particles larger than $2mm(0.078in)$. Both cores were specifically constructed with a 6% density because this was the density for which the beam hardening correction function (section 3.5) was developed. The experiments were again conducted in double-blind fashion. The cores were only known to us by code.

Table 4.1
Determination of mass fractions for asphalt aggregate cores

	Coarse Aggregate core	Mixed Aggregate core
TRUE ASPHALT MASS	70.5g	72g
ESTIMATED ASPHALT MASS	88.5g	71.9g
TRUE AGGREGATE MASS	1105g	1128
ESTIMATED AGGREGATE MASS	1102g	1133
TRUE MASS FRACTION	6%	6%
EXTIMATED MASS FRACTION	7.2%	5.97%

It is clear that ACT adequately estimates the mass fraction of the mixed core, but that it also overestimates the fraction in the coarse core. This is not what one would expect intuitively; ACT should be less accurate when estimating the mixed core. Since the SHRP deadlines imposed on the project did not permit verification of these results with serial experiments, we are hesitant to draw definitive conclusions as to the expected error of the mass fraction calculation. Clearly more experiments are necessary. necessary to validate these results.

4.2 Visualizations of large scale deformation in two dimensions.

There are two major sets of image data which can be obtained in morphological studies beyond the usual CT slice data. One is the visualization of large-scale deformations induced by loading and the determination of aggregate-particle migration patterns; as we will report, ACT can even be used to measure the displacement field. The other is the three-dimensional visualization of the core and the calculation of image data along any arbitrary plane surface through the core. The latter is discussed in section 4.3. †

Numerous core images are presented throughout this report. An argument could be made that these images do not provide any morphological information additional to the information which can already be obtained by other imaging methods such as the dye-chemistry technique introduced by Lee et al (1983).‡ Also, there are easier standard methods for obtaining mass-fraction data. However, all other existing methods which

† In this part of our work we would like to acknowledge Professor Carl Monismith of the University of California at Berkeley of SHRP-A003 for providing us with the cores used in these tests.

‡ Note that the dye-chemistry technique does not provide any distribution data or density data for mixes with fines. Also ACT has five times higher resolution than the dye chemistry imaging method.

provide morphological data similar to that of ACT are destructive; that is to measure the data the core has to be physically destroyed. Only with ACT is it possible to obtain morphological data without altering the core structure. The non-destructive nature of ACT allows for the successive imaging of cores before and after loading and the visualization of the associated deformations and particle displacements.

To demonstrate and to evaluate the application of ACT in the visualization of large scale deformations, we obtained four $10.16\text{cm}(4.0\text{in})$ cores from SHRP-A003; these cores were known to us as only by code. The following testing protocol was used :

- 1) A metal marker particle (referred to in CT as a Bigley spot) was placed on the perimeter of the base of one of the cores to provide a reference marker for image registration.
- 2) Baseline image data was obtained for each core in the condition received.
- 3) The cores were then loaded following standard ASTM procedures up to $2.54\text{mm}(0.10\text{in})$ diametrical deformation.
- 4) Using the marker particle as a guide, the cores were placed at approximately the same place on the CT gantry and a new set of image data was obtained.
- 5) The cores were then loaded again as in step 3.
- 6) The cores were imaged again as in step 4.

A typical loading cycle for core is shown in figure 4.1; this particular test was the loading test for core B4 BOW1FD. The ordinate is the loading force applied in pounds and the abscissa is the diametrical deformation in inches. None of the four cores exhibited plastic failure during the first loading cycle. In the second loading cycle, continuous deformation of a core without any change in the loading force was considered to indicate plastic failure and it resulted in the termination of the loading test. One core (5B1WOFD) failed during the second loading cycle. Two cores had visible signs of permanent deformation after each cycle but did not fail.

Figure 4.2.2 shows a sequence of tomograms of six different cross-sections of the 5B1W0 FD core at three different loading stages. A total of forty-two cross-sectional images were obtained for every core at baseline and after each loading cycle. Figure 4.2.2a is the baseline sequence of images for the unloaded core. Figure 4.2.2b is a sequence of images of approximately the same core surface as figure 4.2.2a, after the first loading cycle. Figure 4.2.2c is a sequence of images after the core has failed. A large crack is seen in this figure The crack width varies from 1mm to $3\text{mm}(0.04\text{in})$ to $9\text{mm}(0.12\text{in})$. The crack

Data from "B4 BOW1 FD"

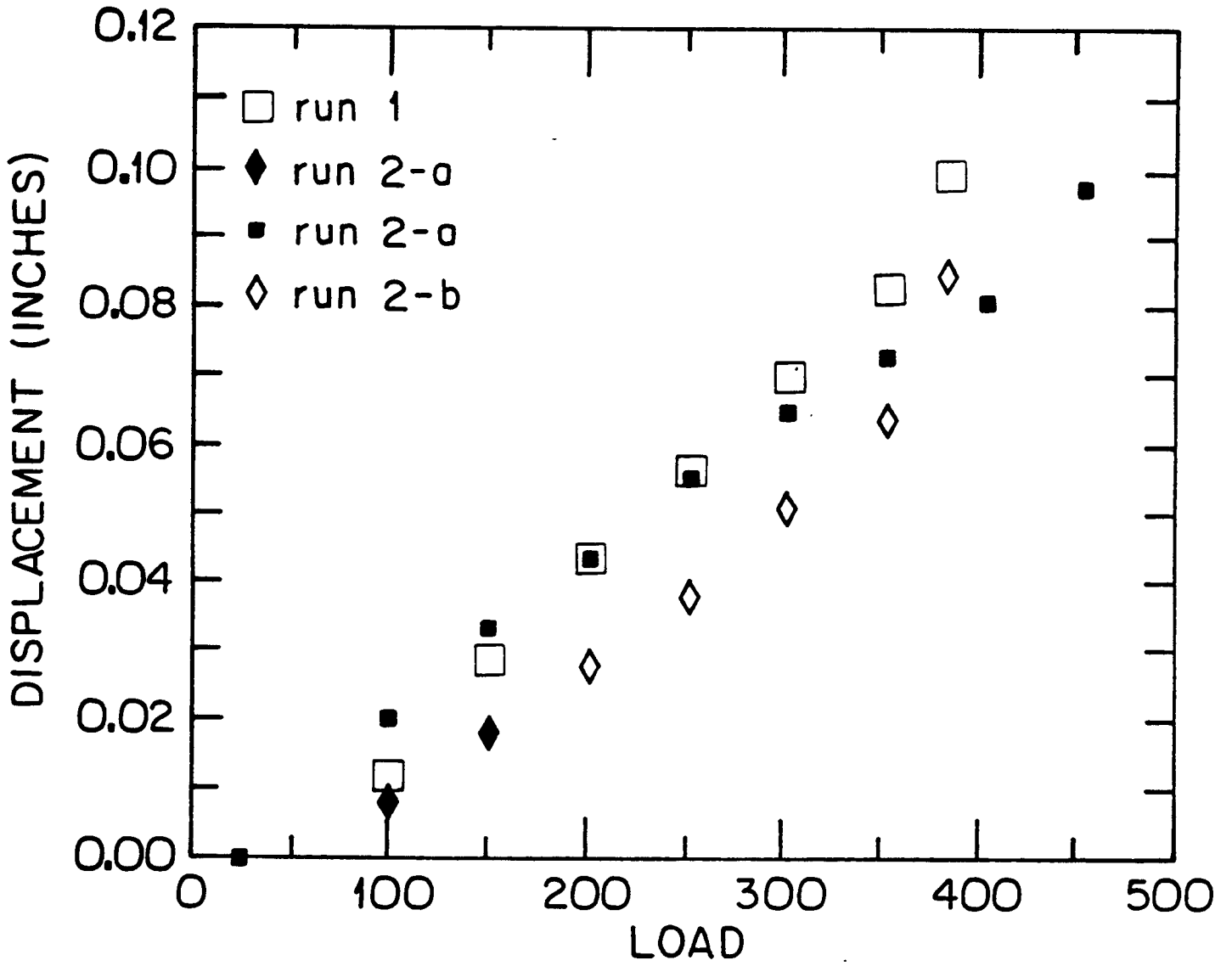


Figure 4.2.1 A typical loading curve for the A003 cores.

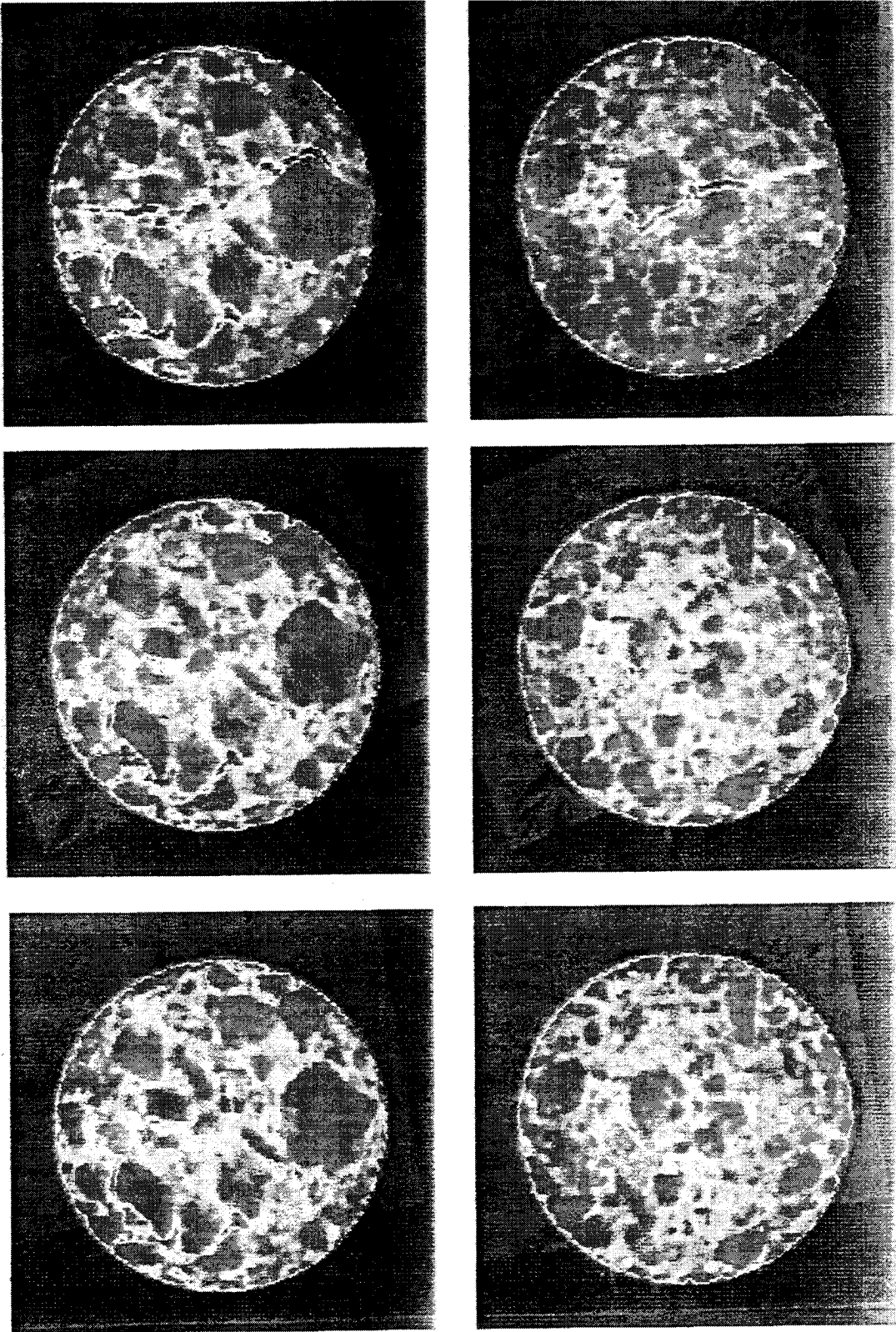


Figure 4.2.2a A sequence of tomograms of six different cross-sections of core 5B1W0FD before loading.

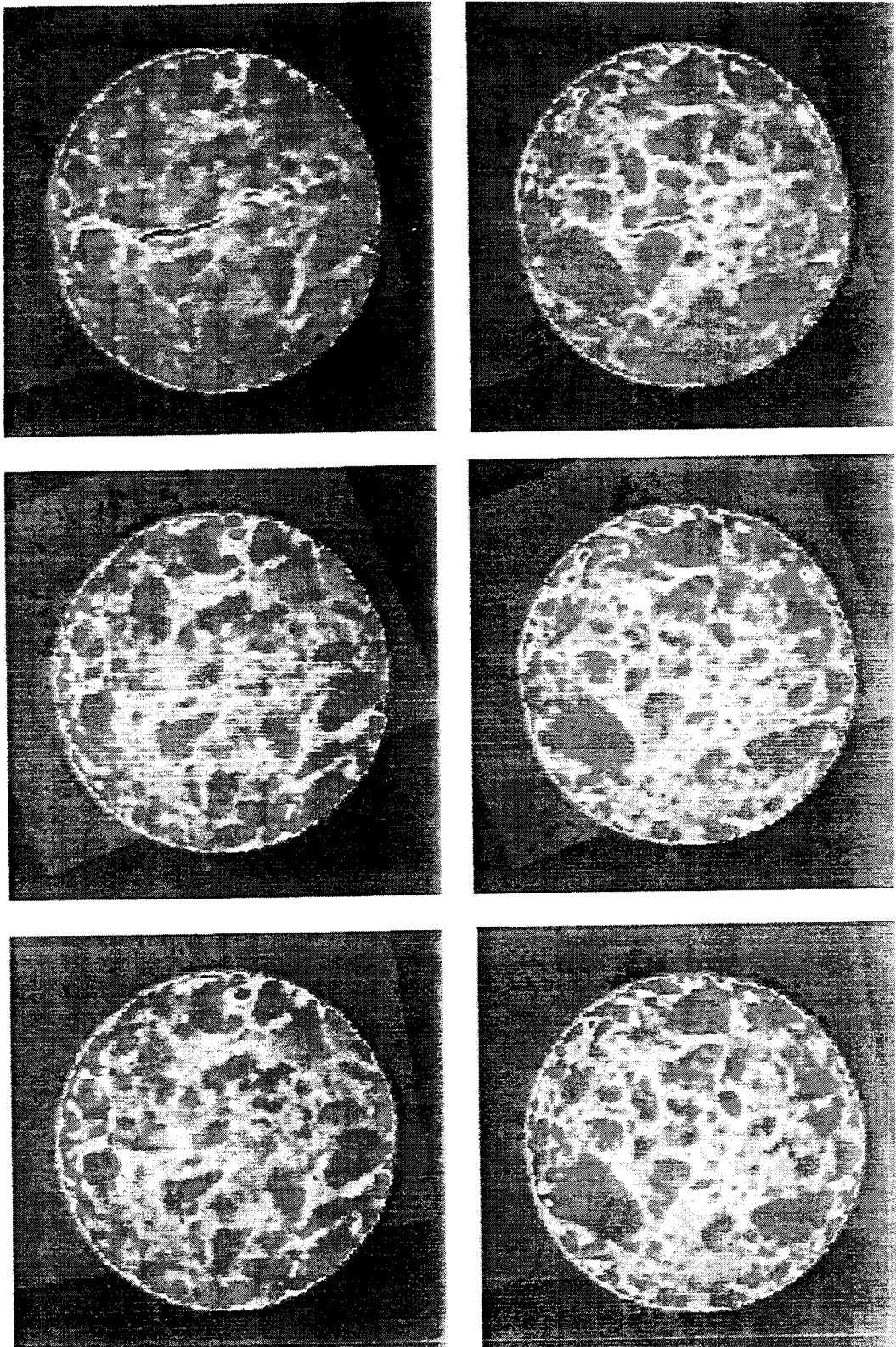


Figure 4.2.2b A sequence of tomograms of six different cross-sections of core 5B1W0FD after the first loading cycle.

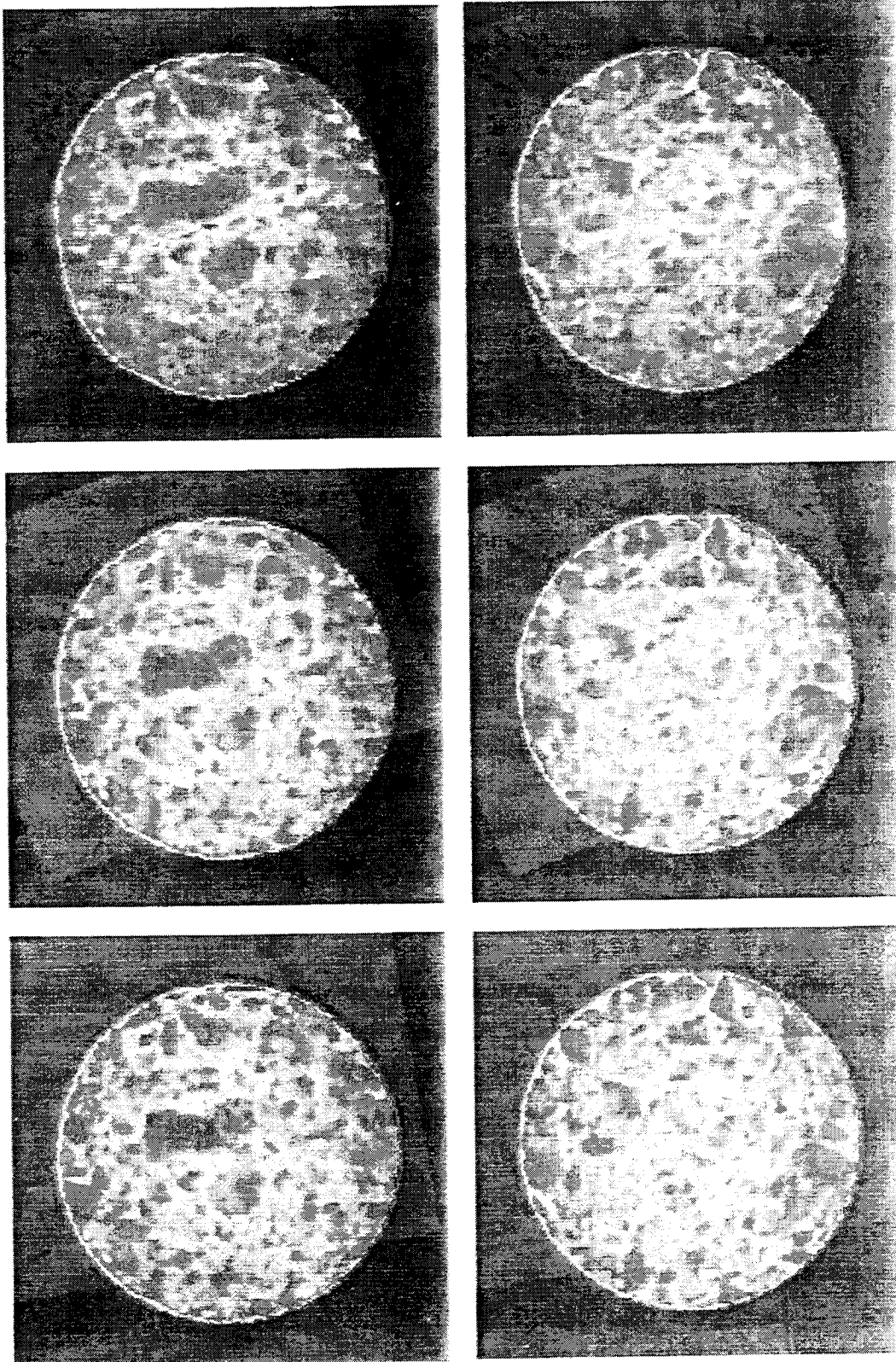


Figure 4.2.2c A sequence of tomograms of six different cross-sections of core 5B1W0FD after the second loading cycle. A large crack is visible in the upper right and left images.

propagation path is quite interesting; the crack is seen to diffract around large aggregate particles. Similar results were obtained with the other core which failed; there it is possibly to see crack bifurcation, i.e., where a crack starts branching out as the load increases.

These results are quite useful in validating finite–element models under development for studying the mechanical aspects of asphalt–aggregate interaction during loading. By digitizing the aggregate particle boundaries, it is possible to assign an initial pattern for the finite–element grids. By comparing the model results after loading with the ACT laboratory results, the validity of these models can be evaluated.

A substantial advance which was achieved in this study is the development of an image–flow analysis protocol. Optical flow analysis refers to the process of studying the motion of structures in sequences of images to determine the velocity field that produces this motion. This is a notoriously difficult problem in image processing because of the non–uniqueness of the solution. However, considerable progress has recently been achieved in studying the motion of the heart in CT chest–images (Song and Leahy, 1991).

We conjectured that ACT is an ideal application for this method. The motions are relatively small and the number of structures (aggregate particles) imposes certain constraints on the solution field, making the velocity field easier to compute. An example of the results is shown in figure 4.2.3. The vectors overlaid on the images show the magnitude and the direction of the velocity of each pixel in the image. An extensive discussion of the image–flow analysis is given in appendix A.

One useful method for visualizing flow patterns is by using the streamfunction. The two–dimensional streamfunction $\Psi(x, y)$ is defined through the equations

$$\frac{\partial \Psi}{\partial y} = u \quad \text{and} \quad \frac{\partial \Psi}{\partial x} = -v, \quad (7)$$

where u and v are the velocity components in the x and y directions along any plane. Lines of constant Ψ values are streamlines; in steady flow they are also the streaklines. In fluid flows these lines are generated by injecting dye at a specific flow location. The pattern formed by the different streamlines helps visualize the flow.

Figure 4.2.4 shows the streamline pattern for the deformation field calculated in figure 4.2.3. The flow pattern in this figure is more useful for visualizing the migration patterns of particles in the flow field.

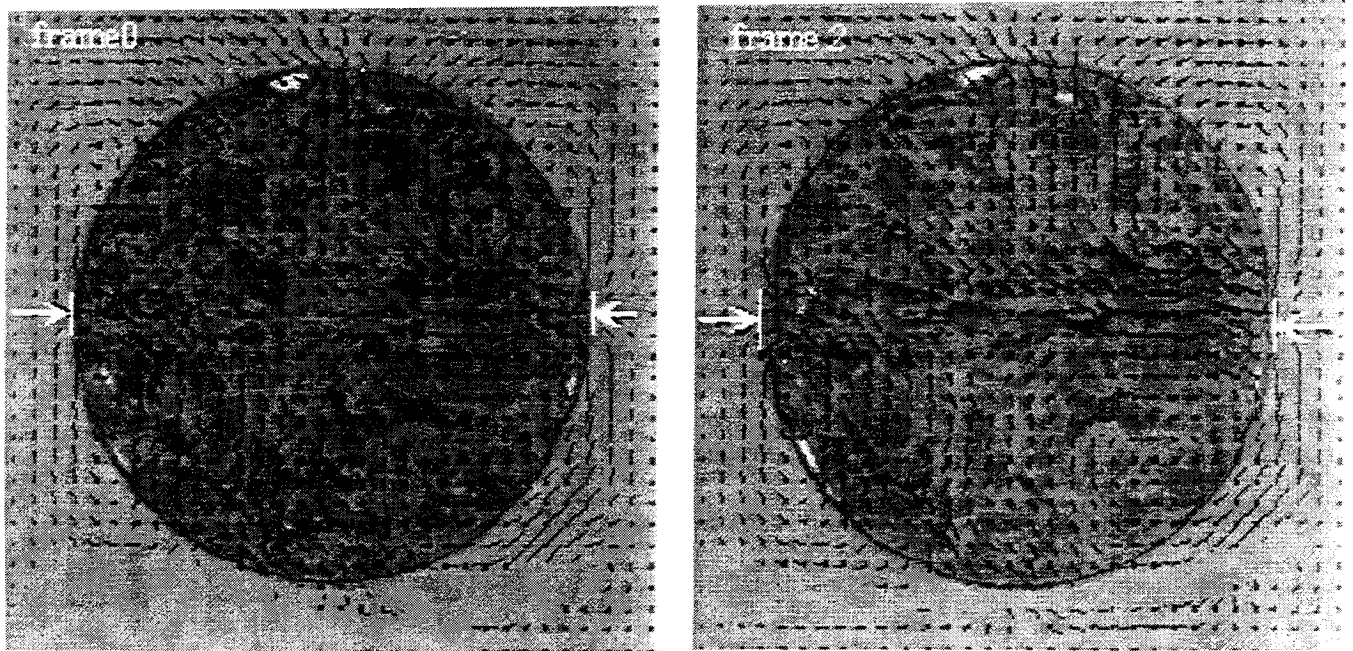


Figure 4.2.3 Demonstration of image flow calculations. Two registered color images of the core 5B1W0FD at baseline and after the second loading cycle.

4.3 Three-dimensional morphological studies.

In this section we will present data showing deformation patterns along arbitrary planes through the asphalt core.

The velocity field data presented in figure 4.2.3 were obtained with images which were identified visually as being the corresponding images using the marker particle as a reference. Image registration was not performed. Image registration is a method for referencing all CT slice data from a given CT test with respect to three-dimensional fixed coordinates (r, θ, ϕ) in the object under study.

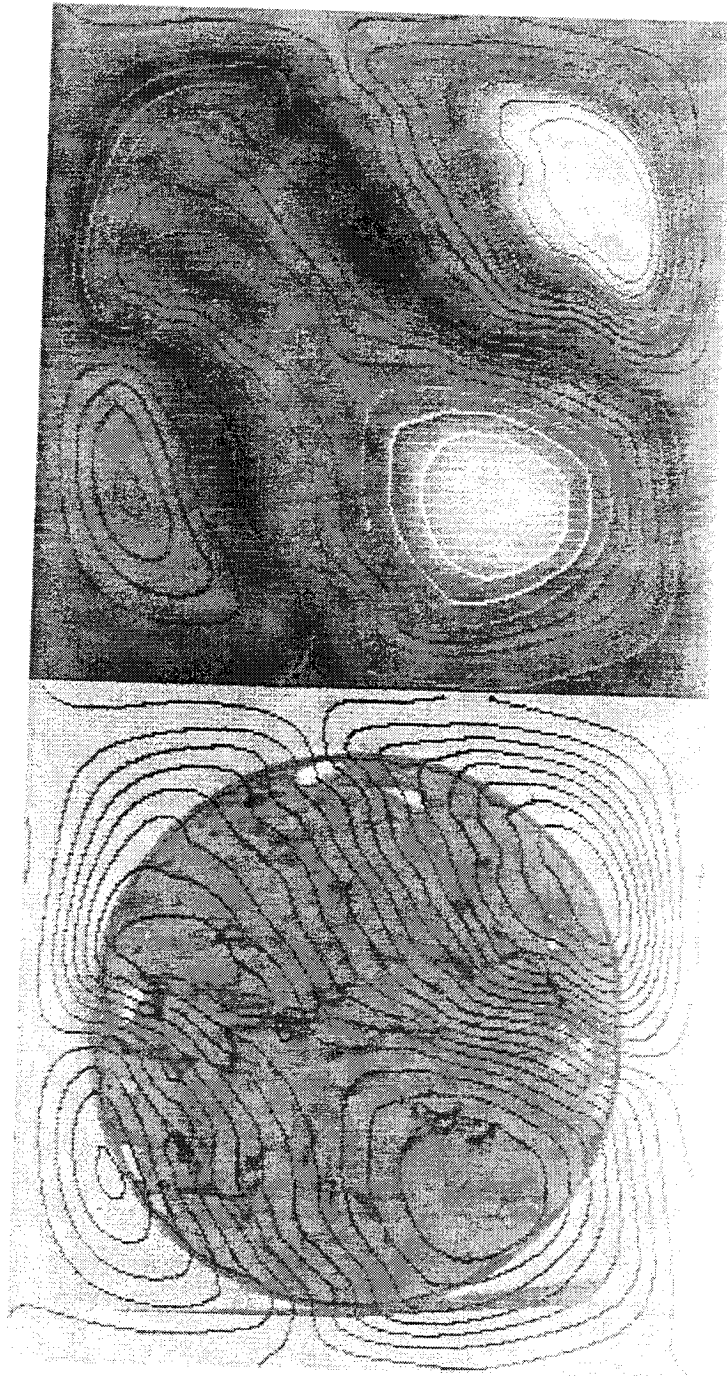


Figure 4.2.4 The streamline pattern and a color map of the streamfunction of the flow in figure 4.2.3.

Without image registration, it is only possible to determine approximate 2-D deformation fields for any given r, θ plane at any given elevation z along the core axis. It is not possible to derive deformation patterns along (r, z) planes perpendicular to the core axis for any angles θ . Even with the most careful alignment, the spatial orientation of the core is never the same in repetitive CT scans, such as performed when imaging a core before and after loading. This difference is inconsequential when looking for qualitative morphological changes, but it is a real hindrance when trying to obtain quantitative displacement data.

Using algorithms under development at the Signal and Image Processing Institute at USC, image registration for two asphalt/aggregate cores was performed. This process involves massive computation, where extrapolation methods are used to generate CT number data for the entire core with respect to the same 3-D coordinate system, even in the inter-slice region where no data was measured; in essence image registration produces a complete set of $CT(r, z, \theta)$ allowing display of CT along any arbitrary plane intersecting the core.

The results obtained by using image registration are shown in figure 4.3.1. This figure shows three columns of cross-sectional images of the same core at three different stages of loading. The plane of all these images is perpendicular to the axis of the core. The images are all accurately registered, namely there is a one-to-one correspondence between the three images along each row. These images are a refinement of the set of images shown in figure 4.2.2, where the corresponding images were identified visually by referring to the marker particle.

Figure 4.3.2 presents cross-sectional reconstruction data along one azimuthal (r, z) plane. The three images shown are all synthesized from individual CT slice data. The last image clearly shows a crack which was neither visible from the outside nor in the individual slice data.

It should be emphasized that image registration is necessary for three-dimensional visualization of asphalt cores and it is highly desirable for performing optical flow calculations. However, this approach is not necessary for other morphological studies, such as visualization of deformations and for measurements of the mass fraction.

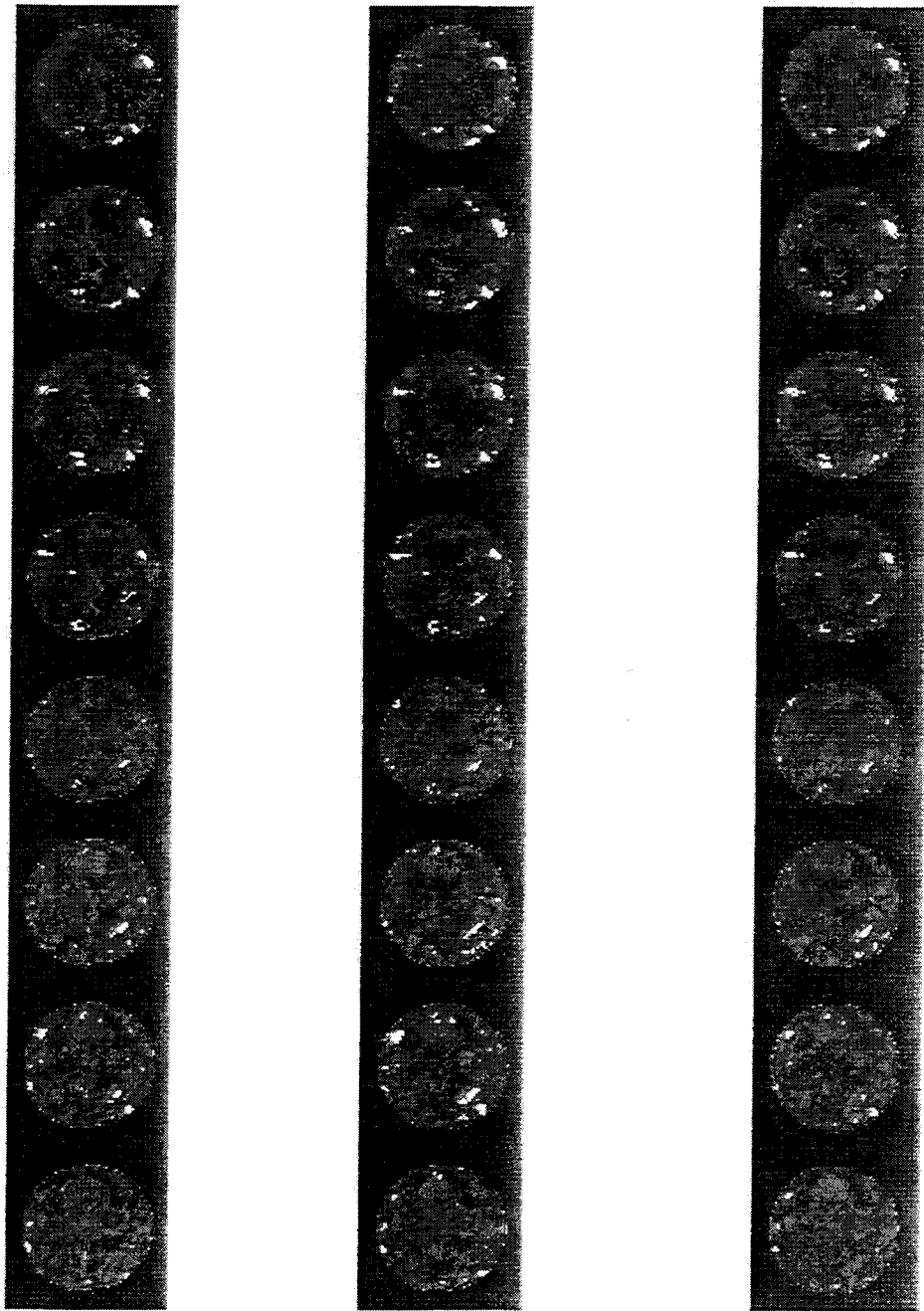
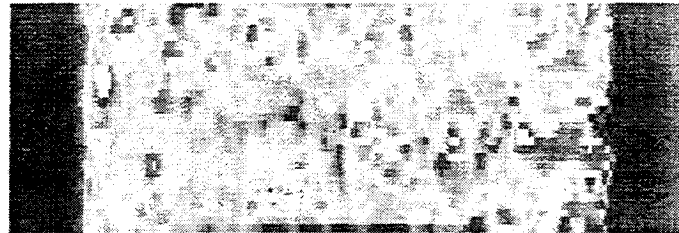
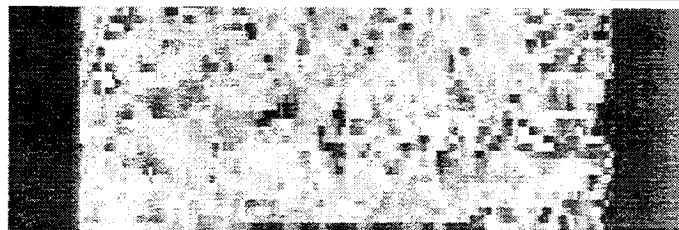


Figure 4.3.1 Three series of eight properly registered CT images of core 5B1W0FD at three different stages of loading. The images are taken along planes (r, θ) perpendicular to the core axis z .



a) baseline image before loading



b) image after first loading cycle



c) image after second loading cycle

Figure 4.3.2 Three properly registered CT images of core 5B1W0FD at three different stages of loading. The images are taken along a plane through the core axis, i.e., along the azimuthal (r, z) plane.

4.4 Special Topics

In this section we will briefly describe two further studies using ACT. In the 4.4.1 we will discuss imaging of voids networks. In 4.4.2 we will discuss the applicability of magnetic resonance imaging in asphalt studies.

4.4.1 Voids network visualization.

One interesting application of ACT would be the mapping of the voids network in an asphalt core. The standard existing method is the modified Lottman test protocol, where the core is saturated with water and then the voids volume is determined by measuring the volume of water used in the saturation. This test does not provide any quantitative data on the distribution of voids through the core, and, if the voids network is not connected, it may not provide an accurate measurement of the voids network.

For this study, we obtained specially prepared briquettes from Professor Ron Terrel fabricated with asphalt AAG-1 and RB aggregate with 7.4% and 7.8% air voids. The testing protocol was the following :

- 1) Baseline data was obtained from the unsaturated briquettes.
- 2) The briquettes were saturated using the modified Lottman (modified AASHTO T-283) procedure.
- 3) CT scan data were obtained from the saturated briquettes.
- 4) Image registration was performed for the baseline data and for the saturated data sets.
- 5) The two sets of registered images were digitally subtracted from each other.

The saturated images of the briquettes were darker than the baseline unsaturated images, indicating a higher water content. After subtraction, the resulting set of images

suggested a residual water distribution though the core. While, this pattern could be interpreted as the voids network, we are very hesitant to conclude that this data set is an actual representation of the network. Our procedure is highly dependent of image registration. Misregistration even by one pixel between the before and after saturation images will produce similar results. Considerable more effort is needed to eliminate misregistration as a cause for the observed patterns. It is therefore premature to draw any conclusions as to the usefulness of ACT in studying voids networks.

4.4.2 Magnetic resonance imaging of asphalt cores.

We will briefly describe our results, without going into the details of the principles of operation of magnetic resonance imaging (MRI) which are quite different than x-ray CT. Understanding of this section presupposes some knowledge of MRI.

The protocol outlined in section 4.4.1 was repeated using a 1.5*Tesla* MRI scanner. Based on preliminary calculations, it was anticipated that the cores had short T_2 and long T_1 relaxation times. Spin-echo sequences with a short echo time $T_e \approx 20ms$ and long repetition time $TR \approx 3s$ were used with several combinations of sequence parameters. No measurable NMR signals were resorted. To investigate the causes for the weakness of the signals, the cores were placed in a water bath. The resulting images showed considerable distortions inside the water volume of the water bath suggesting that the cores contained sufficiently large amounts of ferromagnetic materials, rendering MRI imaging ineffective.

Conclusions

1. Asphalt Core Tomography (ACT) can be used effectively and routinely in morphological studies, i.e. in visualizing quantitatively the interior structure of asphalt cores.
2. ACT is superior to the dye-chemistry technique, the only existing alternative for the visualization of the interior of cores; ACT's resolution is one order-of-magnitude higher, and ACT does not destroy the core structure in the testing process.
3. Using ACT, it is possible to visualize large scale deformations which occur under loading and to measure the propagation and geometric characteristics of cracks down to $1mm(0.025in)$ size.
4. Using the algorithms developed for three-dimensional image reconstruction, it is possible to detect internal cracks parallel and perpendicular to the core axis.
5. ACT can be used to complement chemical stripping methods to determine the mass fraction of asphalt in an asphalt/aggregate core.
6. Large scale deformation results obtained with ACT can be used to validate finite-element models under development to predict the displacement fields under loading.

Recommendations

1) We recommend that an x-ray commercial CT system be acquired by at least one SHA and/or the FHWA. We have found x-ray CT is a very useful and effective analytical tool for concrete pavement and asphalt pavement forensic studies. Certain commercial x-ray CT systems are now priced below \$500,000 and they do not require a radiation technologist for operation. ACT could eventually become a standardized test for core studies.

2) SHRP or FHWA should conduct a one or more day workshop to acquaint engineers in materials labs of the SHA with asphalt core tomography and its uses in complementing and in validating existing testing methods. SHA should have at least one engineer who is familiar with ACT and the ACT testing protocol. This person could interface with a local hospital or medical center and could implement core tests on an as-needed basis. We estimate the cost of having a medical center's radiology department to scan a core at off-peak hours and to provide a data set of twenty five slice images to be less than \$400.

3) We recommend that ACT be used routinely to screen core samples –such as those from the LTPP study– prior to performing additional standard destructive tests. The objective would be to detect any unexpected anomalies which might unduly influence the results. For example, ACT could detect samples with large voids or large aggregates of unusual shape which would not be representative of the pavement under study; data from these core samples would be treated with caution or the samples would be discarded. Using ACT for screening samples would provide greater confidence in extrapolating performance

data based on small number of core data.

4) We suggest that ACT be used as an alternative to the dye-chemistry technique.

5) We recommend that ACT be used as a complementary test to chemical stripping tests. There is the possibility that the solvents used in the stripping tests will be more strictly regulated in the future. Preliminary results with ACT indicate that it provides similar information to a chemical-stripping test without any emissions.

6) ACT may prove to be quite useful for analyzing modified asphalt cores not conducive to conventional chemical stripping techniques.

References

Asphalt core tomography is an entirely novel application of computer tomography in asphalt testing. Consequently we only had a very small number of published studies that were applicable in this research. Signal processing-specific references are listed in the next section which discusses the optical flow calculations.

1. – Davison, M. (1982) X-Ray computed tomography, in *Scientific basis for medical imaging*, H.T. Wells editor, 54–92. Churchill and Lighthill, London, 560pp.
2. – Kak, A.C. (1979) Computerized Tomography with X-Ray, Emission CT and Ultrasound Sources, *Proce IEEE*, **9**, 1245–1272.
3. – Lee, T-C, Terrel, R.L. and Mahoney, J.P. (1983) Measurements of mixing efficiency in pavement recycling, *Asphalt Paving Technology*, **52**, 61–87.

References for Appendix A

- [1] S. M. Song and R. M. Leahy, *Computation of 3-D Velocity Fields from 3-D Cine CT images of a Human Heart*. in *IEEE Tran. Medical Imaging*, vol. 10, No. 3. Sept 1991 pp. 295-306
- [2] A. N. Tikhonov and V. Y. Arsenin, *Solutions of Ill-Posed Problems*. Washington, DC: Winston and Sons, 1977.
- [3] J. Hadamard, *Lecture on the Cauchy Problem in Linear Partial Differential Equations*. New Haven, CT: Yale University Press, 1923.
- [4] B. K. P. Horn and B. G. Schunck, "Determining optical flow," *Artificial Intelligence*, vol. 17, pp. 185-203, 1981.
- [5] B. G. Schunck, "Image flow: fundamentals and future research," in *Proc. IEEE Conf. Comp. Vision and Patt. Rec.*, vol. CVPR-85, (San Francisco, CA), pp. 560-571, 1985.
- [6] W. Enkelmann, "Investigations of multigrid algorithms for the estimation of optical flow fields in image sequences," *Comp. Vision, Graphics and Image Proc.*, vol. 43, pp. 150-177, 1988.
- [7] H. Nagel, "On a constraint equation for the estimation of displacement rates in image sequences," *IEEE Trans. Pattern Anal. Machine Intell.*, vol. 11, no. 1, pp. 13-30, 1989.
- [8] J. Aisbett, "Optical flow with an intensity-weighted smoothing," *IEEE Trans. Pattern Anal. Machine Intell.*, vol. 11, no. 5, pp. 512-522, 1989.
- [9] G. E. Mailloux, A. Bleau, M. Bertrand, and R. Petitclerc, "Computer analysis of heart motion from two-dimensional echocardiograms," *IEEE Trans. Biomed. Engr.*, vol. BME-34, no. 5, pp. 356-364, 1987.
- [10] G. E. Mailloux, F. Langlois, P. Simard, and M. Bertrand, "Restoration of the velocity field of the heart from two-dimensional echocardiograms," *IEEE Trans. Med. Imaging*, vol. 8, no. 2, pp. 143-153, 1989.
- [11] D. C. Youla and H. Webb, "Image restoration by the method of convex projections: Part 1: Theory," *IEEE Trans. Med. Imaging*, vol. MI-1, no. 2, pp. 81-94, 1982.
- [12] S. C. Hunter, *Mechanics of Continuous Media*. New York: John Wiley and Sons, 2nd ed., 1983.

- [13] L. A. Segel, "An introduction to continuum theory," in *Modern Modeling of Continuum Phenomena* (R. C. DiPrima, ed.), pp. 1-60, American Mathematical Society, 1986.
- [14] J. M. Fitzpatrick, "A method for calculating fluid flow in time dependent density images," in *Proc. IEEE Conf. Comp. Vision and Patt. Rec.*, vol. CVPR-85, (San Francisco, CA), pp. 78-81, 1985.
- [15] J. M. Fitzpatrick, "The existence of geometrical density-image transformations corresponding to object motion," *Comp. Vision, Graphics and Image Proc.*, vol. 44, pp. 155-174, 1988.
- [16] J. M. Fitzpatrick and C. A. Pedersen, "A method for calculating velocity in time dependent images based on the continuity equation," in *Proc. Electronic Imaging '88*, pp. 347-352, 1988.
- [17] R. P. Feynman, R. B. Leighton, and M. Sands, *The Feynman Lectures on Physics*, vol. 2. Menlo Park, CA: Addison-Wesley, 1964.
- [18] G. D. Smith, *Numerical Solution of Partial Differential Equations: Finite Difference Methods*. Oxford: Oxford University Press, 1983.
- [19] D. G. Luenberger, *Linear and Nonlinear Programming*. Menlo Park, CA: Addison-Wesley, 2nd ed., 1984.
- [20] B. R. Hunt "The application of constrained least squares estimation to image restoration by digital computer," *IEEE Trans. Computers*, vol. C-22, no. 9, pp. 805-812, 1973.
- [21] D. G. Luenberger, *Optimization by Vector Space Methods*. New York: John Wiley, 1969.

Appendix A

Computation of the 3-D displacement fields from a sequence of 3-D x-ray CT scans of a deforming asphalt core

Samuel M. Song Richard M. Leahy Costas E. Synolakis

Abstract

The motion of a deforming body is completely characterized by the velocity field generated by its motion. A method of computing the three dimensional velocity field from a sequence of three dimensional CT images of a deforming asphalt core is described. The first image in the sequence is generated by scanning a cylindrical core. Subsequent images are generated by scanning the same core after each of a series of diametal loading tests. The objective is to quantify the local deformation of the core as a function of position

inside the core. This technique has potential applications in the study and modeling of thermal cracking, rutting and other failure mechanisms in asphalt structures.

The continuum theory provides two constraints on the velocity field generated by a deforming body. Assuming that (1) the image is proportional to some conserved quantity and (2) the imaged medium is incompressible, the velocity field satisfies the *divergence-free constraint* and the *incompressibility constraint*. Computation of the velocity field from image data using only these two constraints is an *ill-posed* problem which may be *regularized* using a smoothness term. The determination of the solution involves minimization of a penalty function which is the weighted sum of the two constraining terms and of the smoothness terms.

It can be shown that the solution minimizing the penalty satisfies the Euler-Lagrange equations for this problem. The solution of the Euler-Lagrange equation is a set of coupled elliptic partial differential equations (PDEs). For numerical implementation, these PDEs are discretized into a system of linear equations $\mathbf{Ax} = \mathbf{b}$ where \mathbf{x} is the solution velocity field. The matrix equation is solved using the conjugate gradient algorithm.

Solutions of motions from a synthetic sequence of images are presented to validate the method. Then the method is used to calculate the deformation field between sets of CT images from deforming asphalt cores.

1. Introduction

X-ray computed tomography (CT) is a diagnostic tool developed for producing cross-sectional images of the human head or body. The reconstructed CT images are proportional to the spatial distribution of the linear x-ray attenuation coefficient within the imaged slice. Since attenuation coefficients vary with tissue type (e.g. blood, muscle, fat, bone), these images provide valuable anatomical information.

Applications of CT are not limited to human studies. A medical CT scanner may be used for NDE imaging of any object of similar or smaller dimensions as the human body, provided the x-ray attenuation coefficients of the constituents of the object are similar as that of human tissues. Large commercial CT scanners are now available that can image even entire airplane wings. In order to obtain useful information from any of these images, the attenuation coefficients of the different constituents must be sufficiently different so the resulting images exhibit identifiable contrast between structures in the object. The main report describes the ACT protocol for imaging asphalt cores.

Since CT is a non-destructive imaging modality, it is possible to repeatedly scan the same core over time and to identify internal changes. The purpose of this appendix is to describe a method for quantification of the changes which are often identified in a series of images of the same core taken over time as the core is degrading. The method is applied in the calculation of the spatial deformation of the core due to the application of a diametal load; however it can be used to study changes due to thermal rutting or cracking. The loading tests used to generate the series of images is discussed in section 4.2 of the main report. Visual inspection of the images presented there reveals the complex nature of the deformation in an inhomogenous core.

For every pixel in a series of registered CT images, our method computes a vector indicating the direction and magnitude of the displacement of that pixel between any pair of 3-D images in the sequence. This vector deformation field is referred to in the following as the "velocity field", because the velocity field can be derived directly from the displacement field by division by the time interval between the pairs of images used for the calculation of the field.

The problem of estimating motion from a sequence of images is often *ill-posed*[1] in the

sense of Hadamard [2] Horn and Schunck [3] reported the first computational algorithm for computing a 2-D velocity field from a sequence of 2-D images using a method commonly referred to as *optical flow*. They used Tikhonov's [1] regularization method. Several variations on the original optical flow algorithm have since been proposed [4,5,6,7].

The optical flow algorithm of Horn and Schunck[3] computes a velocity vector for every pixel in the image. The *brightness constraint* introduced in [3] is based on the assumption that a 'point' in a sequence of images does not change in its gray level from one frame to the next. However, this brightness constraint alone can not provide a unique solution for the velocity field. By incorporating a regularization or smoothness measure on the velocity field (thereby implicitly assuming the true field to be spatially smooth) and by minimizing a weighted sum of the smoothness term and the error in the brightness constraint, the 2-D velocity field can be computed from a sequence of 2-D images.

An example of the application of this approach to image sequences obtained from a medical imaging device is described by Mailloux *et al*[8,9] for automated motion quantification of a beating heart using echocardiograms. In [8], the optical flow method in [3] was applied directly to two-dimensional echo images with favorable results. In [9], the velocity field was assumed to be locally linear and the solution constrained to lie on the set of linear vector fields. The linearity constraint and both the brightness and smoothness constraints of optical flow can all be shown to be convex. Therefore, by using *projections onto convex sets* (POCS)[10], the velocity field as now been computed for all components of the linear velocity field: translational, rotational, divergent and shear. One limitation of the results reported by Mailloux *et al* is that they are only 2-D approximations of the true 3-D field.

Since the deformation of the asphalt core is intrinsically three-dimensional, we formulate and solve the problem directly in 3-D. The formulation is derived from a physical model for the motion of the imaged medium using continuum theory[11,12]. Fitzpatrick first in suggested using continuum theory for the velocity computation problem from a sequence of images. In his seminal work[13], he points out that for images whose grey level intensity is proportional to the density of some conserved quantity then *equation of continuity* found in classical continuum theory can be solved to yield the velocity field generated by the motion in the imaged medium . In addition, if the imaged medium is incompressible, the incompressibility condition of continuum theory is also applicable [14].

When studying motion of particles in a two dimensional plane of a three dimensional

object, the the equation of continuity and the two-dimensional form of the incompressibility condition may not be strictly valid , since the motion may not be confined to the 2-D slice. For this reason, motion estimation is addressed here as a three dimensional problem.

In Section 2 presents a brief review of continuum theory [11,12] as it applies to 3-D density images. Using this theory, we develop two constraints on the 3-D velocity field associated with the deforming asphalt core. With these constraints, the computation of the 3-D velocity field is formulated in section 3 as an optimization problem and a solution to the optimization problem is developed using the Euler-Lagrange method. The solution is then discretized for computer implementation. In section 4 the results are validated using simulated series of images. Finally the optical flow algorithm is applied to determine the velocity field of a deforming asphalt core. The following presentation introduces a large number of variables. These variables are defined below.

List of variables

- $\mathbf{r} = (x, y, z)$: spatial variables or coordinates
- $\mathbf{R} = (X, Y, Z)$: material variables or initial position
- t : time
- $\mathbf{s}(\mathbf{r}, t) = (u, v, w)$: velocity in Eulerian Description
- $\mathbf{S}(\mathbf{R}, t)$: velocity in Lagrangian Description
- f : density image
- $D/Dt g$: mobile derivative of g with respect to t
- $g_x = \partial g / \partial x$: partial derivative of g with respect to x
- $\nabla = (\partial / \partial x, \partial / \partial y, \partial / \partial z)$: gradient operator, spatial
- $\nabla \cdot$: divergence operator
- (T_x, T_y, T_z) : spatial extent of the imaging experiment
- $\Omega = [0, T_x] \times [0, T_y] \times [0, T_z]$, imaging volume
- $\partial \Omega$: surface enclosing Ω
- $d\Omega = dx dy dz$: differential volume element
- e_S : cost pertaining to smoothness of $\mathbf{s} = (u, v, w)$
- e_I : cost pertaining to incompressibility constraint

- e_D : cost pertaining to divergence-free constraint
- γ_1 : regularization parameter for e_I
- γ_2 : regularization parameter for e_D
- \mathbf{f} : discrete version of image f
- \mathbf{x} : discrete version of the velocity field $\mathbf{s} = (u, v, w)$

2 Constraints on the Velocity Field

In this section we present two constraints which may be applied to the velocity field of the deforming core. These constraints are developed within the framework of continuum theory. A fundamental assumption in the following is that the data are *density images* in the sense defined by Fitzpatrick [15], i.e., the images represent some conserved quantity. CT image intensities are proportional to the linear attenuation coefficient. This coefficient is a time-invariant function of the chemical composition of the core. It is therefore reasonable to assume that the CT image represents a conserved quantity. A mathematical definition of density images and the conservation property is given in section 2.2.

2.1 Descriptions of Motion of Deformable Media

Consider a physical body occupying a region $\mathcal{V} \subset \mathfrak{R}^3$. This body is in motion and is subject to deformation. The region \mathcal{V} consists of points or particles that can be associated with the position vector $\mathbf{R} = (X, Y, Z)$ in one-to-one correspondence. Therefore the mapping ‘particle $\rightleftharpoons \mathbf{R}$ ’ is bijective so that each particle is uniquely labeled with a position vector \mathbf{R} .

Let a physical body at time t_0 occupy a region \mathcal{V}_{t_0} and at time t , through motion, occupy a new region \mathcal{V}_t . Then the particle with label $\mathbf{R} = (X, Y, Z) \in \mathcal{V}_{t_0}$ will have moved to a new position $\mathbf{r} = (x, y, z) \in \mathcal{V}_t$. We describe this mapping by

$$\mathbf{r} = \mathbf{r}(\mathbf{R}, t) \tag{1}$$

The mapping $\mathbf{r}(\mathbf{R}, t)$ describes the path of the particle initially located at \mathbf{R} . Therefore, it is natural to define the velocity \mathbf{S} at time t of the particle with label \mathbf{R} as follows.

$$\mathbf{S}(\mathbf{R}, t) = \frac{\partial}{\partial t} \mathbf{r}(\mathbf{R}, t) \tag{2}$$

Further, we assume that the particle with label at \mathbf{R} moves to only one \mathbf{r} and conversely, no two particles with different labels arrive at the same \mathbf{r} at the same time. This assumption is the principle of *impenetrability of matter*. Then, the inverse mapping of (1) exists and a pair of invertible mappings are described below.

$$\mathbf{r} = \mathbf{r}(\mathbf{R}, t) \quad \text{and} \quad \mathbf{R} = \mathbf{R}(\mathbf{r}, t) \quad (3)$$

The above pair of invertible mappings depict the transformation between *spatial description* and *material description*. These are also called *Eulerian* and *Lagrangian* descriptions respectively. In spatial description, the independent variable is \mathbf{r} —the spatial variable. In material description, the independent variable is \mathbf{R} —the material variable. In both cases, t is an independent variable.

In most imaging experiments, pixels or voxels are fixed to a laboratory frame of reference. The motion of the imaged medium is observed with respect to this laboratory frame in which the pixels are fixed. Therefore, the convenient description of motion in most imaging applications seems to be the spatial description. This is the case for the problem of computing the velocity field within the imaging volume. We must express $\mathbf{S}(\mathbf{R}, t)$ in (2) in terms of the spatial variable \mathbf{r} —the pixel coordinates.

Using (3), the velocity may be expressed in terms of the spatial variable \mathbf{r} as below.

$$\mathbf{s}(\mathbf{r}, t) = \mathbf{S}(\mathbf{R}, t) |_{\mathbf{R}=\mathbf{R}(\mathbf{r}, t)} = \mathbf{S}(\mathbf{R}(\mathbf{r}, t), t) \quad (4)$$

This is the spatial description of the particle velocity. In other words, $\mathbf{s}(\mathbf{r}, t)$ is the velocity of the particle passing through the spatial position \mathbf{r} at time t .

2.2 The Equation of Continuity

In this section, we present the *continuity equation* using the conservation of mass. Consider a region \mathcal{V} with a density distribution $f(\mathbf{r}, t)$. Let m be the volume integral of f over \mathcal{V} . If f represents the mass density then m is the total mass in \mathcal{V} . The rate of change in m (within a fixed arbitrary volume \mathcal{V}) is given by

$$\frac{dm}{dt} = -\frac{\partial}{\partial t} \int_{\mathcal{V}} f(\mathbf{r}, t) dV \quad (5)$$

where

$$dV = \text{differential volume element in } \mathcal{V}$$

This is the change in m as a result of a decrease in density f within \mathcal{V} .

Assuming that f is a density of some conserved quantity—meaning that this quantity is neither created nor destroyed—the change in m above should exactly be matched by the flux of m out of the volume \mathcal{V} . Mathematically,

$$\frac{dm}{dt} = \oint_{\partial\mathcal{V}} f(\mathbf{r}, t) \mathbf{s}(\mathbf{r}, t) \cdot d\mathbf{n} \quad (6)$$

where

$\partial\mathcal{V}$ = surface enclosing \mathcal{V}

$d\mathbf{n}$ = differential normal surface element on $\partial\mathcal{V}$

$\mathbf{s}(\mathbf{r}, t)$ = velocity field in spatial description

Equating (5) and (6) yields the conservation equation which states that the rate of m (the volume integral of density f) leaving an arbitrary region \mathcal{V} must be canceled by the flux of m across the surface $\partial\mathcal{V}$ enclosing that region

$$\frac{\partial}{\partial t} \int_{\mathcal{V}} f dV + \oint_{\partial\mathcal{V}} f \mathbf{s} \cdot d\mathbf{n} = 0 \quad (7)$$

This is the conservation of mass equation (in integral form) that every density image is defined to obey.

Application of the divergence theorem to the flux integral yields

$$\int_{\mathcal{V}} \left(\frac{\partial}{\partial t} f + \nabla \cdot (f \mathbf{s}) \right) dV = 0 \quad (8)$$

This must hold for every arbitrary region \mathcal{V} . Hence, the integrand itself must be identical to zero.

$$f_t + \nabla \cdot (f \mathbf{s}) = 0 \quad (9)$$

This is the conservation of mass equation in differential form. In continuum theory, (9) is referred to as the *equation of continuity*. It can be shown that (9) holds even for blurred images [15] by defining a blurred version of the velocity field \mathbf{s} .

Equation (9) may be used as a constraint on the velocity field $\mathbf{s}(\mathbf{r}, t)$. For density images of a compressible medium, the continuity equation (9) may be used as a constraint on velocity field rather than constraints to be discussed in Sections 2.3 and 2.4 to follow. For instance,

in [14] and [16], (9) was used as a constraint and was solved by assuming the velocity field \mathbf{s} to be irrotational or curl-free. Unfortunately, real velocity fields are rarely curl-free and for this reason, incompressible fluid that is curl-free is sometimes referred to as the *dry water* [17].

2.3 The Incompressibility Constraint

The density f may be expressed in either material or spatial descriptions.

$$\begin{aligned} f^L(\mathbf{R}, t) & \quad \text{in Lagrangian or material description} \\ f^E(\mathbf{r}, t) & \quad \text{in Eulerian or spatial description} \end{aligned}$$

Recall that in material description, the initial position \mathbf{R} is the independent variable whereas in spatial description, \mathbf{r} is independent. In view of (3),

$$f^L(\mathbf{R}, t) = f^E(\mathbf{r}, t) \big|_{\mathbf{r}=\mathbf{r}(\mathbf{R}, t)}$$

Then, by considering the initial position \mathbf{R} as the fixed variable we take the partial derivative of both sides with respect to t . Using $\mathbf{r} = (x, y, z)$,

$$\begin{aligned} \frac{\partial}{\partial t} f^L(\mathbf{R}, t) &= \frac{\partial x}{\partial t} \frac{\partial f^E}{\partial x} \bigg|_{\mathbf{r}=\mathbf{r}(\mathbf{R}, t)} + \frac{\partial y}{\partial t} \frac{\partial f^E}{\partial y} \bigg|_{\mathbf{r}=\mathbf{r}(\mathbf{R}, t)} \\ &+ \frac{\partial z}{\partial t} \frac{\partial f^E}{\partial z} \bigg|_{\mathbf{r}=\mathbf{r}(\mathbf{R}, t)} + \frac{\partial f^E}{\partial t} \bigg|_{\mathbf{r}=\mathbf{r}(\mathbf{R}, t)} \end{aligned} \quad (10)$$

The partials $\partial x/\partial t$, $\partial y/\partial t$ and $\partial z/\partial t$ evaluated at $\mathbf{r} = \mathbf{r}(\mathbf{R}, t)$ simply represent three components of the velocity in material description $\mathbf{S}(\mathbf{R}, t)$. Using (3) and (4) we may express (10) in spatial description as

$$\begin{aligned} \frac{\partial}{\partial t} f^L(\mathbf{R}, t) \big|_{\mathbf{R}=\mathbf{R}(\mathbf{r}, t)} & \\ &= \frac{\partial f}{\partial t} + u(\mathbf{r}, t) \frac{\partial f}{\partial x} + v(\mathbf{r}, t) \frac{\partial f}{\partial y} + w(\mathbf{r}, t) \frac{\partial f}{\partial z} \end{aligned} \quad (11)$$

where $\mathbf{s}(\mathbf{r}, t) = (u, v, w)$. The superscript E on f have been dropped. From this point on, by f we mean the spatial description of the density— $f^E(\mathbf{r}, t)$. The left hand side of (11) is the rate of change in the density of the particle initially at \mathbf{R} expressed in terms of the spatial

variable \mathbf{r} . It is precisely the rate of change of f as seen by an observer moving with the particle initially at \mathbf{R} .

The *convected* or *mobile derivative* is defined as the derivative with respect to time, moving with the particle, as

$$\frac{D}{Dt} = \frac{\partial}{\partial t} + \mathbf{s} \cdot \nabla \quad (12)$$

Then, we may write (11) as

$$\frac{D}{Dt} f = \frac{\partial}{\partial t} f + \mathbf{s} \cdot \nabla f \quad (13)$$

For an incompressible medium, the density f does not change in time if the observation is carried out while moving along with the particle. Therefore $D/Dt f = 0$ if f represents an incompressible medium. This yields the *incompressibility constraint*.

$$f_t + \nabla f \cdot \mathbf{s} = 0 \quad (14)$$

This is equivalent to the *brightness constraint* of optical flow extended to 3-D.

Examples abound where the flow is incompressible and thus satisfying (14). For instance, in CT images, the density (and hence CT numbers) of the constituents of the core are invariant during the loading process. Consequently, CT images of the core should obey the incompressibility constraint (14).

2.4 The Divergence-Free Constraint

Thus far, the constraints on the velocity field of a moving body represented by a density image were shown to be the continuity constraint (9) and the incompressibility constraint (14). These two constraints may be imposed directly; however, in practice we have found that it was easier to impose the incompressibility constraint and a linear combination of the two constraints.

Equating (9) and (14) yields,

$$\nabla \cdot (f\mathbf{s}) = \nabla f \cdot \mathbf{s}$$

The left hand side can be expanded as $\nabla \cdot (f\mathbf{s}) = f \nabla \cdot \mathbf{s} + \nabla f \cdot \mathbf{s}$, resulting in

$$f \nabla \cdot \mathbf{s} = 0 \quad (15)$$

In continuum theory, (15) is referred to as the *continuity equation for incompressible media*. Equation (15) states that for an incompressible medium the divergence of the velocity field must be zero for regions where f is non-zero. That is,

$$\nabla \cdot \mathbf{s} = 0 \quad (16)$$

This is the *divergence-free* constraint which incompressible density images must obey. For regions where $f = 0$, where it is void of ‘particles’, we also assume the velocity field to be divergence-free for mathematical simplicity.

We end this section by noting that when imposing the divergence-free constraint (16), the incompressibility constraint (14) should also be imposed, since the latter was used in deriving (16).

3 Problem Description

3.1 Formulation

Computation of the velocity field using the incompressibility and the divergence-free constraints is an ill-posed problem, i.e., the solution is not necessarily unique and may be sensitive to small changes in the data.

The cost functional $e_S(\mathbf{s})$ is defined as

$$e_S(\mathbf{s}) = \int_{\Omega} (u_x^2 + u_y^2 + u_z^2 + v_x^2 + v_y^2 + v_z^2 + w_x^2 + w_y^2 + w_z^2) d\Omega \quad (17)$$

where

$$\begin{aligned} \Omega &= \{(x, y, z) \in \mathfrak{R}^3 : 0 \leq x \leq T_x, 0 \leq y \leq T_y, 0 \leq z \leq T_z\} \\ d\Omega &= dx dy dz \\ \mathfrak{R} &= \text{the real line} \end{aligned}$$

and (T_x, T_y, T_z) is the spatial extent of the imaging volume.

Combining the cost e_S (17) and the two constraints, the optimization problem becomes

$$\begin{aligned} &\text{minimize} && e_S(\mathbf{s}) \\ &\text{subject to} && f_x u + f_y v + f_z w + f_t = 0 \quad \text{and} \quad u_x + v_y + w_z = 0 \end{aligned} \quad (18)$$

Rather than solving the above optimization problem directly, we consider the equivalent problem.

$$\begin{aligned} & \text{minimize} && e_S(\mathbf{s}) \\ & \text{subject to} && e_I(\mathbf{s}) = 0 \quad \text{and} \quad e_D(\mathbf{s}) = 0 \end{aligned} \quad (19)$$

where

$$\begin{aligned} e_I(\mathbf{s}) &= \int_{\Omega} (f_x u + f_y v + f_z w + f_t)^2 d\Omega \\ e_D(\mathbf{s}) &= \int_{\Omega} (u_x + v_y + w_z)^2 d\Omega \end{aligned}$$

Since (19) is a convex minimization problem over convex constraints, one could apply the method of Lagrange multipliers to find an optimal solution. However, due to the complexity of the problem and the difficulty in finding the Lagrange multipliers, we confine our attention to finding an approximate solution to (19) by unconstrained minimization of the penalty function

$$e(\mathbf{s}) = e_S(\mathbf{s}) + \gamma_1 e_I(\mathbf{s}) + \gamma_2 e_D(\mathbf{s}) \quad (20)$$

where γ_1 and γ_2 are a pair of real positive constants. We note that an approximate choice of γ_1 and γ_2 is an important theoretical problem; however, we have found in practice that acceptable solutions may be obtained by minimizing $e(\mathbf{s})$ over a fairly wide range of values for γ_1 and γ_2 . By way of justification of this approximate solution, we note that in practice, the data contains noise, and the use of hard constraints as in (18) may result in poor solutions due to the incorporation of the noise into the computed velocity fields. In contrast, the solution obtained by minimizing (20) does not require that the constraints be exactly met, and consequently may be more robust to noise.

In the optical flow formulation of Horn and Schunck [4], a global constraint—a 2-D version of e_S above—was introduced so that a solution may be obtained. The penalty method presented in this section is identical to their approach. In fact, if $\gamma_2 = 0$, our method yields a straight-forward extension of optical flow solution [4] to 3-D.

3.2 Solution by Minimization of the Penalty $e(\mathbf{s})$

In this section, we present a solution minimizing the penalty functional $e(\mathbf{s})$.

$$\begin{aligned} e(\mathbf{s}) &= \int_{\Omega} \{ (u_x^2 + u_y^2 + u_z^2 + v_x^2 + v_y^2 + v_z^2 + w_x^2 + w_y^2 + w_z^2) \\ &\quad + \gamma_1 (f_x u + f_y v + f_z w + f_t)^2 + \gamma_2 (u_x + v_y + w_z)^2 \} d\Omega \end{aligned} \quad (21)$$

where $\mathbf{s} = (u, v, w)$ and γ_1 and γ_2 are real positive constants.

Let F be the integrand of (21). Then, from the calculus of variations the solution \mathbf{s}_0 must satisfy the following set of Euler-Lagrange equations with either the Dirichlet or the Neumann boundary conditions.

$$\begin{aligned} 0 &= F_u - \frac{\partial}{\partial x} F_{u_x} - \frac{\partial}{\partial y} F_{u_y} - \frac{\partial}{\partial z} F_{u_z} \\ 0 &= F_v - \frac{\partial}{\partial x} F_{v_x} - \frac{\partial}{\partial y} F_{v_y} - \frac{\partial}{\partial z} F_{v_z} \\ 0 &= F_w - \frac{\partial}{\partial x} F_{w_x} - \frac{\partial}{\partial y} F_{w_y} - \frac{\partial}{\partial z} F_{w_z} \end{aligned} \quad (22)$$

The substitution of the partials into the Euler-Lagrange equation (22) results in the following set of partial differential equations (PDEs).

$$\begin{aligned} \nabla^2 u &= \gamma_1 f_x(f_x u + f_y v + f_z w + f_t) - \gamma_2 (u_{xx} + v_{xy} + w_{xz}) \\ \nabla^2 v &= \gamma_1 f_y(f_x u + f_y v + f_z w + f_t) - \gamma_2 (u_{xy} + v_{yy} + w_{yz}) \\ \nabla^2 w &= \gamma_1 f_z(f_x u + f_y v + f_z w + f_t) - \gamma_2 (u_{xz} + v_{yz} + w_{zz}) \end{aligned} \quad (23)$$

where ∇^2 is the Laplacian operator. The solution satisfies equation (23) on the interior of Ω . On the boundary $\partial\Omega$, we impose either the Dirichlet or Neumann boundary conditions (see Appendix A).

If we let $\gamma_2 = 0$, in (23) then the problem is identical to the optical flow problem [4] extended to 3-D; and the solution satisfies the PDEs.

$$\begin{aligned} \nabla^2 u &= \gamma_1 f_x(f_x u + f_y v + f_z w + f_t) \\ \nabla^2 v &= \gamma_1 f_y(f_x u + f_y v + f_z w + f_t) \\ \nabla^2 w &= \gamma_1 f_z(f_x u + f_y v + f_z w + f_t) \end{aligned} \quad (24)$$

As in [4] the Laplacian may be discretized as $\nabla^2 g = \kappa(\bar{g} - g)$ where κ is a constant depending on the differential mask and \bar{g} is the local average of g . Algebraic manipulation and a symbolic inversion of the 3 by 3 matrix result in a Jacobi type iterative algorithm.

$$u^{(n+1)} = \bar{u}^{(n)} - f_x \frac{\bar{u}^{(n)} f_x + \bar{v}^{(n)} f_y + \bar{w}^{(n)} f_z + f_t}{(\kappa/\gamma_1) + f_x^2 + f_y^2 + f_z^2}$$

$$\begin{aligned}
v^{(n+1)} &= \bar{v}^{(n)} - f_y \frac{\bar{u}^{(n)} f_x + \bar{v}^{(n)} f_y + \bar{w}^{(n)} f_z + f_t}{(\kappa/\gamma_1) + f_x^2 + f_y^2 + f_z^2} \\
w^{(n+1)} &= \bar{w}^{(n)} - f_z \frac{\bar{u}^{(n)} f_x + \bar{v}^{(n)} f_y + \bar{w}^{(n)} f_z + f_t}{(\kappa/\gamma_1) + f_x^2 + f_y^2 + f_z^2}
\end{aligned} \tag{25}$$

If the most recent updated values are used in the iteration above, we obtain a Gauss-Seidel iteration. The successive over-relaxation (SOR) method [18] may also be used.

In Jacobi type iterations, convergence is guaranteed if the *row-sum criterion* [18] is met. Unfortunately, the row-sum criterion cannot be checked since the row elements depend on the image f . However, we have implemented (25) in 3-D and obtained convergence for a large class of images. It is more difficult to obtain a Jacobi type iterative formula for the case $\gamma_2 \neq 0$ as this involves a symbolic inversion of a more complex 3 by 3 matrix. Although this symbolic inversion can be done, we chose to use the conjugate gradient algorithm where convergence is guaranteed [19].

3.3 Discretization of the PDE

To compute a solution for the PDEs in (23), the equations must be discretized. Assuming uniform sampling, let the spatial sample grid spacings be Δ_x, Δ_y , and Δ_z for the x, y and z -axis respectively, and let

$$f_{ijk} = f(x, y, z) |_{(x,y,z)=(i \Delta_x, j \Delta_y, k \Delta_z)}, \quad (x, y, z) \in \Omega \tag{26}$$

The partial derivatives (f_x, f_y, f_z, f_t) and the velocity components (u, v, w) are similarly discretized.

Using lexicographical ordering [20], the image samples f_{ijk} can be vector-stacked as $\mathbf{f} = [f_{0,0,0}, \dots, f_{N_x-1, N_y-1, N_z-1}]^T$ where (N_x, N_y, N_z) denotes the discrete spatial extent of the imaging volume. The vectors, $\mathbf{f}_x, \mathbf{f}_y, \mathbf{f}_z, \mathbf{f}_t, \mathbf{u}, \mathbf{v}$ and \mathbf{w} are similarly constructed. The solution vector \mathbf{x} is then defined as

$$\mathbf{x} = \begin{bmatrix} \mathbf{u} \\ \mathbf{v} \\ \mathbf{w} \end{bmatrix} \tag{27}$$

To express the PDEs of (23) in the discrete domain, the matrices below are defined.

$$\mathbf{H}_D = [\mathbf{D}_x | \mathbf{D}_y | \mathbf{D}_z]$$

$$\begin{aligned}
\mathbf{H}_I &= [\text{diag}(\mathbf{f}_x) \mid \text{diag}(\mathbf{f}_y) \mid \text{diag}(\mathbf{f}_z)] \\
\mathbf{Q} &= \begin{bmatrix} \mathbf{D}_x^2 + \mathbf{D}_y^2 + \mathbf{D}_z^2 & \mathbf{0} & \mathbf{0} \\ \mathbf{0} & \mathbf{D}_x^2 + \mathbf{D}_y^2 + \mathbf{D}_z^2 & \mathbf{0} \\ \mathbf{0} & \mathbf{0} & \mathbf{D}_x^2 + \mathbf{D}_y^2 + \mathbf{D}_z^2 \end{bmatrix} \\
\text{diag}(\mathbf{f}_x) &= N \times N \text{ diagonal matrix with elements of } \mathbf{f}_x \text{ in the diagonal}
\end{aligned} \tag{28}$$

where \mathbf{D}_x , \mathbf{D}_y and \mathbf{D}_z are matrix representations of partial differential operators with respect to x , y and z respectively, and $N = N_x N_y N_z$. With this discretization, (23) has the following discrete form.

$$\mathbf{A}\mathbf{x} = \mathbf{b}, \quad \text{where} \quad \begin{cases} \mathbf{A} = \mathbf{Q} - \gamma_1 \mathbf{H}_I^T \mathbf{H}_I + \gamma_2 \mathbf{H}_D^T \mathbf{H}_D \\ \mathbf{b} = \gamma_1 \mathbf{H}_I^T \mathbf{f}_t \end{cases} \tag{29}$$

Boundary Conditions

Equation (29), is not completely defined without a boundary condition. For instance, assuming a central difference scheme, partial differentiation along the z -axis (i.e. \mathbf{D}_z) is not defined at boundaries $z = 0$ and $z = T_z$. A Dirichlet or a Neumann boundary condition (see Appendix A of [1]) can be used to define the elements of \mathbf{A} corresponding to the boundary $\partial\Omega$.

If we know the value of \mathbf{s} on the boundary $\partial\Omega$, then the natural choice is the Dirichlet boundary condition. For instance, on the bounding planes of the 3-D image, the motion may be known to be zero a priori. In this case, the value of \mathbf{x} , the discrete version of \mathbf{s} , is known on $\partial\Omega$. Hence, the matrix equation (29) can be reduced to a smaller dimension discarding the elements corresponding to the boundary $\partial\Omega$. The algorithm only computes elements of \mathbf{x} corresponding to the interior of Ω . Therefore, the differential operators of (29)—assuming the usual central difference derivative, five point Laplacian, etc—are defined everywhere in the interior of Ω and (29) may be solved.

If we have no knowledge of the value of \mathbf{s} on the boundary $\partial\Omega$, we insist that the Neumann boundary condition in Appendix A of [1] be satisfied. The Neumann boundary condition for our problem becomes

$$\left. \begin{aligned} u_x + \gamma_2(u_x + v_y + w_z) &= 0 \\ v_x &= 0 \\ w_x &= 0 \end{aligned} \right\} \quad \text{at } x = 0, \text{ and } x = T_x \tag{30}$$

$$\left. \begin{aligned} u_y &= 0 \\ v_y + \gamma_2(u_x + v_y + w_z) &= 0 \\ w_y &= 0 \end{aligned} \right\} \text{ at } y = 0, \text{ and } y = T_y \quad (31)$$

$$\left. \begin{aligned} u_z &= 0 \\ v_z &= 0 \\ w_z + \gamma_2(u_x + v_y + w_z) &= 0 \end{aligned} \right\} \text{ at } z = 0, \text{ and } z = T_z \quad (32)$$

The Neumann boundary condition is not well-defined at edges or vertices of Ω , as the normal vector \mathbf{n} is not continuous there. At an edge we may insist that boundary conditions corresponding to the two intersecting boundary planes both be satisfied; and at a corner, we impose three boundary conditions for the three intersecting boundary planes.

4 Results

In this section, results obtained by the conjugate gradient implementation of the algorithm of the previous section are presented. The 2-D version of the incompressibility constraint—the brightness constraint of optical flow—has been studied extensively; therefore, results obtained (1) with the incompressibility constraint only; and (2) with both incompressibility and divergence-free constraints are compared. It is demonstrated that for density images of moving incompressible objects, using the divergence-free constraint with the incompressibility constraint provides solutions consistent with our intuition of the motion of deforming objects. In all cases presented the Dirichlet boundary condition was used since at spatial boundaries of the images, the motion was known to be zero. For the CT images of the asphalt core this is true, since the imaging volume entirely encloses the core.

4.1 Simulated Images

All simulated images presented in this section were constructed so that the conservation of mass is obeyed. Regions of images were allowed to deform but they were not allowed to change in the area that they occupy in both time frames. Hence, these simulated images clearly satisfies the conservation of mass (7). The incompressibility constraint was imposed on the motion by maintaining a constant gray level for each fixed point of the image as the objects deformed. Thus, the velocity field generated by the simulated images of Figures A. 1 and A. 5 were constructed to satisfy the incompressibility and the divergence-free constraints.

2-D images

For illustration purposes, 2-D examples are presented first. Experiment 1 of Figure A. 1 shows a 64×64 image sequence of a translating circle. The boundary of the outer circle (of radius 25 pixels) is fixed whereas the inner circle (of radius 13 pixels) translates one pixel down. A physical example of this type of motion is a situation in which the inner region is solid and the outer doughnut is fluid. The images represent the densities of these regions. As the inner circle translates, the outer region (the outer boundary is fixed) experiences motion such that along the left and right regions of the doughnut, upward motion should prevail to evacuate (bottom) and replenish (top) the regions affected by the inner region's motion.

The incompressibility constraint alone does not give results that show such motion. Figure A. 2 (a) shows the result obtained using only the incompressibility constraint. Here, a general downward motion is shown which does not agree with preceding arguments. When using both constraints, the motion within the doughnut region is seen to accommodate the motion of the inner circle as described above. This is clearly indicated in Figure A. 2 (b).

Experiment 2 of Figure A. 1 shows a 64×64 image sequence of a diagonally translating circle. The boundary of the outer circle is fixed as for the first experiment, and the inner circle translates 1 pixel diagonally. Both circles are of the same radius as in the first experiment. Figure A. 3 depicts similar but different results as in experiment 1. We conjecture that the difference is probably due to the quantization of the image f , as well as the derivative operators.

Experiment 3 of Figure A. 1 shows a 64×64 image sequence of a deforming ellipse. The outer ellipse (a circle of radius 25) is fixed in both frames and the inner ellipse deforms from a major and minor axis of (13, 10) to (15, 130/15). These numbers were chosen to guarantee the conservation of mass—i.e. the equation of continuity (9). Again, the utility of the divergence-free constraint for density images is clearly illustrated in Figure A. 4.

These experiments in 2-D clearly indicate the advantage of using the divergence-free constraint for density images.

3-D images

Experiment 4 of Figure A. 5 shows a $16 \times 16 \times 8$ image sequence of a translating ellipsoid. The outer ellipsoid is fixed in both frames and the inner ellipsoid translates down one voxel. As

for the experiments in 2-D, the algorithm was performed with and without the divergence-free constraint. Figure A. 6 shows the two 3-D vector fields plotted as a function of 3-D space, projected onto a plane. Figure A. 6 (a)—without the divergence-free constraint—does indicate a general downward motion. However, the motion deep within the inner ellipsoid is significantly smaller than it should be. Figure A. 6 (b) does not have this undesirable effect due to the divergence-free constraint.

4.2 Applications to CT asphalt core images

The CT images were collected on a Phillips TX60 X-ray CT scanner. A sequence of 2-D images spaced 2mm apart were collected for the original core and again after the application of each loading. The ASTM diametal loading test was used allowing deformations upto 0.1in. A detailed analysis of this data is the subject of a future paper. Our purpose here is simply to demonstrate the ability of the method described above to estimate the displacement or velocity field. In order to compute this field one must first accurately register each of the 3-D data sets to a common computer coordinate frame. The reason for this is that it is very difficult to exactly reposition the core within the scanner after each loading. The results shown here are based on the computation of flow for a registered pair of 2-D slices (before and after loading). These slices were selected from the 3-D image sets and carefully registered by trial and error. The 2-D version of the velocity computation algorithm was then applied. The resulting estimated flow field, overlayed on each of the images is shown in Figure A. 7. The arrows in the figure show the location of the loading bars relative to the core.

As one would expect, the predominant motion towards the center in the direction of the load and away from the center in the orthogonal direction. However, one can also see local variation in this motion due to early crack formation in the location of the larger aggregate particles.

Clearly a more detailed analysis of the 3-D data is required before conclusions may be drawn concerning the nature of the deformation under diametal loading conditions. However, these results clearly indicate the ability of the algorithm described in this report to produce reasonable estimates of the deformation of the asphalt/aggregate core due to loading.

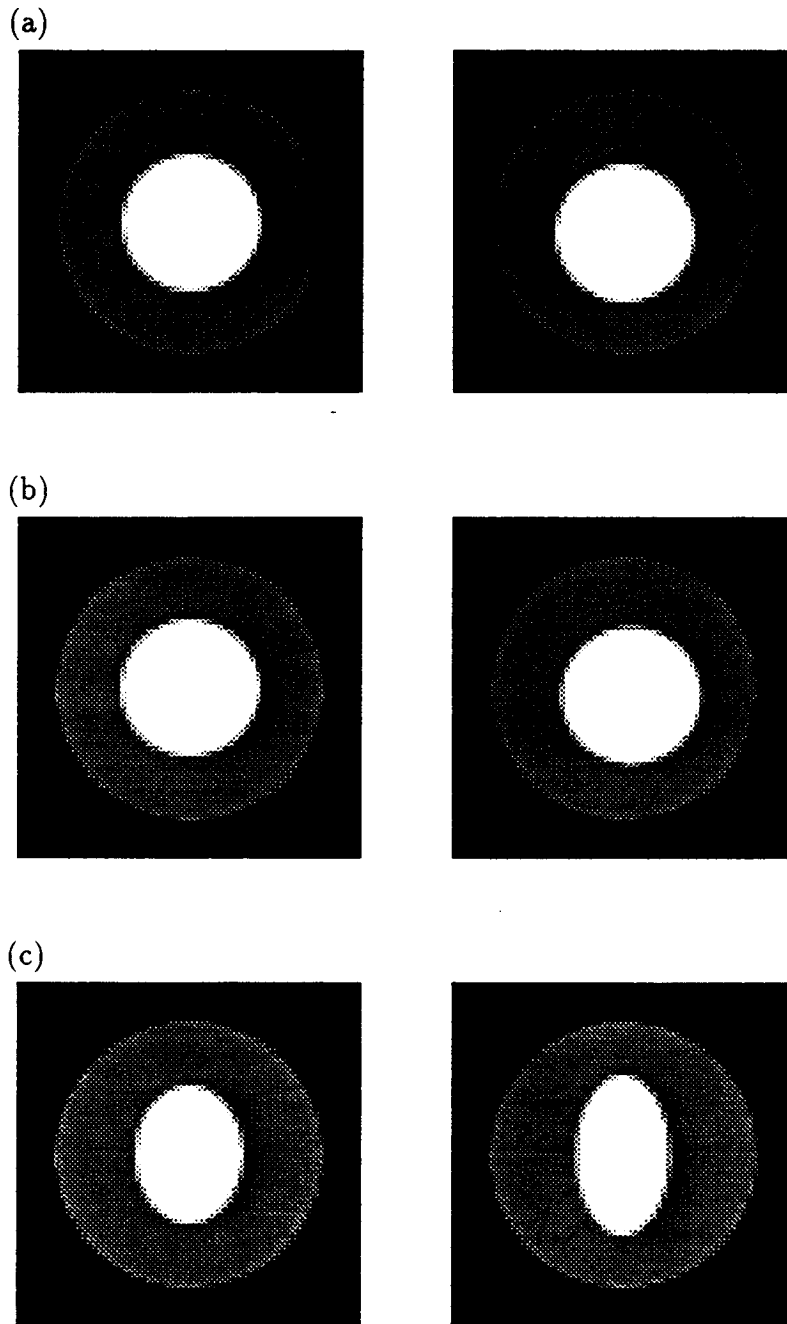
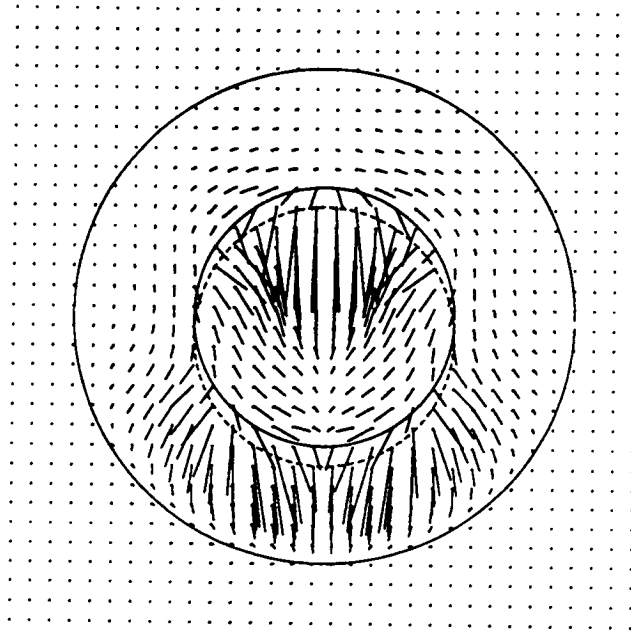


Figure A.1 Simulated images for experiments 1,2 and 3.

- (a) Experiment 1, synthetic images of a vertically translating circle.
- (b) Experiment 2, synthetic images of a diagonally translating circle.
- (c) Experiment 3, synthetic images of a deforming ellipse.

(a)



(b)

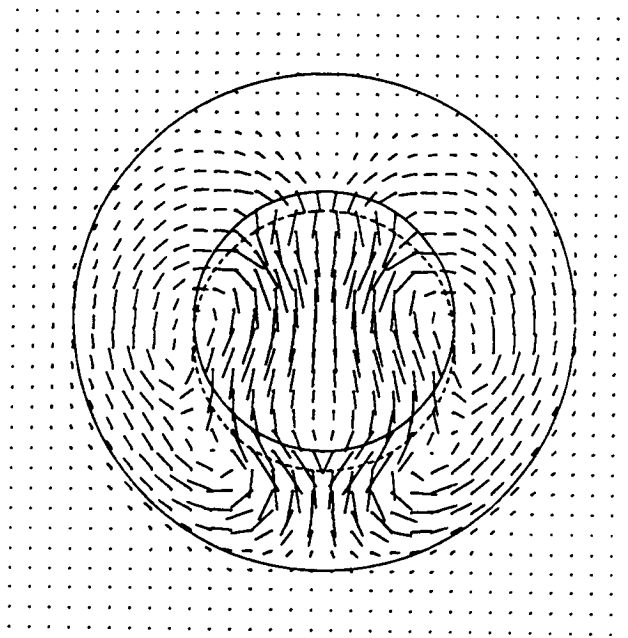
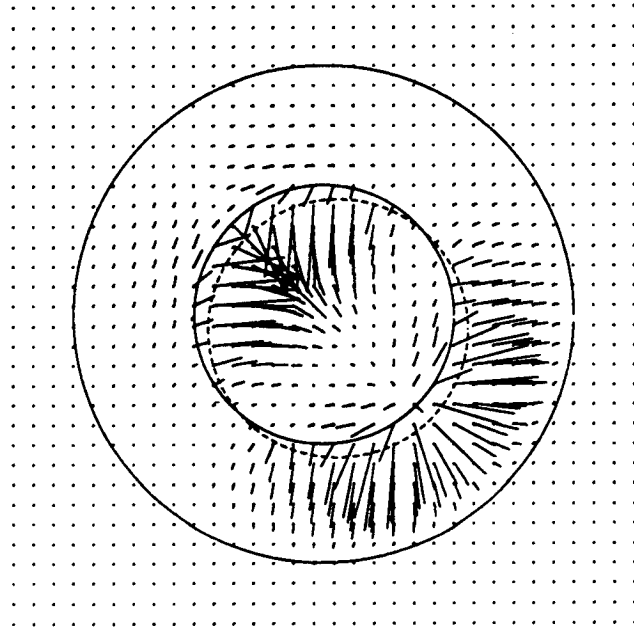


Figure A.2 Calculated flow field from experiment 1 with the boundary outlines; the dotted circle represents the second time frame. (a) Results derived using the incompressibility constraint only; (b) using the incompressibility and the divergence-free constraints.

(a)



(b)

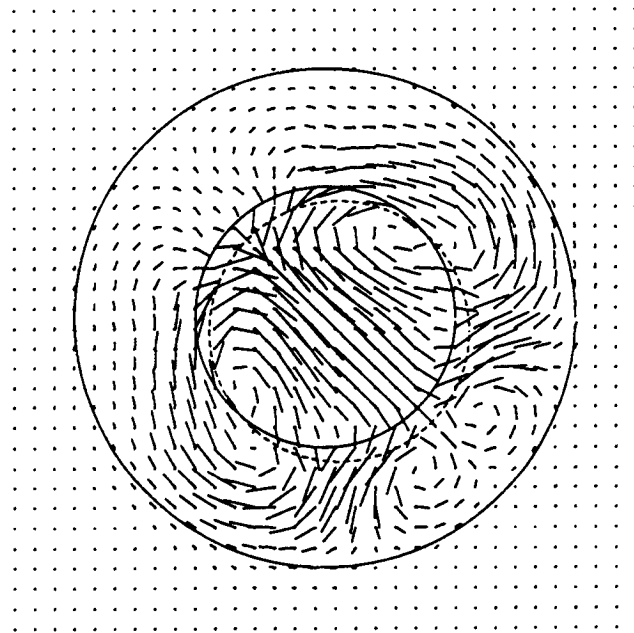
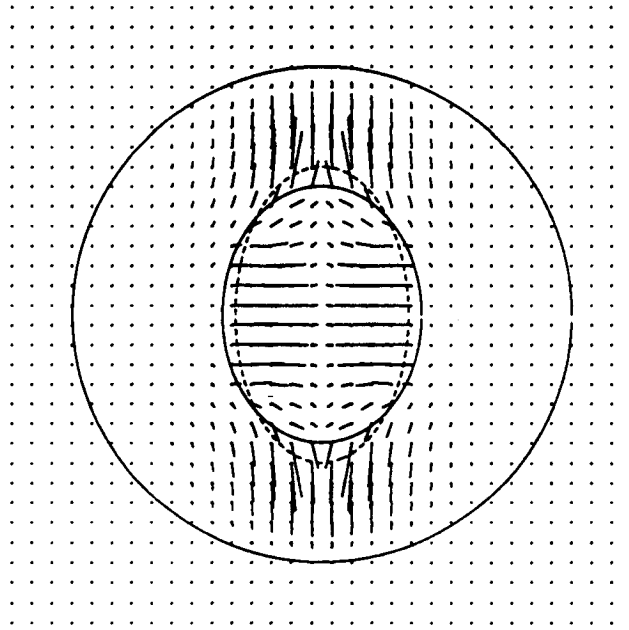


Figure A.3 Calculated flow field from experiment 2 with the boundary outlined. See caption of figure A.2

(a)



(b)

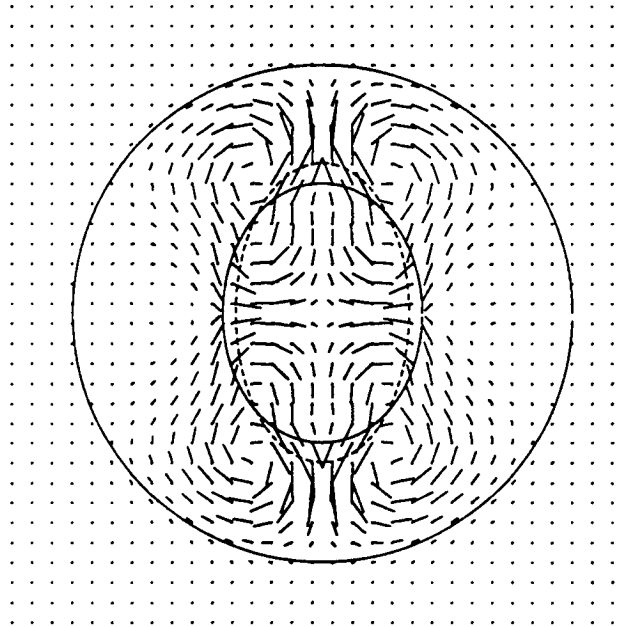


Figure A.4 Calculated flow field from experiment 3 with the boundary outlined. See caption of figure A.2

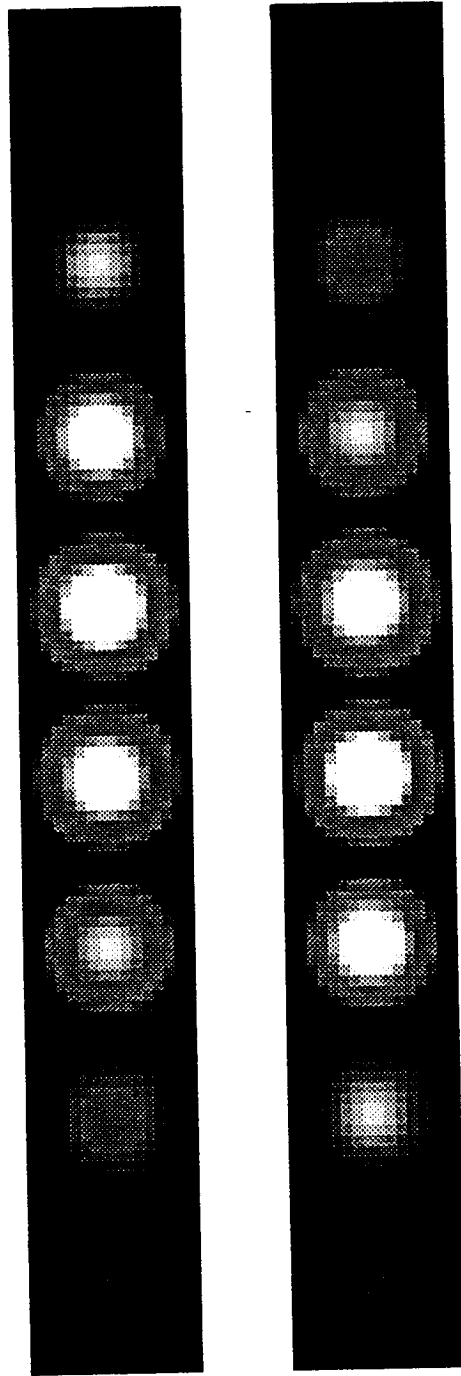


Figure A.5 Simulated images for experiments 4. Vertically translating ellipsoid, time frames 1 and 2.

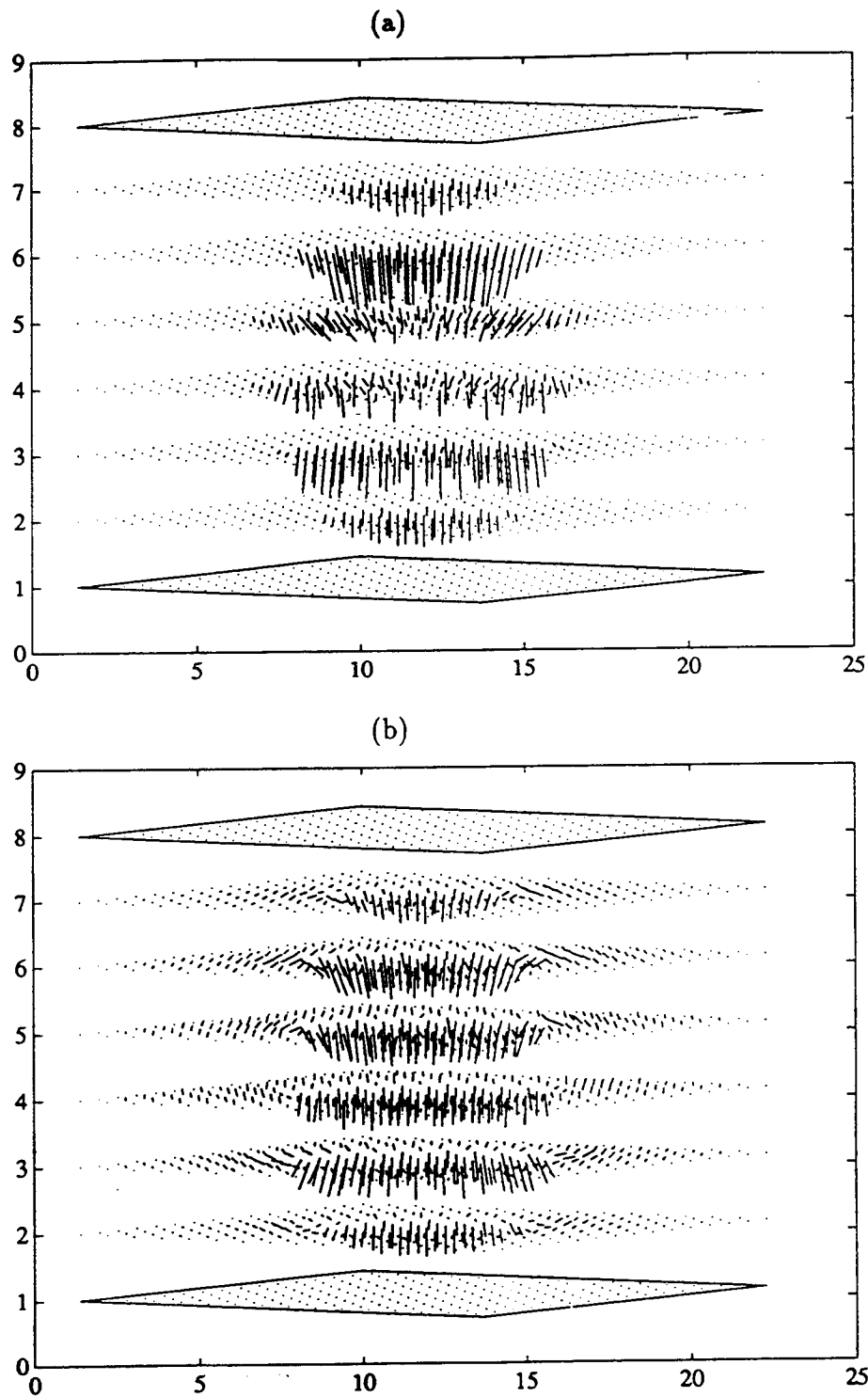


Figure A.6 Calculated flow field from experiment 4. The 3-D vector field is projected into the plane shown. a) Results derived using the incompressibility constraint only; (b) using the incompressibility and the divergence-free constraints.

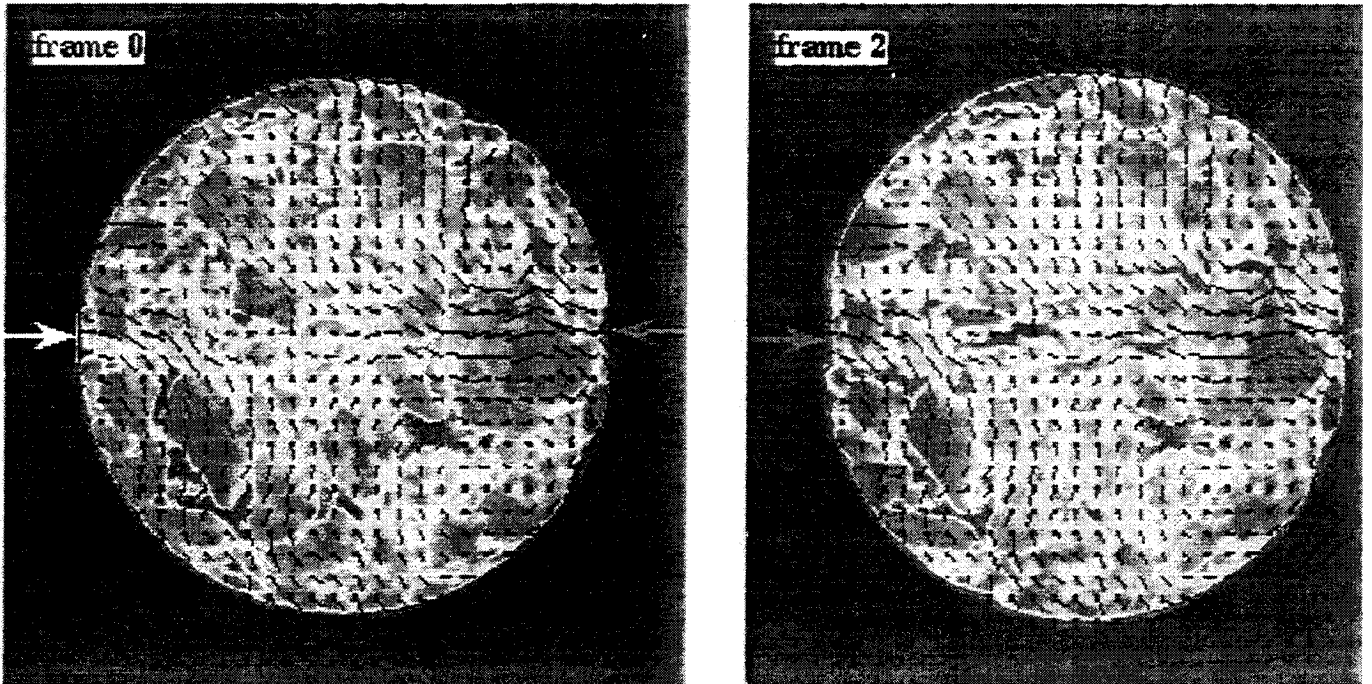


Figure A.7 Demonstration of image flow calculations. Two registered images of the 5B1WOFD core before and after two stages of loading. The vectors overlaid on the images show the magnitude and the direction of the velocity of each pixel in the image.

Appendix B

ASPlab USER'S MANUAL

Zhenyu Zhou, Richard Leahy, Costas Synolakis

1. Abstract‡

This section describes software developed specifically for analyzing CT image data of asphalt cores. It is based on the commercial image processing software package IPLab. At this stage this software is only available for the Macintosh family of computers. Several additional utilities have been generated for the specific requirements of asphalt core tomography including beam hardening correction, calibration, mass-fraction determination, and edge-detection analysis and other image enhancement functions. The software package can

‡ This software works with any Macintosh II having a color monitor; four megabytes of memory are recommended.

also take advantage of various existing utilities of IPLab such as enhancement, histogram equalization, Fourier transform, medium filtering, animation, enhanced contrast, and point function.

This manual describes specific features of the software used in the ACT protocol; the IPLab describes in depth other features of IPLab. (IPLab is trademark of the Signal Analytics Corporation, see page B14.)

2. Preparation of the data and data transfer.

The raw data which is generated from the CT computer are sequences of CT numbers; the files are not directly readable by any image processing software, except with the proprietary software which is supplied with the CT. However, all the scan data can be transferred on magnetic tape; most CTs have mag-tape drives for archiving of data. The procedure we will describe and the software we developed specifically works for the interface between Phillips or GE scanners and SUN computers.

Using common tools on the SUN, the magnetic tape is mounted and the data is read by running a utility call TCP; this utility translates the CT raw image data into binary format; each image consists of a two-dimensional array of 256×256 two-byte integers and each array element corresponds to one pixel in the image. (This is the image referred to in the image processing literature as the "short" integer image. We would like to emphasize that the software automatically multiplies the CT number by a factor of 4, due to a binary shift to the left. This procedure has to be repeated for each image; a batch-file can be written to translate all the CT raw files into these short-integer files.

The files are then ready for image processing on the SUN or for transfer to the Macintosh. We recommend use of FTP, a widely available and used utility for file transfer. Also, to this date (10/26/92) several commercial software packages have been announced for the transfer of data from the CT computers to workstations.

3. Using the ASP lab software.

As a preamble we note that ASP Image Lab works like any other Macintosh application and it uses all the Macintosh user-friendly tools. By taking the mouse image over the ASPLab icon and by double-clicking the mouse the program starts and the user sees the standard Macintosh menu bar. The following discussion assumes that the reader has some basic experience with the Macintosh.

3.1 Starting the program and modifying the data

Go to the menu bar and choose **file** . Choose **open** in the file sub-menu. This operation displays a list of all the image files which are available in the same folder as ASPLab on the Macintosh disk and also six buttons. (This operation is also described in the IPLab manual in the section on MENU reference, pages 76-80). Click **all** then click **set**; another dialog box shows up now. Make the following changes.

1. Change the **pixels per line box** to 256.
2. Change the **number of lines box** to 256.
3. Change the **bytes per pixel box** to 2.
4. Do not change the **extra bytes/line** and the **header length** boxes. (This means DON'T, DON'T.)
5. Click **OK** or type **return**.

Now you are back in the **open** menu; go to the Macintosh disk directory where the CT image files are residing; the box should show a list of all the available image files. Double click on the image file name to be displayed or just highlight the name. Then click on the **open** button. If you have performed all the above functions correctly, you will see the image displayed on the screen as it had originally appeared on the CT computer; however, the contrast on the Macintosh screen is superior. An example of the displayed image is shown in figure B.1.

The next step is to modify the raw data. There are two methods.

1. Go to the **custom** menu and use the sub-menu **modify data**. This action does performs two operation. Each pixel value is automatically divided by four. Then the image of any background artifacts (such as the phantom of the gantry supporting the core)

are removed; this is quite important because these artifacts affect the image processing results. For example, using this operation, figure B.1 automatically becomes figure B.2. The gantry image and other irrelevant background artifacts are removed by setting a threshold value above which everything is displayed. Occasionally, the default threshold we have established (350) may not be adequate for a specific image. The threshold can be easily modified. Go to the **show variable** command in the **view** menu. This operation opens a window referred to as *the vector window*. This window stays open. Go to the **edit** menu and use **set** then highlight the number 254 variable and then use **set** to enter the value 1; highlight the number 255 variable and then use **set** to assign any threshold value you deem appropriate. (The **set** menu is described on page 95 of the IPLab manual.) Then repeat the **modify data** procedure again.

2. Another simple way for modifying the data is using the **point function** item in the **operate** menu. A window appears with 15 functions. One of the choices is the function $(ax+b)/c$; click the button, and then set the following values in the parameter box $a=1$, $b=0$ and $c=4$. The click **OK**. This procedure only divides the data by a factor of 4, but it does not remove the background artifacts. (For more information on the **point function**, refer to page 118 of the IPLab manual.)

3.2 Performing the beam hardening correction to remove artifacts.

The beam hardening correction is one of the most important operations performed by ASPlab. To perform this correction, it is highly recommended to have available the image of a fine-aggregate core of the same diameter and with the same mass fraction as the core under study; both cores should have been imaged by the same CT machine and with the same system parameters. (If not available, the software can perform self-calibration) . A truly uniform core should have a uniform attenuation coefficient. Our software detects the beam hardening effect from the image of the fine core and then it determines a correction function to modify all other test cores.

As discussed in section 3.5 of the main report, the preliminary data suggest that small differences in the mass fraction between the calibration image and the core-under-study do not appear to affect the beam hardening correction function significantly; using a 5% fine aggregate core to correct a 6% test core will produce very similar results as when a

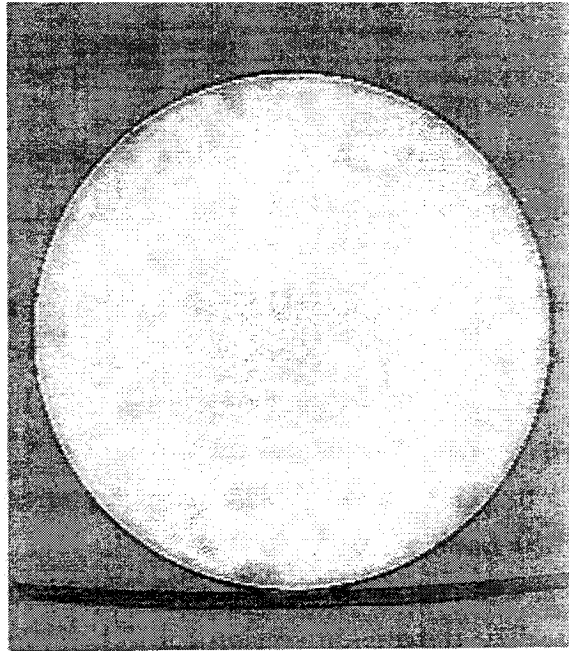


Figure B.1 The image of a fine core, as displayed by the CT computer.

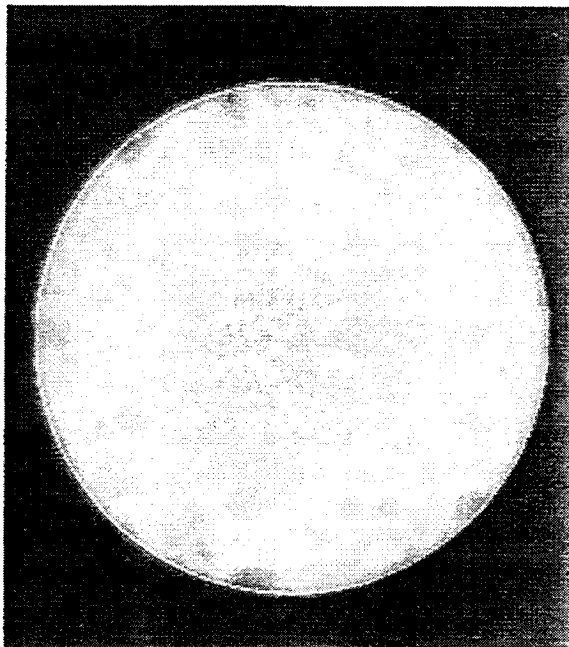


Figure B.2 The image of the core in figure B.1 after the **modify data** operation. The image of the Ct gantry has been removed.

6% fine aggregate core is used for the correction. These differences are not important for morphological studies, but they might be important in the mass-fraction calculations.

Proceed as follows.

1. Go to the **file** menu and choose **open** and select the file name with the image data which is to be used as the calibration standard.

2. **Modify data** as described in the previous section (3.1).

3. Go to the **custom** menu and choose **measure**. This operation determines the calibration function. This function is now stored internally and it is available throughout this particular session of ASPLab.

4. Go to the **file** menu and choose **open** and select the file name with the core images to be corrected. Then **modify data** as in section 3.1. The image of the uncorrected test core is now displayed.

5. Go to the **custom** menu and choose **BH calibrate**. The image of the test core in the display is automatically transformed to the corrected image.

To appreciate this operation consider figure 3 which shows a "uniform" calibration core before calibration and figure 4 which shows the same image after the beam hardening correction. Figure B.5 shows "before" and "after" pairs for a mixed fine-coarse aggregate core. Figure B.7 shows "before" and "after" pairs for a coarse-aggregate core.

The beam hardening correction and its effects can be monitored by looking at the variation of CT numbers across the core. The following procedure is useful in accomplishing this operation. Use the **New ROI** (Region of Interest) command in the **edit** menu and set the **ROI** to any value (see page 100 of the IPLab manual). Remember that it is most convenient to obtain the distribution over one of the diameters. Set the left button to 0, the right button to 255, the top to 128 and the bottom to 129. By assigning these values, you have now selected one line through the core. Then select **analyze** from the menu bar choose the **ToVector** command and click the button **data** within **ROI**. A vector window now appears which displays the distribution of CT numbers along the chosen slice. If you repeat this procedure before and after the beam hardening correction, you can visualize the differences in the images. See, for example, figures B.4 and figure B.6 which correspond to the images of figures B.3 and figure B.5.

Another method for performing the beam hardening correction is to shelf-calibrate the core. This is particularly useful when a calibration image is not available, or when the

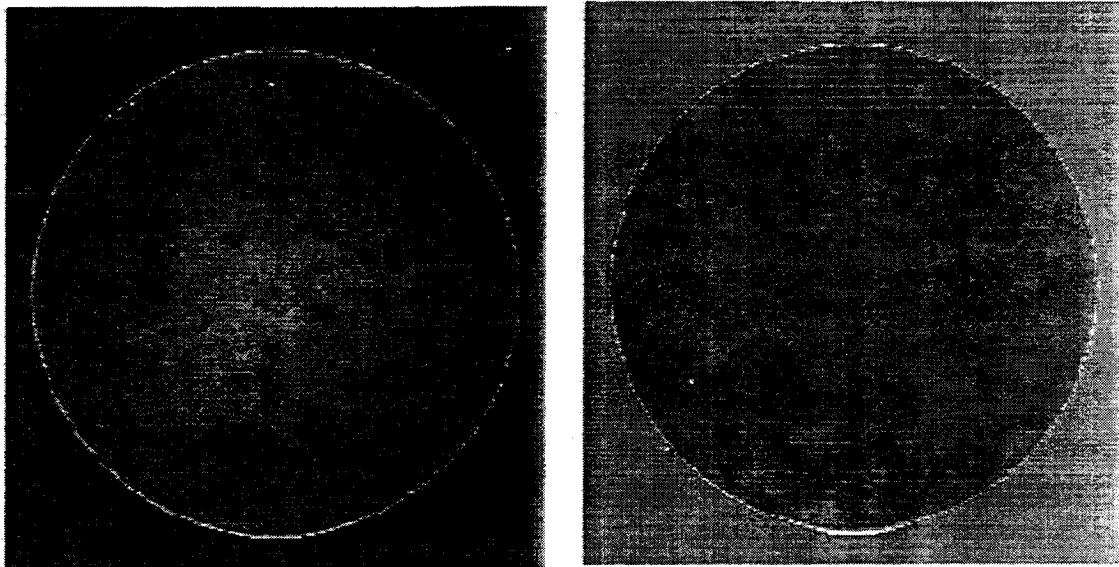


Figure B.3 The image of a fine core before and after the beam hardening calibration

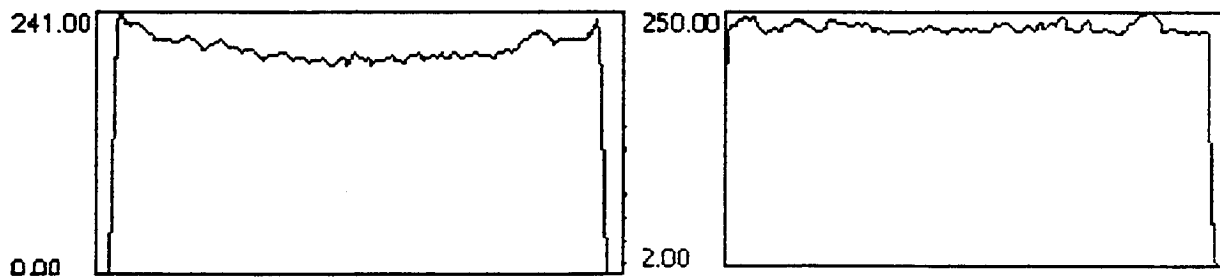


Figure B.4 The variation of the CT number along a diameter of the image in figure B.3 before and after BH calibration. Notice how the calibration produces a more uniform CT variation along the diameter.

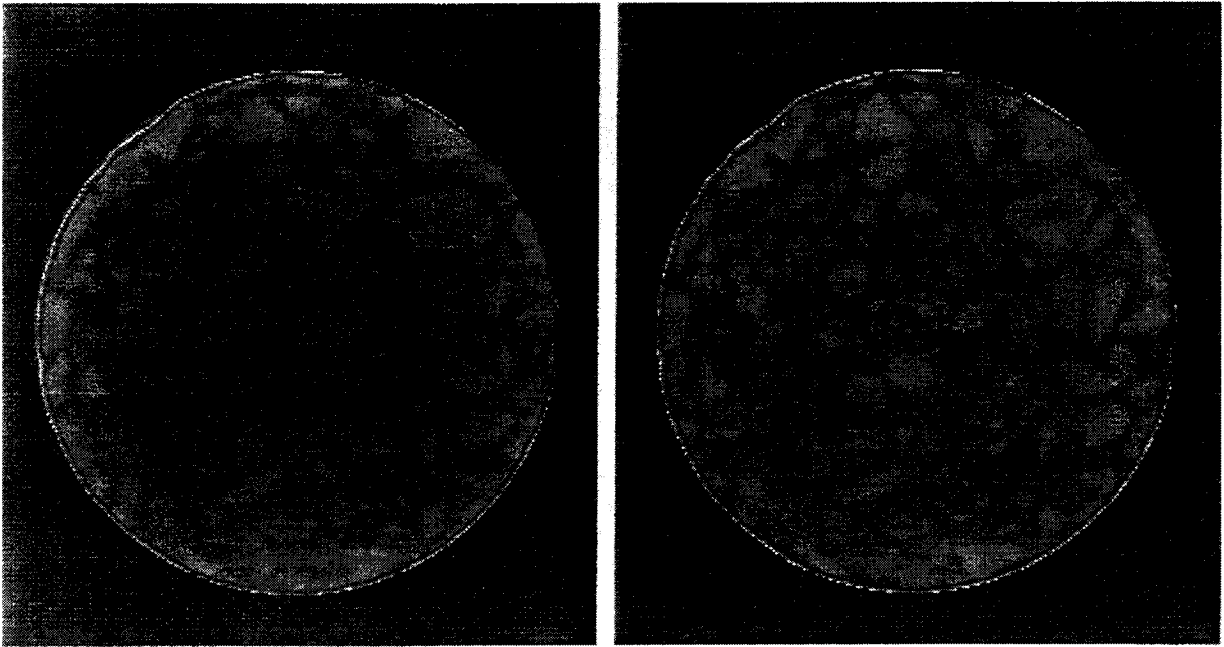


Figure B.5 The image of a mixed fine/coarse aggregate core before and after the beam hardening calibration.

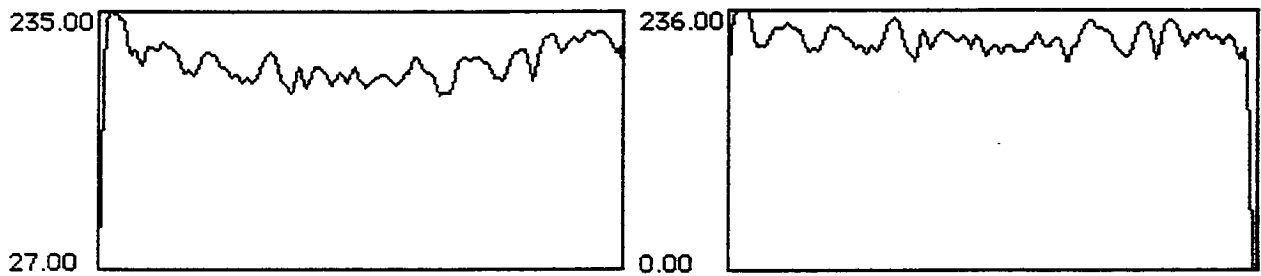


Figure B.6 The variation of the CT number along a diameter of the image in figure B.5 before and after BH calibration. Notice how the calibration produces a more uniform CT variation along the diameter.

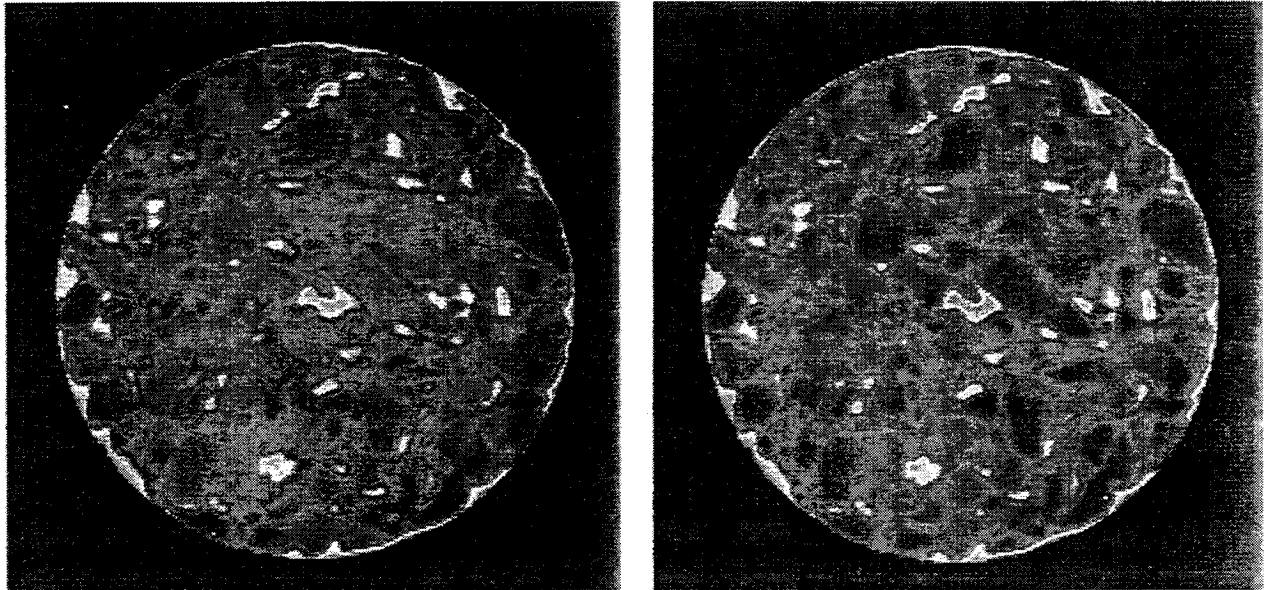


Figure B.7 The image of a coarse core before and after the beam hardening calibration.

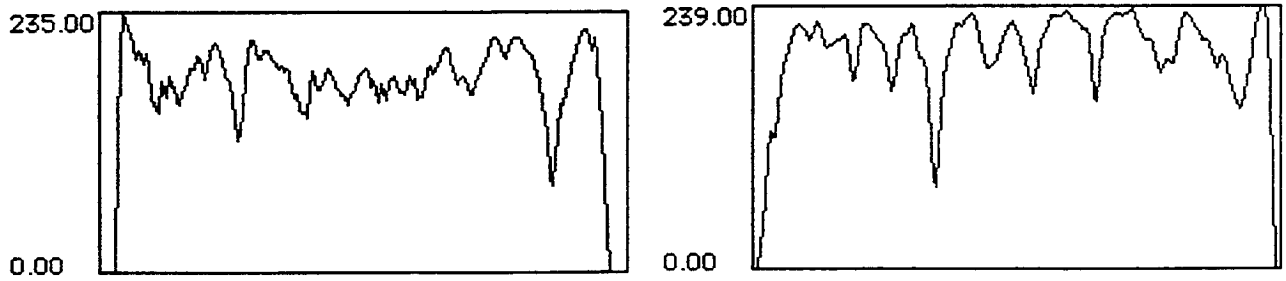


Figure B.8 The variation of the CT number along a diameter of the image in figure B.7 before and after BH calibration.

core under study is approximately uniform; then this procedure works relatively well.

1. **Open** the image which you like to calibrate.
2. **Modify data**.
3. **Measure** in the **custom** menu.
4. Use **BH Calibration**.

Examples of self-calibration are shown in figure B.9; the uncorrected image is the one shown in figure B.5 Figure B.10 shows the corresponding CT number variation curve, but obtained with the RoI procedure described earlier. Again, note that the self-calibration procedure works well for relatively uniform cores.

All these operations and other operations of IPLab could be combined together in a batch file by creating an IPLab script file, as required. (See also the IPLab manual, pages 61–71.)

3.3 Mass fraction analysis

The mass fraction analysis is dependent on the CT values of the various core components. By default, the ASPLab assumes values for AAG-1 asphalt and RG aggregate. It also assumes the corresponding densities and variation of the CT number with the density, as described in section 9. These values can be changed. See section 3.3.2. (Note that it is only possible to perform volume fraction analysis if only the CT numbers are available; if the densities of the components are also available, then it is possible to perform mass fraction analysis.) The following procedure describes how to perform the mass-fraction analysis on a single image.

3.3.1 Procedures for performing mass-fraction analysis on a single image.

1. Perform the beam-hardening correction as discussed in section 3.2 , if you not already done. (Performing this correction multiple times does not affect the image quality.)
- 2 Go to the **custom** menu and choose **classify mixed** or the **classify coarse** item in the **custom** menu. This is only a flag and it does not produce any visible changes.
3. Choose **results** from the **custom** menu. The mass fraction of asphalt in the core is displayed as percentage in the upper right hand corner of the image.

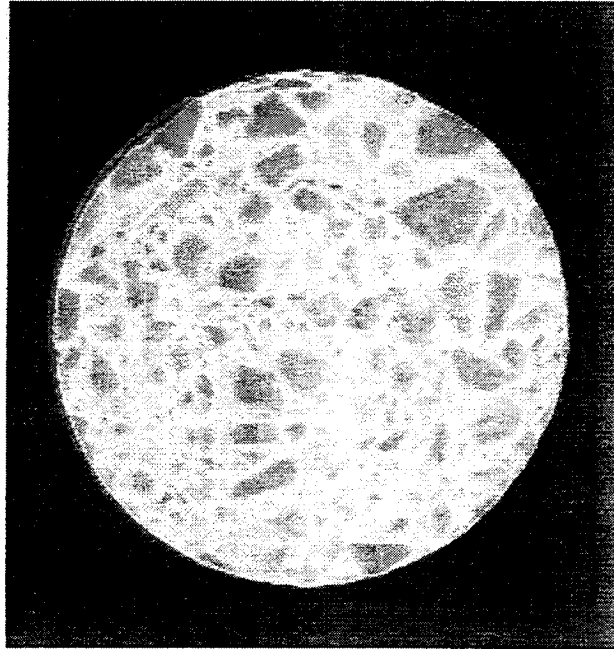


Figure B.9 The image of the mixed coarse/fines aggregate core of figure B.5 after self-calibration .

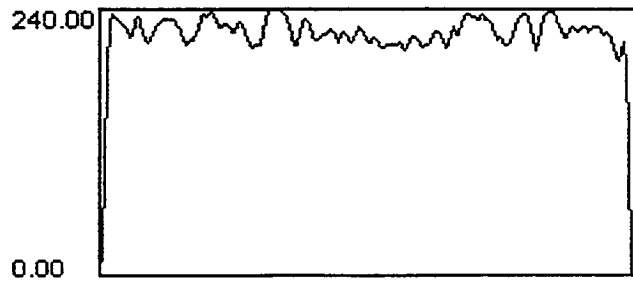


Figure B.10 The variation of the CT number along a diameter of the image in figure B.9 after BH self-calibration.

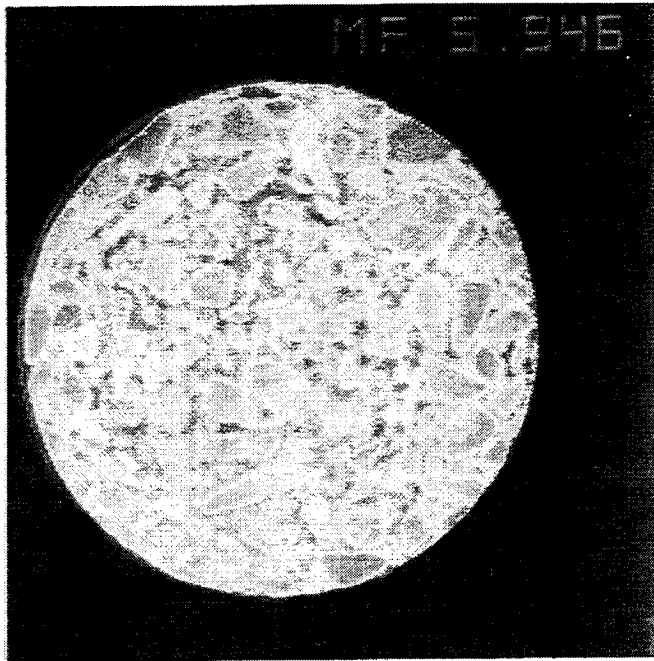


Figure B.11 The image of a mixed coarse/fine aggregate core showing the mass fraction of asphalt.

An example of this operation is shown in figure B.11. The label on the upper right hand corner reads "MF=5.946%"; MF means mass-fraction data.

3.3.2 Procedures for performing mass-fraction analysis on an entire core

To determine the mass fraction for an entire core, all the cross-sectional image-file names should be listed in an IPLab file list; to create this list refer to the IPLab manual page 81 and page 88. Then proceed as follows.

1. Go to **file** menu, **open** and then click on the **script** button.
2. Go to the **scripts Folder** and **open** the **MassClassify.list**.

An example of a script is given in IPLab manual on page 27. Then click on the **run script** button. The script is essentially a batch file which will modify all the data and perform the BH calibration. The mass fraction for the entire core is then displayed on the last image. One important detail is that the calibration image which is used in the beam hardening correction should have the name **fine core**; it should not be included in the IPLab file list, but it should exist in the IPLab image folder. Also, the IPLab script can handle exactly twenty cross-sectional images; if the number of images is different, then the loop number should be changed by opening the IPLab script. The process involves using

file and then **open** to open the **script** and then highlighting the loop command line in the script file, clicking the button **Comment** and changing the value of iterations to any desired value. For more information please refer to page 66 of IPLab.

3.3.3 Setting the asphalt, aggregate and mix CT numbers.

To change the CT values of the different core components, proceed as follows.

1. **Set** the number zero IPLab variable to any non-zero number. This is just a flag to indicate that you don't want to use default values for the CT numbers.
2. **Set** the variable 1 to the CT number of the aggregate.
3. **Set** the variable 2 to the CT number of the asphalt.
4. **Set** the variable 3 to the CT number of air.

Note that if you change the number zero flag, i.e., if you change any of the variables, *you have to change all of them*. Simply ignoring the other variables will not retain the default values but instead ASPlab will assign zero values.

To provide density values for the core-components, proceed as follows.

5. **Set** the number five IPLab variable to any non-zero number. This is again a flag to indicate that you don't want to use default values for the densities.
6. **Set** the variable 6 to the density of the asphalt.
7. **Set** the variable 7 to the density of the aggregate.

Notice that the density values can be in any arbitrary units, provided that they are all in the same units. Also recall that IPLab only accepts integer values as settings for its variables, so multiply decimal values by large integer numbers to assign integer density values.

4. Image enhancements

ASPlab can perform a variety of standard image-enhancement functions. First the beam hardening correction has to be performed. Then the Polygonal Object operator has to be used to prepare the image data.

1. Go to **edit** and then go to **cursor mode** and then to **polygonal object**.†

† This procedure obtains a sample of the data and automatically adjusts internal parameters for optimal results. Usually CT images contain large black background areas, which –if included in the image enhancement calculations– they would produce poor results.

2. Using the mouse draw a closed polygonal boundary within the core image. Then press the **ESC** key to exit. (Refer to the IPLab manual, page 56.)

The switch **ASPCoreView** is a script (a batch operation) which performs most of the common enhancement operations. The script will generate the following five windows.

1. An **enhanced image** window displays the enhanced image by histogram equalization.

2. A **sharpen Image** window which is generated with the "upsharpen" operator.

3. An **edge detection** window which is generated with Robert's operator. (This is the name of a standard image processing algorithm.)

4. An **enhanced edge** window which displays the core image sharpened.

5. A **binary image** window which displays the core-image with only two grey-level intensities allowing identification of the aggregate and of the asphalt. This operation involves assigning threshold values for asphalt and aggregate and then assigning one of two grey-level intensities to each of the two components. It produces images of superior contrast for easier identification.

Examples of these operations are shown in figure B.12 for a fine aggregate core and in figure B.13 for a coarse aggregate core. Figure B.12a shows the original image and the enhanced image. Figure B.12b shows the sharpened image and the edge-Robert image. Figure B.12c shows the sharpened edge image and the binary image. Figure B.13 shows images for a coarse aggregate core in a sequence similar to that in figure B.12.

Additional information is provided in the IPLab manual.

Disclaimer IPLab is a registered trademark of the Signal Analytics Corporation, 374 Maple Avenue East, Suite 200, Vienna, Virginia 22180, telephone number (703) 281-3277. It is protected by the copyright laws of the United States. This software can only be used on one CPU at any given time; unless the proper licences are obtained this software is not for public distribution. USC remains the licensee of Signal Analytics. Anyone wishing to use ASPlab should first contact Signal Analytics to acquire a licence for IPLab and then contact the Department of Civil Engineering at USC (213) 740-0603 for ASPlab.

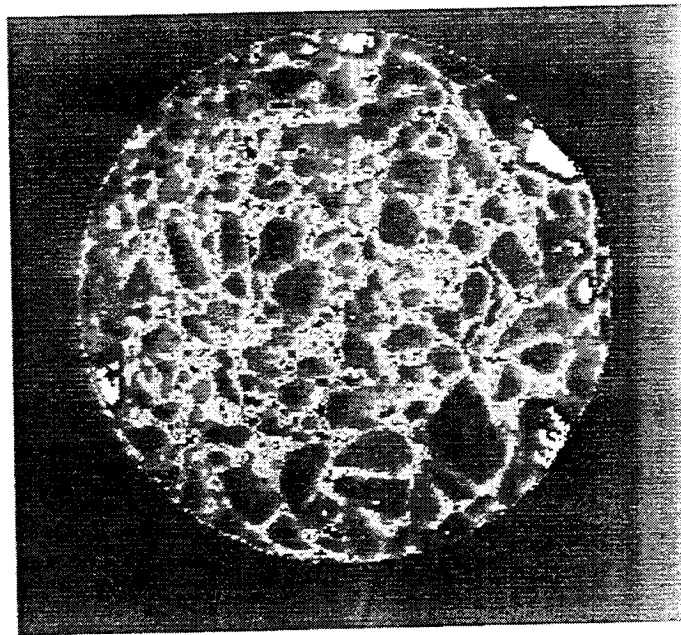
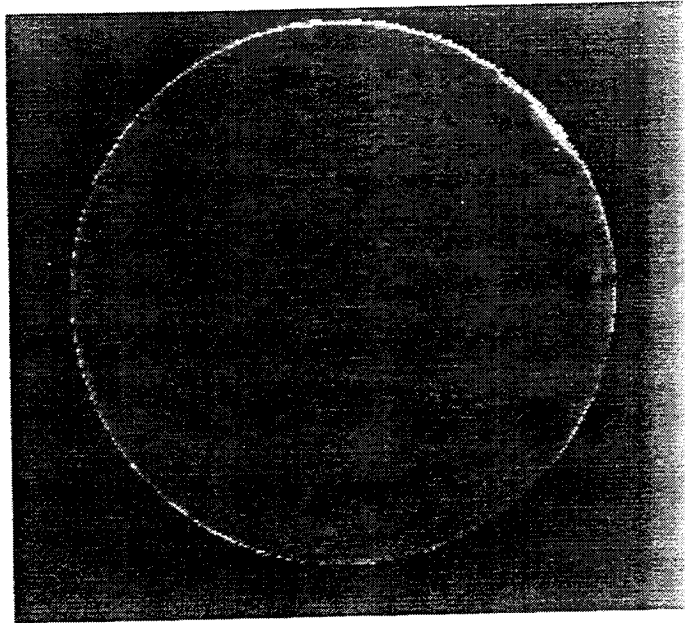


Figure B.12a The image of a mixed core and the enhanced image.

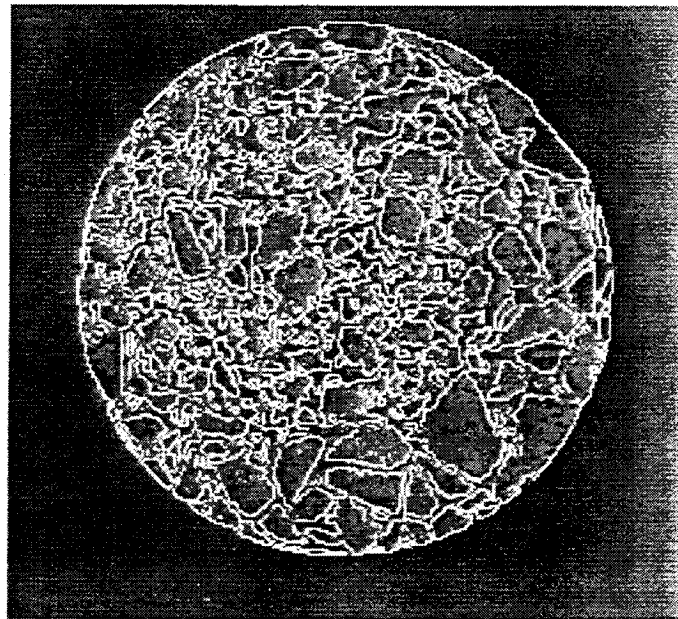
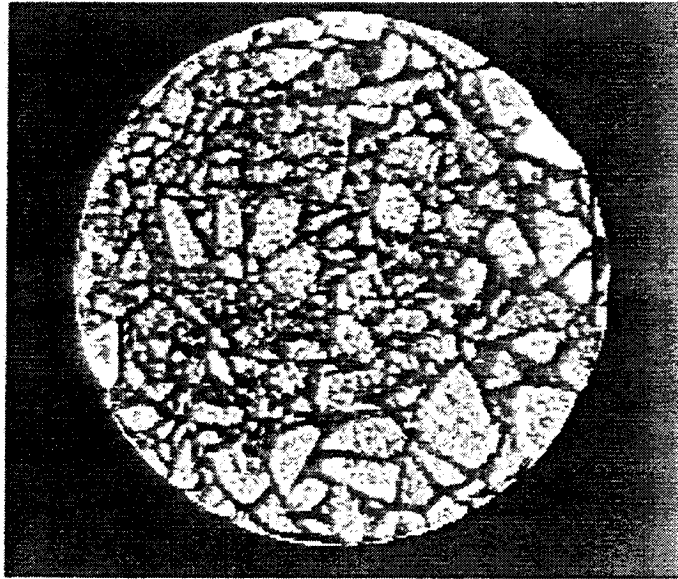


Figure B.12b The sharpened image and the edge-Robert image of the core in figure B.12a.

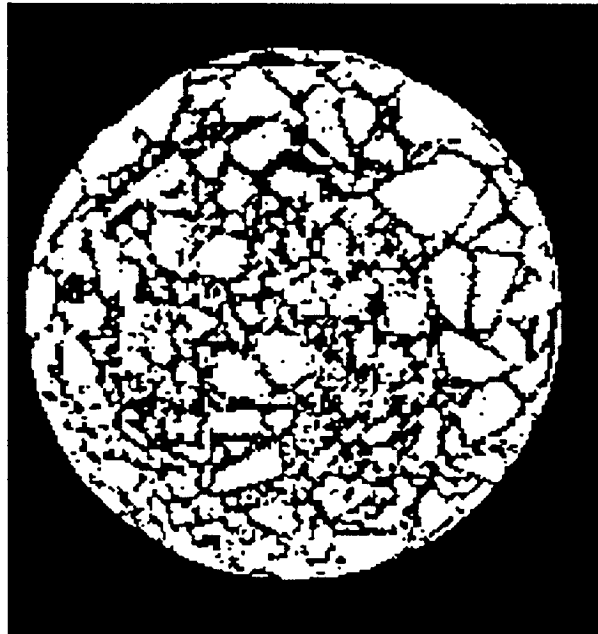
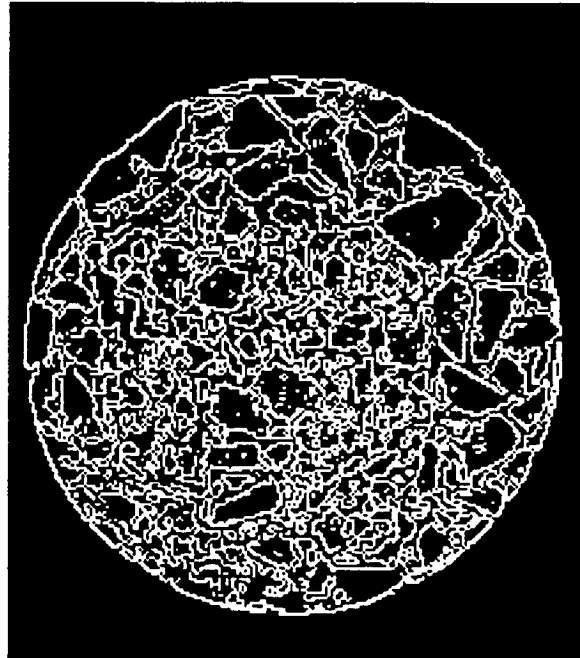


Figure B.12c The sharpened edge image and the binary image of the core in figure B.12a.

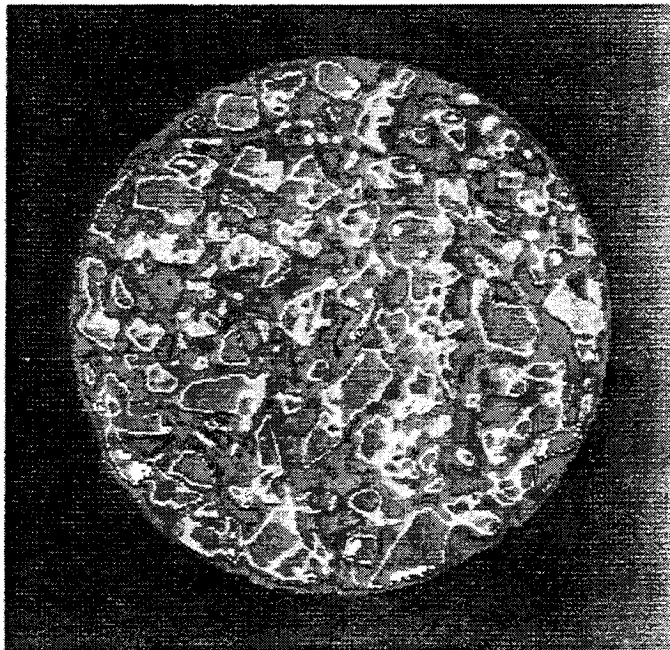
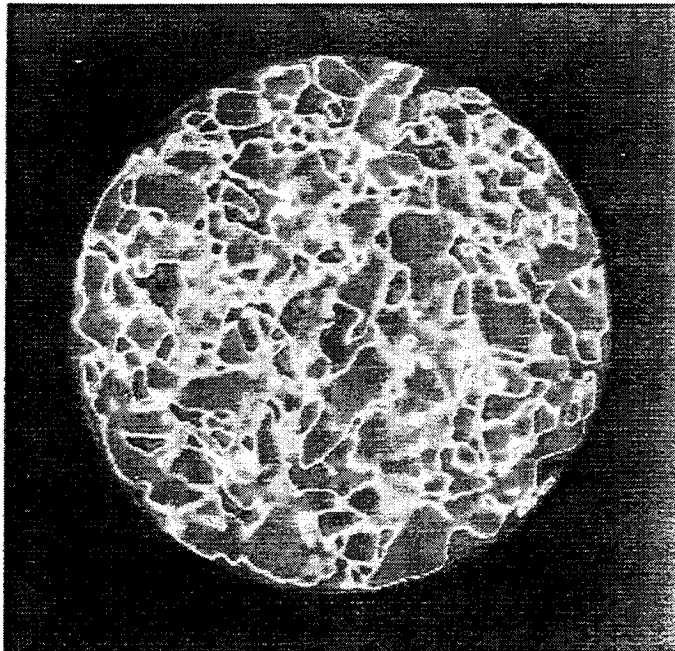


Figure B.13a The image of a coarse core and the enhanced image.

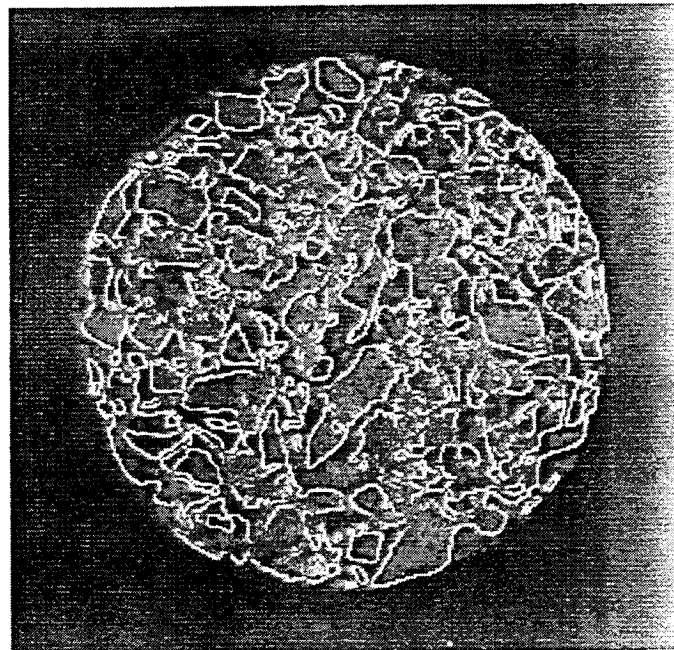
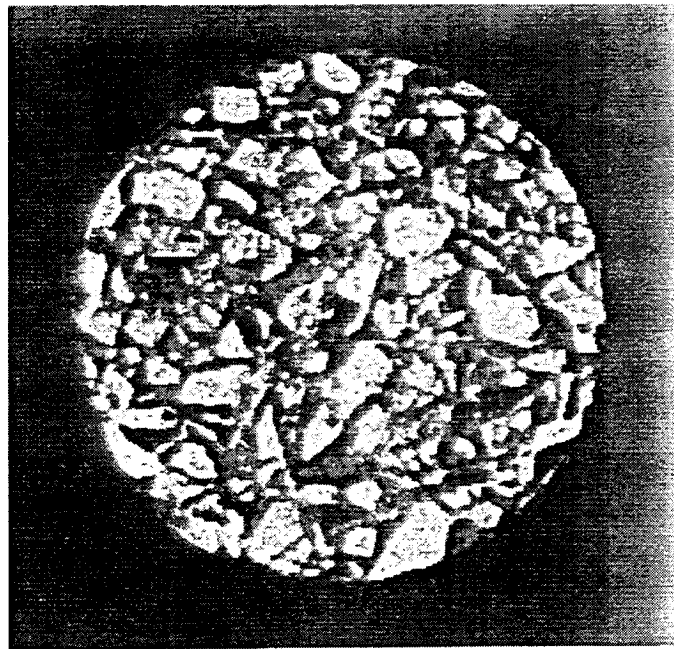


Figure B.13b The sharpened image and the edge-Robert image of the core in figure B.13a.

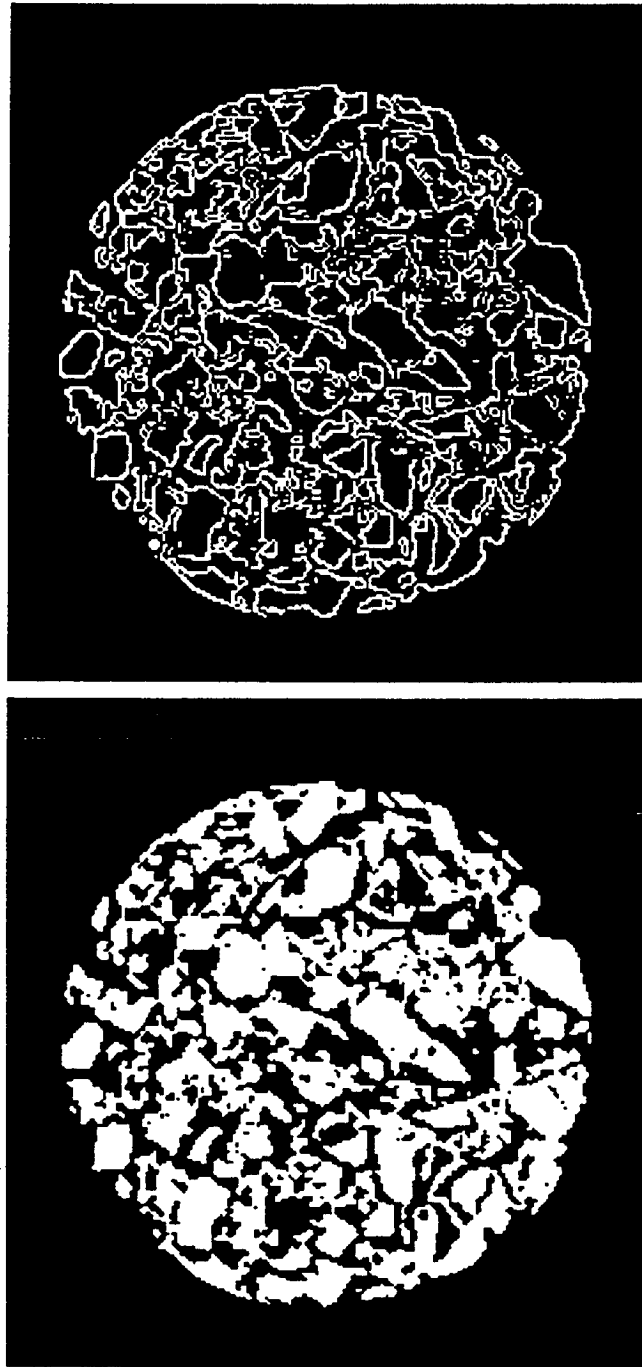


Figure B.13c The sharpened edge image and the binary image of the core in figure B.13a.

Asphalt Advisory Committee

Chairman

Thomas D. Moreland
Moreland Altobelli Associates, Inc.

Vice Chairman

Gale C. Page
Florida Department of Transportation

Members

Peter A. Bellin
*Niedersachsisches Landesamt
für Strassenbau*

Dale Decker
National Asphalt Paving Association

Eric Harm
Illinois Department of Transportation

Charles Hughes
Virginia Highway & Transportation Research Council

Robert G. Jenkins
University of Cincinnati

Anthony J. Kriech
Heritage Group Company

Richard Langlois
Universite Laval

Richard C. Meininger
National Aggregates Association

Nicholas Nahas
EXXON Chemical Co.

Charles F. Potts
APAC, Inc.

Ron Reese
California Department of Transportation

Donald E. Shaw
Georgia-Pacific Corporation

Scott Shuler
The Asphalt Institute

Harold E. Smith
City of Des Moines

Thomas J. Snyder
Marathon Oil Company

Richard H. Sullivan
Minnesota Department of Transportation

Haleem A. Tahir
*American Association of State Highway
and Transportation Officials*

Jack Telford
Oklahoma Department of Transportation

Liaisons

Avery D. Adcock
United States Air Force

Ted Ferragut
Federal Highway Administration

Donald G. Fohs
Federal Highway Administration

Fredrick D. Hejl
Transportation Research Board

Aston McLaughlin
Federal Aviation Administration

Bill Weseman
Federal Highway Administration

Expert Task Group

Ernest Bastian, Jr.
Federal Highway Administration

Wayne Brule
New York State Department of Transportation

David Esch
Alaska Department of Transportation

Joseph L. Goodrich
Chevron Research Company

Woody Halstead
Consultant, Virginia Highway & Transportation Research Council

Gayle King
Bituminous Materials Company

Robert F. LaForce
Colorado Department of Transportation

Mark Plummer
Marathon Oil Company

Ron Reese
California Department of Transportation

Scott Shuler
Colorado Paving Association